Design and Fabrication of Nanotweezers for Nanomanipulation

By

Fardad A. Hashemi

B.S. University of California at Berkeley (1998)
M.S. Massachusetts Institute of Technology (2000)

Submitted to the Department of Mechanical Engineering
in partial fulfillment of the requirements for the degree of

Doctor of Philosophy in Mechanical Engineering

at the

MASSACHUSETTS INSTITUTE OF TECHNOLOGY

MASSACHUSETTS INSTITUTE OF TECHNOLOGY
JUN 16 2005
LIBRARIES

June, 2005

©2005 Massachusetts Institute of Technology. All rights reserved.

Author.....
Department of Mechanical Engineering
18 May, 2005

Certified by .....
Gang Chen
Professor of Mechanical Engineering
Thesis Supervisor

Accepted by .....
Lallit Anand
Professor of Mechanical Engineering
Chairman, Department Committee on Graduate Students

ARCHIVES

ARCHIVES

Design and Fabrication of Nanotweezers for Nanomanipulation

By

Fardad A. Hashemi

Submitted to the Department of Mechanical Engineering on 18 May, 2005
in partial fulfillment of the requirements for the degree of
Doctor of Philosophy in Mechanical Engineering

ABSTRACT

Experimentation and realization of new product concepts at the nanoscale present new challenges. Due to the diffraction limit of visible light it is not possible to see at this scale using optical microscopes. The Scanning Tunneling Microscope (STM) and the Atomic Force Microscope (AFM) are widely used tools for visualization at this scale and serve as the eyes into the nano-world. The ability to probe, manipulate, and construct at this scale is a continuing challenge that needs to be addressed. There are concurrent projects in both industry and academia to construct nanotweezers to serve as the hands and arms for nanomanipulation. Most such devices are not fabricated using completely batch processes and lack the consistency, feature definition, and ease of production required for general use. In this project, we propose a completely batch fabricated nanotweezer designed for compatibility with the AFM. We have developed a completely batch process for making overhanging, electrostatically actuated, compliant mechanism nanotweezers with nanoscale gripper motion resolution. The nanotweezer we tested requires lower actuation voltage and is more compliant than other similar grippers. It also has desired out of plane stiffness and resonance modes for operation with the AFM. We have also developed a batch process to fabricate self-aligned nanoscale tips with nanoscale spacing without the need for nanoscale lithography. The two processes are compatible and can be combined to batch fabricate consistent and practical nanotweezers for large scale use.

Thesis Supervisor: Gang Chen
Title: Professor of Mechanical Engineering

ACKNOWLEDGMENTS

It is now near the end of the last part of my Ph.D. experience and I have a little time to reflect on this experience and the people who helped and taught me.

To my advisor Prof. Gang Chen I am most grateful for his advice and support during this project. His vision started this project and gave me a chance to work on a topic that I truly enjoyed. Through a unique combination of frankness and patience Gang has taught me a lot about his approach to problem solving and life in general. He always has our best interest in mind and I feel privileged to have worked in his group.

I have the deepest respect and admiration for Prof. Scott R. Manalis who agreed to be on my committee and advised me throughout the project. Prof. Manalis's advice has always been dead on. I am privileged to have had the benefit of his experience and all the wrong paths it saved me from.

I decided to pursue the Ph.D. in part due to Prof. Alexander H. Slocum. His enthusiasm for design and engineering is both contagious and addictive. I had to stay to learn more and let my mind stumble into and out of new hidden places yet to be discovered. I was so grateful to have the benefit of his advice and encouragement when he agreed to be on my committee. I am even more grateful for his constructive criticism.

I have been lucky to be in company of such good lab mates. Gang definitely knows how to pick the best of MIT. In particular, I want to thank Chris Dames for our many long hours of discussion. A lot of good ideas came from our discussions, and perhaps even more important, a lot of bad ideas were rightfully discarded as a result. His support has been invaluable.

I wanted to thank the wonderful people at MTL for their insight, patience, and support. I have learned a lot from them. In particular, I want to thank Vicky Diadiuk for her kindness, advice, and understanding; Gwen Donahue for her immense knowledge of microfabrication which she was so willing to share; Kurt Boderick for his enthusiasm and instruction; Eric Lim for helping me better understand and fine tune processes; Paul Tierney for introducing me to the clean room and for his patient explanations; and Dennis Ward for his incredible understanding of the DRIE processes and for making things so much easier to accomplish.

I also wanted to thank Prof. Dennis M. Freeman for letting me use his laboratory equipment and Shih-Chi Chen for teaching me how to use it. I was able to get a much better understanding of my devices from the data I obtained using this equipment.

As all mechanical engineering graduate students, I can not possibly thank Leslie Regan enough for taking care of us. She is our all knowing guardian. She is the first one we turn to when we need help and she always comes through for us.

I am thankful to my friend Kumaran for his relaxed intensity and support during my quals; to my loving friend Merche, her husband, and their adorable daughter for their support and warmth; to Pouyan for our many escapades and conversations; to Reza for staying true to his principles; to Anjelica for her support over our many years of friendship and for calling me to make sure I was working on this thesis. To all of you many many thanks. I am indebted to my good friend Navid Sabbaghi for his wisdom and selflessness. My growth to this stage would not have been possible without his advice and mentoring. I am a better person as a result of our long friendship.

Finally, I would like to express my everlasting gratitude to my parents Fereidoon and Sohi Hashemi and my bother Farshid. They made many sacrifices for my education and well being. They taught me the value of dignity, character, and how to maintain balance in life. I will strive to follow their example as best as I can.

Contents

Chapter 1 Introduction 21

1.1 Background 21

1.2 Prior Work 23

1.3 Motivation 25

1.4 Nanotweezer Requirements 25

1.4.1 Key requirements 26

1.4.2 Target goals 26

1.5 Thesis Overview 27

Chapter 2 Design 29

2.1 Design Architecture 29

2.2 Electrostatic Actuators 33

2.2.1 Theory for electrostatic actuators 33

2.2.2 Parallel plate electrostatic actuators 35

2.2.3 Combdrive electrostatic actuators 37

2.2.4 Comparison of parallel plate and combdrive actuators 39

2.3 Modeling of the Flexure Behavior 42

Chapter 3 Fabrication 66

3.1 Pattern Combination/Multiplication Lithography 66

3.2 DRIE Process 78

3.3 Surface Tension 80

3.4 Solution to Circumvent Wet Release 82

3.5 Struct-v3 Process 83

3.5.1 Bumpers 89

3.6 Outcome of Fabrication 91

Chapter 4 Device Testing 93

4.1 Experimental Setup 93

4.2 Analysis and Explanation of Results 97

Chapter 5 Nanocut Process 104

5.1 Process Flow 104

5.2 Process Results 108

5.3 Combination of Nanocut and Struct-v3 processes 114

5.4 Other Applications of Nanocut 116

Chapter 6 Future Work and Conclusion 119

6.1 Future Work and Considerations 119

6.1.1 Robust design paradigm 119

6.1.2 Sensing tip sample interactions 123

6.2 Lessons Learned 130

6.2.1 Nanoscale tips 130

6.2.2 Process flow development 131

6.2.3 Sub-process debugging 132

6.2.4 Summary of Contributions 135

List of Figures

Figure 2-1. Schematic showing how a SOI wafer is used to fabricate the nanotweezers. Nanotweezers are fabricated in the device layer. Parts of the substrate and oxide layer are removed to create overhanging structures. 30

Figure 2-2. Schematic showing the function of an AFM probe. An optical lever consisting of a laser beam that reflects of the back of the cantilever and into the photodiode detector measures probe deflection. This deflection is indicative of the force interaction between the tip and the sample. 31

Figure 2-3. Schematic showing the in-plane design of the overhanging nanotweezer structure. The two arms on the side each have a flexure mechanism for translation and combdrive for actuation. 32

Figure 2-4. Schematic of a general electrostatic actuator. Force F is the force exerted on the actuator. Coordinate x is the position of the moving electrode relative to the fixed electrode on the right. 33

Figure 2-5. Schematic of a parallel plate electrostatic actuator pulling against a spring of constant k. 36

Figure 2-6. SEM of a combdrive actuator showing the interdigitated teeth 38

Figure 2-7. Schematic of a combdrive electrostatic actuator. Only one comb tooth is shown for simplicity. In practice many comb teeth are used (dimmed lines). x_0 is the amount of interdigitation as fabricated. 38

Figure 2-8. Schematic of a typical hammock flexure. 42

Figure 2-9. Diagram indicating annotation for each beam comprising the nanotweezers arm flexure mechanism. Color coordination of the annotation indicates a symmetric set: blue for set A, red for set B, and green for set C.....43

Figure 2-10. Diagram highlighting the smaller junctions that connect beam set A with B.....45

Figure 2-11. Schematic showing positive force and moment notation for an elemental beam section.....46

Figure 2-12. Diagram highlighting the half hammock beam set C. This part of the flexure mechanism forms a hammock type flexure and can be analyzed independent of the other beams. 47

Figure 2-13. Force and moment diagram for beam set C. Insert on the top left corner indicates the section of the flexure mechanism that is depicted in the diagram. This section is the larger junction that connects beam set B with C. The x coordinate system originates from the larger junction. The positive direction for deflections of the beam is horizontal and to the left...48

Figure 2-14. Force and moment diagram for beam set A. Insert on the top left corner indicates the section of the flexure mechanism that is depicted in the diagram. This is the anchor section of flexure mechanism that connects beam set A to the substrate. The x coordinate system originates from the anchor points. The positive direction for deflections of the beam is horizontal and to the left. 51

Figure 2-15. Force and moment diagram for junction of beam 1 and 2. This is one of the smaller junctions that connects beam set A with B. This junction is

the one on the left indicated in Figure 2-10. The x coordinates point in opposite directions. The positive direction for deflections of the beam is horizontal and to the left. 52

Figure 2-16. Force and moment diagram for the junction of beam 4 and 5. This is one of the smaller junctions that connects beam set A with B. This junction is the one on the right indicated in Figure 2-10. The x coordinates point in opposite directions. The positive direction for deflections of the beam is horizontal and to the left. 53

Figure 2-17. Force and moment diagram for the larger junction connecting beam set B with C. Insert on the top left corner indicates the section of the flexure mechanism that is depicted in the diagram. The loading from beam set C on the junction is represented as force moment pair. The positive direction for deflections of the beam is horizontal and to the left. 55

Figure 2-18. Schematic of kinematic constraints for the beam set junctions. Using the axially rigid beam assumption, any rotation of the larger junction (of length y_L) must be completely accommodated for by consequent rotations of the small junctions (of length y_o)....57

Figure 2-19. FEA model of the left nanotweezer arm subjected to an out of plane force at the tip. The model shows exaggerated deflection. This is a 1000x model where the color bar shows displacement in units of mm corresponding to units of μm in real life. A model force of 0.15 N is applied corresponding to real life force of 1.5×10^{-7}N....62

Figure 2-20. FEA diagram showing the 6th resonance mode of vibration of the nanotweezer arm. Deformation has been exaggerated for visualization. 64

Figure 2-21. FEA diagram showing the 7th resonance mode of vibration of the nanotweezer arm. Deformation has been exaggerated for visualization. 64

Figure 3-1. Diagram showing the effect of shuttering and offset with a stepper lithography tool on the wafer pattern. The top two diagrams show the area of the reticle that is shuttered down. The lower left diagram shows the resulting exposed pattern on the wafer. The lower right diagram shows the same pattern offset to the center of the die. Offset is achieved by moving the wafer underneath the reticle.....68

Figure 3-2. Diagram showing the shuttering of two regions of the reticle to be combined for exposure on the wafer. The two patterns, which are disjoint on the reticle, will be offset during exposure to form a connected pattern on the wafer space.....69

Figure 3-3. Diagram showing pattern combination of two disk patterns, a) shows the commonly expected resulting pattern that is incorrect, b) shows the actual pattern resulting from the combination of the two disks, c) shows what patterns need to be combined to from the desired pattern of a).....70

Figure 3-4. Diagram showing how the pattern in the converging zone of the contact pads (shown in black cross-hatch) combines with the nanotweezer pattern (shown in red cross-hatch).....72

Figure 3-5. Diagram showing potential pattern errors that can be caused by misalignments and ways to avoid them. a) shows the spikes caused by

horizontal misalignment, b) shows how to avoid the spikes by use of a bridge segment, c) shows effect of horizontal misalignment on the bridge segment, and d) shows effect of vertical misalignment on the bridge segment. 73

Figure 3-6. Diagram showing how encompassing bridge segments can be used to avoid narrowing of bridge segments due to misalignment of the patterns. ..74

Figure 3-7. Diagram demonstrating the use of tangential circular bridge segments to prevent sharp concave and convex corners caused by misalignment of the patterns, a) perfectly aligned, b) horizontally misaligned, c) vertically misaligned 76

Figure 3-8. Diagram showing the use tangential encompassing circular bridge segments. This combined approach both preserves minimum bridge width and avoids sharp concave and convex corners despite misalignment of the patterns 77

Figure 3-9. SEM photos showing the result of pattern combination/multiplication lithography in practice, a) shows how the pattern from the large contact pads seamlessly converges down to the contact lines leading to the nanotweezer, b) is a magnified view of the intersection region showing a small step caused by the misalignment of the two patterns circled in red. ...78

Figure 3-10. SEM photo of structure formed by the FARDAD DRIE process showing the smooth side walls created by the process 79

Figure 3-11. Close-up SEM photo of structures showing effect of surface tension on the structures. The slender beams have permanently adhered to each other and the device is destroyed. 81

Figure 3-12. 2-D Diagram of the entire process flow. The left column (steps 1-4) shows the patterning and bracing of the device layer. The middle column (steps 5-8) shows the mounting of the SOI water and subsequent BOX layer removal and die separation. The right column (step 9) is the final ashing step. 83

Figure 3-13. Process flow diagram for nanotweezers structures at the completion of step 2 (post DRIE). Insert on the right shows a perspective view of a representative 3 × 3 die section of the wafer. 84

Figure 3-14. Process flow diagram for nanotweezers structures at the completion of step 4 (post PR brace). Insert on the right shows a perspective view of a representative 3 × 3 die section of the wafer. 85

Figure 3-15. Process flow diagram showing the device wafer mounted to a mount wafer a). The mount wafer has special pillars and channels surface micromachined into its interface surface with the device wafer. The locations of these pillars and channels relative to the device wafers are shown in a see through diagram b). 86

Figure 3-16. Process flow diagram for nanotweezers structures after step 8 (post backside die release). Insert on the right shows a perspective view of a representative 3 × 3 die section of the wafer. 88

Figure 3-17. Process flow diagram for nanotweezers structures at the completion of step 9 (post dry dismount). Insert on the right shows a perspective view of a representative 3 × 3 die section of the wafer. At this point the individual dies are no longer stuck to the mount wafer and can be extracted for use. 89

Figure 3-18. Optical microscope photo of the wafer after the back side DRIE etch (step 7). The photo shows the nanotweezer section and the contact lines that are converging in. Bumper structure that surround the nanotweezer are surface micromachined in the device layer to prevent cracks from propagating through the device. 90

Figure 3-19. SEM photos of the nanotweezers structures after extraction from the process. Insert on top corner of the picture on the right shows a magnified view of the tips region. 91

Figure 3-20. Close-up top view SEM photo of the nanotweezer flexure mechanism showing beam anchor points. 92

Figure 4-1. Photograph of experimental setup 94

Figure 4-2. SEM photo of the nanotweezers in the closed position 96

Figure 4-3. Close-up SEM photo of the nanotweezers' tips in the open and closed positions 96

Figure 4-4. Graph showing measured vs. calculated actuation data 97

Figure 4-5. Amplitude plot for in-plane frequency response of the nanotweezers 98

Figure 4-6. Phase plot for in-plane frequency response of the nanotweezers 98

Figure 4-7. Diagram showing the effect of the footing from the DRIE etch on the beam cross-section 99

Figure 4-8. SEM photo showing the effect of the footing from the DRIE etch on the structure. The effect is visible underneath the structure where the BOX layer was, prior to removal. 100

Figure 4-9. Graph showing measured vs. calculated actuation data. The new calculated data accounts for structural deviations caused by footing by incorporation of an effective beam thickness and combdrive gap. In this case, effective parameters were optimized to match deflection data. 101

Figure 4-10. Graph showing measured vs. calculated actuation data. The new calculated data accounts for structural deviations caused by footing by incorporation of an effective beam thickness and combdrive gap. In this case, effective parameters were optimized to match in-plane frequency response 102

Figure 5-1. Process flow diagram for the Nanocut process 105

Figure 5-2. SEM photos of features created using the Nanocut process. On the left is a view of a pyramidal wall created by a nitride line mask. On the right is a cross-section view of a similar pyramidal wall 107

Figure 5-3. Close-up cross-section SEM photos of a pyramidal wall created using the Nanocut process 108

Figure 5-4. SEM photo of experimental results for the Nanocut process 108

Figure 5-5. Graph of oxidation thickness vs. time for the thermal oxidation process 109

Figure 5-6. Graph of results for the Nanocut process 113

Figure 5-7. Schematic of the combined Nanocut and Struct-v3 processes.....115

Figure 5-8. SEM photos of thin walls micromachined into Si using the Nanocut process.....117

Figure 5-9. SEM photos showing the application of the Nanocut process to rings fabricated for Metamaterials applications.....118

Figure 5-10. SEM photos showing an array of apertures created using the Nanocut process.....118

Figure 6-1. Diagram showing the attachment of an external flexure based grating to the existing nanotweezer arm. The grating flexure would be designed to be much more compliant than the arm flexure. 127

Figure 6-2. Plots showing normalized intensity of reflection of a grating as a functional of angle a), with increased number of grating lines b), with increased spacing between the grating lines c). 128

Figure 6-3. Plots showing normalized intensity of reflection of a flexure arm grating as a functional of angle. Blue plot corresponds to the relaxed state. Red plot corresponds to the fully extended state.....129

List of Tables

Table 1-1. Summary of design requirements 28

Table 2-1. Table showing characteristics of the combdrive actuator. A range of 2 μm is required of each arm to close the 4 μm gap of the nanotweezers. 61

Table 2-2. Table showing various displacement results and subsequent spring constants derived from FEA model. All spring constants are measured at the tip. 63

Table 3-1. Table of parameters for "FARDAD" DRIE etch recipe. 80

Table 5-1. Table of starting oxide thickness for each wafer 110

Table 5-2. Table of oxide thickness for each wafer post nitride etch 110

Table 5-3. Table of oxide thickness for each wafer post DRIE etch 111

Table 6-1. Table of poly-Si RIE etch modifications 134

Chapter 1 Introduction

1.1 Background

The benefits of higher density, smaller electronic devices, lower power consumption, and the ability to engineer new materials have fueled technological advances for working at continuously smaller length scales. The progress from microscale to nanoscale, however, transitions below the wavelength of visible light and presents its unique challenges. Due to the diffraction limit of visible light it is not possible to see at this scale using optical microscopy. A new set of tools are needed for imaging and manipulation at this scale.

To address this, in 1981 IBM researchers, Bining and Rohrer, developed the scanning tunneling microscope (STM). In similar manner to a stylus profiler[1], the STM scans a sample using tunneling current between an ultra sharp tip and the sample to generate three dimensional surface topography.[2] The STM provides resolution down to individual atoms but can only image conducting samples. To address this limitation, in 1986 Binning, Quate, and Geber invented the atomic force microscope (AFM). This microscope scans similar to the STM but uses force interactions of the sharp tip, instead of tunneling current, to generate topography.[3] The AFM measures deflections of a very flexible cantilever supporting the tip as an indication of the tip-sample force interaction. The original setup of the AFM used a STM probe to measure deflections of the AFM via tunneling current between the two. Today most commonly, a laser beam reflected off of

the cantilever to a photodiode is used as an optical lever system to measure deflections of the cantilever. Other methods have been developed since to improve AFM performance. Two such examples include measuring diffracted mode intensity off of a grating created by interdigitated fingers attached to the cantilevers[4] and the use of cantilevers with integrated piezoresistive sensors and piezoelectric actuators.[5] New methods to enhance and build upon the capabilities of AFM are still being developed. The AFM is one of the most commonly used tools for visualization at nanoscale and serves as the primary eyes into the nano-world.

The ability to probe, manipulate, and construct at this scale has been even more challenging. There has been some success at nanomanipulation using the AFM probe as means to push and pull objects around on the sample.[6] A novel example of this is by Superfine and his group who connected a haptic interface to the AFM[7] to assist in nanomanipulation. Their setup allowed the user to feel the force for the tip on the sample in real time. The haptic interface allowed for more precise manipulation of the sample. Using Superfine's nanoManipulator scientists were able to manipulate and extract mechanical properties for viruses[8], DNA[9], and carbon nanotubes[10] and investigate friction at the molecular level.[11] Despite this and other advances, as of yet, there are no practical tools that can be used to grip, pick, and place objects for general experimental setup and realization of new product concepts. The arms and hands to grip and pick up objects at the nanoscale are a much needed goal still under development. This thesis is an attempt to add gripping manipulation functions to the AFM, through the development of batch fabricated nanotweezers.

1.2 Prior Work

Perhaps the earliest microfabricated gripper was made at UC Berkeley[12] in 1992. These were overhanging devices able to access and pick up micro-size objects. They did not have nanoscale tips and were not intended to pick up smaller objects. However, the microgrippers were well suited for general use and quantity production because they were completely batch fabricated.

In 1999, Lieber's group of Harvard university demonstrated one of the first proofs of concept of a nanotweezer made out of carbon nanotubes.[13] Their nanotweezers were constructed by depositing two electrically independent gold electrodes onto a micropipette and then attaching a carbon nanotube to each electrode. When the two carbon nano-tubes were biased electrically with respect to each other, they attracted each other and would close similar to tweezers. Although the two arms were separated by 2μm, each one was only 50nm in diameter making it more suitable for interacting with nanoscale objects than the microgrippers. In addition, Lieber's nanotweezers required only 8.3V to fully close compared to 45V for the microgrippers. However, Lieber's devices were individually fabricated and not suitable for large scale use. Lieber and his group were able to pick up 500-nm polystyrene clusters using a light microscope for visualization. They also successfully used to pick up and electrically probe GaAs nanowires. The results were consistent with theoretical predictions.

An improved version Lieber's nanotube-based nanotweezers was made by Seiji Akita and Yoshikazu Nakayama of Osaka Prefecture University who fabricated nanotweezers by attaching carbon nanotubes to an AFM tip.[14] The AFM tip was first coated with a conducting Ti/Pt film that contacted larger Al contact lines. This film was

then cut into two electrically independent sections using a Gaion beam. They used a specially designed SEM with three movable stages to position the nanotubes on each of the two coated regions of the tip. Finally e-beam contamination deposition was used to deposit an amorphous carbon film on the contact region of the tubes with the tip to secure them. While similar in function to Lieber's nanotweezers, these were created with use with an AFM in mind.

In addition, Bøggild and his group from the Technical University of Denmark constructed a different type of nanotweezers by first batch microfabricating metal coated silicon oxide arms, and then individually growing tips at the end of the arms using focus electron beam contamination growth.[15] Bøggild's nanotweezers provided three major improvements. First, his nanotweezers were at least partially batch fabricated making them easier to produce for large scale use. Second, these nanotweezers' arms could be closed without having to bias the tips with respect to each other. Finally, unlike the micro spaced nanotube nanotweezers, his deposited tips could be made with a gap of only 25nm.

1.3 Motivation

The previously mentioned nanotweezer projects prove the vision and concept but can be improved upon in their fabrication and design. The nanotweezers mentioned are not suitable for general large scale use since they are not readily producible using a batch process. In addition, due to limitations in their construction it is not possible to define a guided direction of motion and constrain compliance along specific directions. As with macroscale applications, it will be difficult to specifically select a single object within tight confines and pick it up with tweezers with that are equally compliant in many directions. In contrast to the nanotweezers, Kim's microgripper is an example of design intent resulting in a mass producible device with well defined features and performance optimized for tweezing applications. Similarly, for the full promise of nanotweezers to be exploited a practical way to manufacture them with guided motion and constrained compliance, and the ability to have better control of feature definition are necessary. Given the limitations of nanoscale patterning and fabrication, it is difficult to match Kim's level of feature definition with nanoscale fabrication. However, through careful re-consideration of required characteristics, alternate, more practical, and more controllable methods of achieving them is possible.

1.4 Nanotweezer Requirements

The objective of this project is to create a nanotweezer that combines the best advantages of the prior art nanotweezers into one that can be readily fabricated and optimized for tweezing. There are some key requirements that are critical to achieve this

objective and to the function of the devices for nanomanipulation. There are also non-critical target goals, which if possible, will greatly enhance the utility and versatility of a nanotweezer.

1.4.1 Key requirements

The first key requirement, which is also the motivation behind this project, is to be able to make functional nanotweezers using a completely batch process. Batch fabrication provides for both consistency and ease of production, both of which are necessary for large scale use and research utility. Second, for further increased research utility, the nanotweezers have to be compatible for use with AFM, as it is the primary visualization tool at this scale. The ultimate vision is to use the same device to both image and manipulate in an AFM. Nanoscale tips are also required both to function as an AFM tip and to be able to interact and access nanoscale objects with nanoscale spacing. Finally, nanoscale motion of the arms with constrained directions of compliance is required to be able to select and accurately grip the desired object based on the image provided by the AFM.

1.4.2 Target goals

In order to successfully pick up small aspect ratio nanoscale objects, such as spheres, it is necessary for the nanotweezers tips to meet at a point when they close. This can be achieved if either the tips maintain alignment as they close or if they can be fabricated in the closed state with a nanoscale gap that is then actuated open. In order to increase the chance of success, both nanoscale alignment of the tips as they close, and the

ability to fabricate tips with a nanoscale gap are target goals. In practice, however, either of the latter may be sufficient.

Another target goal is to create nanotweezers arms that are as compliant as possible in their intended axes of motion. Ideally, they can be fabricated with a spring constant within the range of contact mode AFM cantilevers, which is 0.05-1N/m. Although this is not a strict requirement, it will allow more compliant objects to be picked up without risk of damage and or the need to sense tip position. For a detailed analysis please see section 6.1.2.

Finally, it is desirable for the nanotweezers to require very low drive voltage to fully close. This would reduce the risk of electrical damage to the sample and is a feature that other projects like that of Lieber have emphasized with regard to their device. Table 1-1 summarizes these requirements and goals.

1.5 Thesis Overview

In this project, it is shown that overhanging structures with well defined guided nanoscale motion, desired in-plane compliance, low actuation voltage, and single pitch nanoscale features are possible using a completely batch process. The following sections will layout the design architecture, and subsequent detailed design and analysis of a proposed nanotweezer. Next, a process for fabricating this structure is detailed including the outcome of the fabrication. Actuation and frequency response results for the nanotweezer structure are presented along with justification for deviations from predicted results. Finally, a novel process for batch fabricating nanoscale, nanospaced tips using microscale lithography is illustrated and characterized. The proposed combination of the

two compatible processes can yield the desired final form of the nanotweezers. For the sake of presentation this thesis is centered on one specific nanotweezer design. However, the scope of project goes beyond this case example. The focus of this project is not to make one specific nanotweezer work but rather use a few specific designs as case studies to develop a general framework for the design and fabrication of nanotweezers of certain useful type. For other designs have been fabricated and tested using this general framework e-mail fardad@alum.mit.edu. The contributions of this work are its various innovations in design and fabrication approach that bring rigorous control of feature definition and ease of production into the execution of a useful type nanotweezers for nanomanipulation.

Key Requirements	**Justification**
Complete Batch Fabrication	-Device consistency -Ease of production
Compatibility with AFM	-Ability to image and manipulate using the same tool -No need for calibration to another probe tip
Nanoscale sharp tips	-Ability to scan as an AFM probe -Ability to access within nanoscale Confines
Nanoscale motion control of the tips	-Ability to accurately select and grip an object from within tight confines
Constrained compliance	-Ability to accurately select and grip an object from within tight confines
Target Goals	**Justification**
Nanoscale alignment of the tips as they close	-Ability to pick small aspect ratio Objects
Nanoscale tip separation (gap)	-Ability to pick small aspect ratio Objects
Highly compliant structures	-Ability to grip compliant objects without closed loop control of the tips position
Low actuation voltage	-Reduce risk of electrical damage to sample -Reduce the need to place a matching bias voltage on the sample

Table 1-1. *Summary of design requirements*

Chapter 2 Design

The proposed nanotweezer for this project consists of two arms that can move and close at the tip region to grip objects. This is assumed to be the basic definition of a tweezer. In this regard, the proposed nanotweezer is no different than that of Lieber, Bøggild, or macroscale tweezers. However, its design architecture has been defined to satisfy a different set of requirements as detailed in sections 1.4 and 1.5.

2.1 Design Architecture

The design architecture dictates both the general physical layout of the device and also the fabrication approach. The two are interconnected due to constraints in microfabrication and microassmbly. The architecture determines what technical challenges need to be solved in order to meet the requirements and goals.

To meet the requirement for complete batch production, the entire fabrication, including that of the nanoscale sharp tips, is designed using standard microfabrication processes and microscale lithography. Although nanoscale lithography is available in some industrial clean rooms, it is not available at MIT's Microsystems Technology Laboratory or other similar educational facilities and is not used for this reason. Since gripping or tweezing action involves in plane motions, the SOI wafer is adopted as the fabrication medium. This medium is widely used in MEMS applications. As a result, there is a large number of mature microfabrication processes already developed for its use. As shown in Figure 2-1, SOI wafers consist of a device layer used for the

nanotweezer structure and tips, a sacrificial oxide layer that is removed to release and mobilize the structures, and a large substrate layer that serves as a handle.

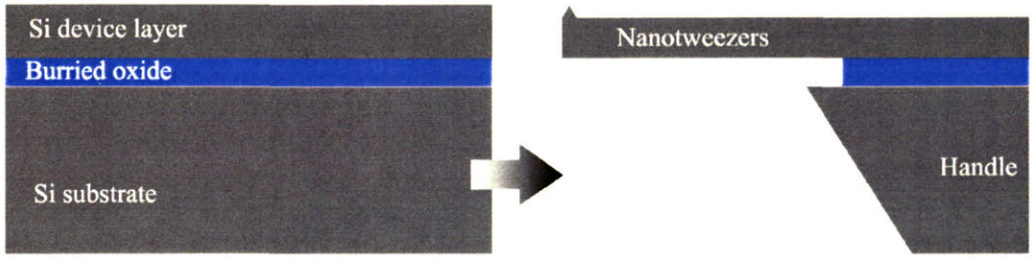

Figure 2-1. *Schematic showing how a SOI wafer is used to fabricate the nanotweezers. Nanotweezers are fabricated in the device layer. Parts of the substrate and oxide layer are removed to create overhanging structures.*

As shown in Figure 2-2, an AFM probe is an overhanging structure that accesses the sample from the one side while the AFM laser accesses it from the other to measure its deflection. To be used as an AFM probe, the nanotweezers must also be overhanging protruding structures with sharp tips that can be accessed from both the top and bottom. The handle section of the SOI is removed as shown in Figure 2-1 to give access from the bottom. In addition, just like AFM probes the nanotweezers are designed to have adequate out of plane compliance to be able to scan over samples without damaging them. The goal is to have an out of plane spring constant within the range of 0.3-1N/m, for contact mode probes. Out of plane compliance and resonance modes of the nanotweezers, which are necessary for measuring tip sample force interactions, are achieved by adjusting the device layer thickness and the design of the in-plane structure. A batch process is developed to achieve sharp tips with nanoscale spacing at the head of the tweezer arms.

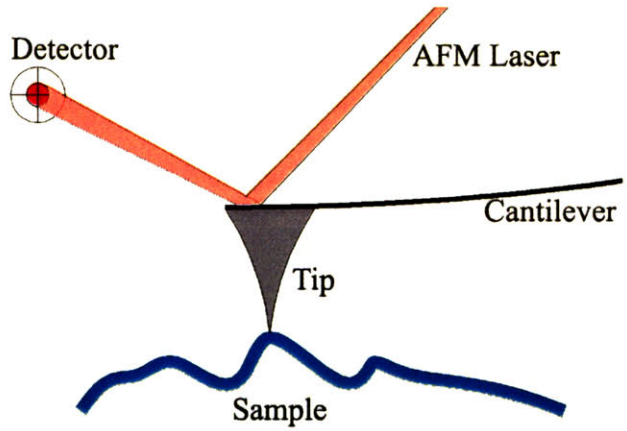

Figure 2-2. *Schematic showing the function of an AFM probe. An optical lever consisting of a laser beam that reflects of the back of the cantilever and into the photodiode detector measures probe deflection. This deflection is indicative of the force interaction between the tip and the sample.*

For the in-plane motion of the nanotweezer arms a flexure mechanism is used. A flexure mechanism allows for guided motion between two objects via elastic deformation of it structure. Flexure mechanisms are often used in place of sliding guides, rails, and bearings in applications that require high precision and small range of motion. Since they do not have sliding components they do not suffer from sticktion or backlash and provide good repeatability within their elastic region of operation. If designed properly, flexure mechanism can selectively constrain compliance in specified directions. In general they are easier to produce than rails and bearings. The latter is particularly true in MEMS applications due to limitations of microfabrication and assembly of microscale objects. Figure 2-3 shows the in-plane layout of the nanotweezers design. The arms, located on the right and left, each have a dedicated flexure mechanism. The mechanism serves two purposes: to allow for guided motion; and act as a linear spring to resist the force of the actuator. Each arm also has an electrostatic actuator that pulls it towards the center electrode. Force from the actuator pulling against the linear flexure spring allows for the

predictable motion. The force of the actuator is matched to the stiffness of the flexure mechanism to allow nanoscale resolution in motion.

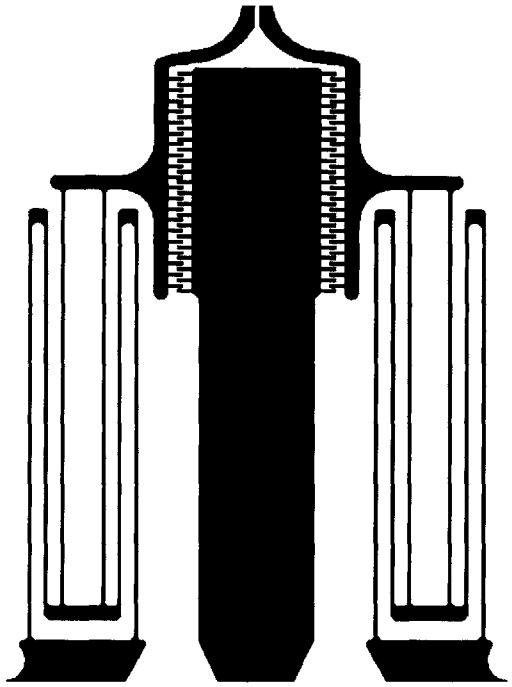

Figure 2-3. *Schematic showing the in-plane design of the overhanging nanotweezer structure. The two arms on the side each have a flexure mechanism for translation and combdrive for actuation.*

Electrostatic actuators are used to provide a well controlled force to pull the arms inward. They were chosen mainly for their simplicity. Unlike piezo and magnetic actuators, electrostatic actuators are generally monolithic planar devices that can be fabricated out of the same conducting Si as the rest of the nanotweezers. They provide force as a repeatable function of voltage. The characteristic of this function and the sensitivity of output force to the input voltage can be customized via modifications of the actuator geometry. Through proper design and matching of the actuator and the flexure mechanism pair, highly compliant arms with nanoscale resolution in motion can be achieved.

2.2 Electrostatic Actuators

Electrostatic actuators convert electrical energy to mechanical work. They are often used in MEMS applications for their convenience. In most application, electrostatic actuators are used to generate planar motion.

2.2.1 Theory for electrostatic actuators

Figure 2-4 shows a simplified generic electrostatic actuator. In this notation the force F exerted on the actuator and x are in the direction that pulls the two electrodes apart.

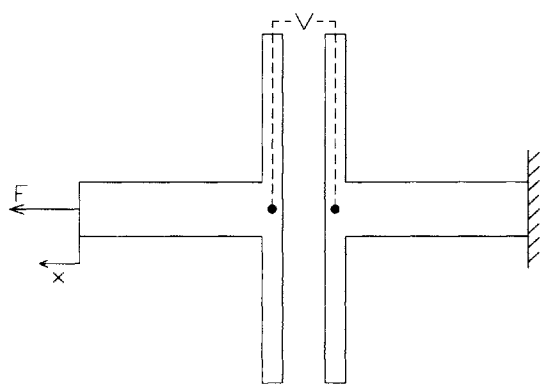

Figure 2-4. *Schematic of a general electrostatic actuator. Force F is the force exerted on the actuator. Coordinate x is the position of the moving electrode relative to the fixed electrode on the right.*

Electrostatic actuators are two port systems with two degrees of freedom and require two of the variables F, x, V, or q (the charge on stored on the plates) to describe their state. Both mechanical and electrical work can be done on these systems to increase their energy.

$$Fdx + Vdq = dE \qquad \textit{(energy balance)} \qquad (2\text{-}1)$$

Using the following constitutive relation,

$$V = \frac{q}{C(x)} \qquad \textit{(constitutive relation)} \qquad (2\text{-}2)$$

the energy of the system can be evaluated and expressed as,

$$E = \frac{C(x)V^2}{2} \qquad (2\text{-}3)$$

Using the latter expressions, the force of the actuator, per the notation in Figure 2-4, can be expressed as,

$$F = -\frac{V^2}{2}\frac{dC}{dx} \qquad \textit{(general force expression)} \quad (2\text{-}4)$$

The above equation can also be re-evaluated and expressed as,

$$F = -\frac{dE}{dx}$$

This suggests that positive mechanical work done on the actuator reduces its energy. While pulling with a force F in the direction of x does positive mechanical work on the actuator, it forces the actuator to do twice that much work out of its electrical port

thus reducing its energy. This is a consequence of the constitutive relation governing the electrical port and the energy balance equation is still satisfied.

$$F + V^2 \frac{dC}{dx} = \frac{d}{dx}\left(\frac{C(x)V^2}{2}\right) = \frac{V^2}{2}\frac{dC}{dx}$$

2.2.2 Parallel plate electrostatic actuators

Parallel plate actuators consist of two parallel plate electrodes that can move with respect to each other just as shown in Figure 2-4. Relative motion of the electrodes changes the capacitor gap and hence produces a *dC/dx*. As before, the general equation for force holds.

$$F = -\frac{V^2}{2}\frac{dC}{dx}$$

where,

$$C(x) = \frac{Ak\varepsilon_o}{x} \tag{2-5}$$

and A is the area of the parallel plates.

$$F = \frac{Ak\varepsilon_o V^2}{2x^2} \tag{2-6}$$

As the above equation indicates, parallel plate actuators are nonlinear with motions in x and exert a force that is both a function of x and voltage.

2.2.2.1 Pull in

When connected to a linear spring (Figure 2-5), the nonlinear behavior of parallel plate actuators makes them prone to what is called "pull in".

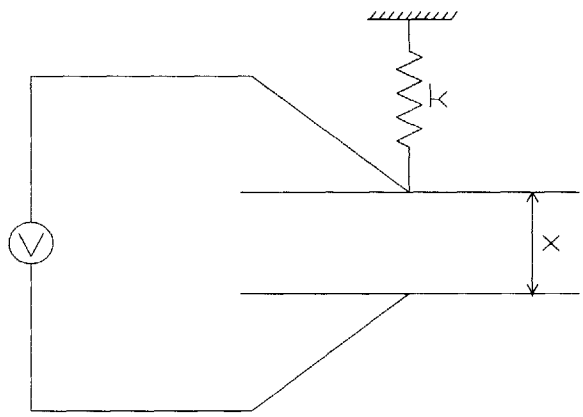

Figure 2-5. *Schematic of a parallel plate electrostatic actuator pulling against a spring of constant k.*

Given an initial relaxed-state gap of $x=g_o$, the following is the force balance condition for such an actuator spring system.

$$k(g_o - x) = \frac{A\varepsilon V^2}{2x^2} \qquad \textit{(force balance)} \quad (2\text{-}7)$$

Pull in occurs within the range where a perturbation δx from equilibrium in x cause a larger perturbation in the actuator force than it does in the spring force.

$$\left|\frac{d}{dx}\left(\frac{A\varepsilon V^2}{2x^2}\right)\delta\right|x \geq \left|-k\delta x\right|$$

In this unstable region the actuator plates, if perturbed open, will swing open into the stable region and re-approach to equilibrium. If perturbed closed they will slam shut, which is the inevitable result of this instability. The system transitions to the unstable range when,

$$\frac{A\varepsilon V_o^{\,2}}{x^3} = k \tag{2-8}$$

Simultaneous evaluation with the force balance equation results in

$$x = \frac{2g_o}{3} \tag{2-9}$$

Therefore, the nonlinear behavior of parallel plate actuators limits their stable range of operation to within one third of the starting gap as fabricated. Not all electrostatic actuators suffer from this instability. In comparison combdrive actuators achieve a constant *dC/dx* with position due to their design.

2.2.3 Combdrive electrostatic actuators

Combdrive actuators consist of two electrodes with interdigitated teeth as shown in the SEM photo in Figure 2-6. They are widely used in MEMS applications to generate

in-plane and out of plane motion[16]. Unlike parallel plate parallel plate actuators, relative motion of the electrodes causes a change in the capacitor area and hence produces a constant dC/dx. Capacitor gap g, shown in Figure 2-7, does not change with x.

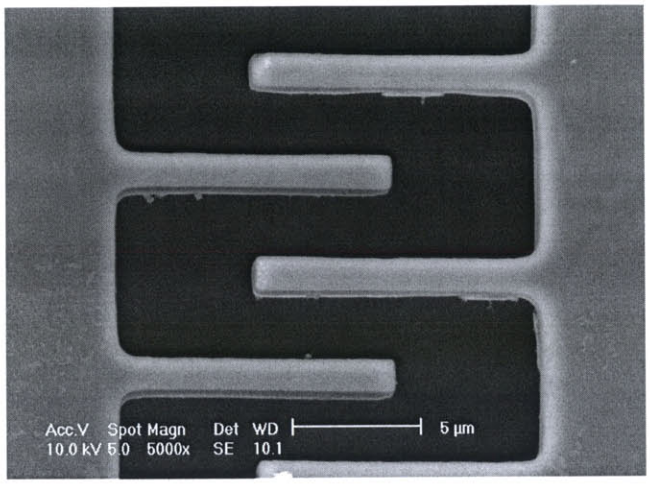

Figure 2-6. *SEM of a combdrive actuator showing the interdigitated teeth*

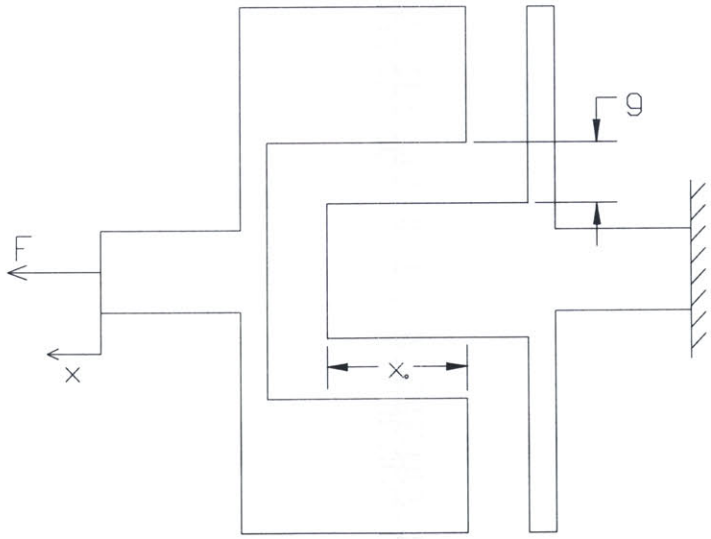

Figure 2-7. *Schematic of a combdrive electrostatic actuator. Only one comb tooth is shown for simplicity. In practice many comb teeth are used (dimmed lines). x_o is the amount of interdigitation as fabricated.*

As before, the general equation for force holds.

$$F = -\frac{V^2}{2}\frac{dC}{dx}$$

$$C(x) = \frac{2ntx_o k\varepsilon_o}{g} - \frac{2ntxk\varepsilon_o}{g} \tag{2-10}$$

where n is the number of comb teeth, t is the thickness of the device layer out of the page, g is the gap between the combdrive teeth, and x_o is the amount of interdigitation at the relaxed-state. Please refer to Figure 2-7. Combdrive actuators are linear, in fact, constant, with x and exert a constant force that is function of voltage.

$$F = \frac{nk\varepsilon_o t}{g}V^2 = const \cdot V^2 \tag{2-11}$$

2.2.4 Comparison of parallel plate and combdrive actuators

Parallel plate and combdrive actuators are both widely used in MEMS applications. Each has its own advantages and disadvantages. The primary difference is that combdrive actuators exert a linear force with respect to displacement while parallel plate actuators are highly nonlinear. It can be shown, however, that given the same feature fabrication resolution and device dimensions, parallel plate actuators can exert

twice the force of combdrive actuators for the same drive voltage. Given a device thickness of t and width w the force per voltage applied for parallel plate actuators is:

$$\frac{F}{V^2} = \frac{ktw\varepsilon_o}{2x^2} \tag{2-12}$$

where w is the width of the plate.

For a given w, the minimum x will achieve the largest force for applied voltage. Setting this to the minimum fabrication resolution r_o will yield the following equation.

$$\frac{F}{V^2} = \frac{ktw\varepsilon_o}{2r_o^2}$$

The force per applied voltage for the combdrive is given by:

$$\frac{F}{V^2} = \frac{nkt\varepsilon_o}{g} \tag{2-13}$$

where g is the gap between the combdrive teeth and n is the number of teeth.

Similarly for combdrive actuators the minimum g set to the minimum fabrication resolution r_o and the maximum n will yield the largest force per applied voltage. The maximum n can be achieved by setting the width and gap of the combdrive teeth to smallest possible dimension of r_o, thus packing the most number of teeth in a given width w. Given a combdrive width w, $n_{max}=w/4r_o$. Using these values, the following equations

give the maximum force per voltage attainable with each actuator given the same size and fabrication constraints.

$$\frac{F_{plate}}{V_{plate}^{2}} = \left(\frac{kt\varepsilon_o}{r_o}\right)\frac{w}{2r_o} \qquad \frac{F_{comb}}{V_{comb}^{2}} = \left(\frac{kt\varepsilon_o}{r_o}\right)\frac{w}{4r_o}$$

The parallel plate actuators can generate twice the force per voltage of that of the combdrives. However, combdrive actuators are linear and have longer range of motion. Since in this application linear performance and range are both important, the combdrive actuator is chosen over the parallel plate despite its lack of relative compactness and strength.

The dimensions of the combdrive, such as number of comb teeth and the gap between the comb teeth are designed to achieve a desired strength vs. drive voltage. The strength of the combdrive is designed to match the stiffness of the flexure mechanism it is pulling against. Please refer to end of the flexure design section 2.3 and Table 2-1 on page 61 for these values and justification. One consideration is that the actuator not be too strong so that small resolution in motion vs. voltage can be achieved. Yet the actuator must be strong enough to fully close the arms within a specified voltage range. Since low actuation voltage is target goal of this design, a drive voltage of approximately 25 V to fully close the nanotweezers is chosen as a target starting point for the preliminary design. This value is roughly half way between that of Lieber's nanotweezers (8.3V), which is ideally achievable, and Kim's microgrippers (45V), which is likely to be achievable. Given the test results from this design, which are discussed in section Chapter

4, it is fortunately possible to decrease the required drive voltage even further in future generations.

2.3 Modeling of the Flexure Behavior

In addition to serving as a linear spring for the actuator to pull against, flexure mechanisms allow for guided motion between two objects with constrained directions of compliance. A properly designed flexure will guide motion along a single intended direction while constraining it in all others. A hammock flexure such as the one shown in Figure 2-8 is commonly used. It allows translation in the x direction of the center piece. Hammock type flexures are used because they do a good job of constraining any motion but translation along the x direction.

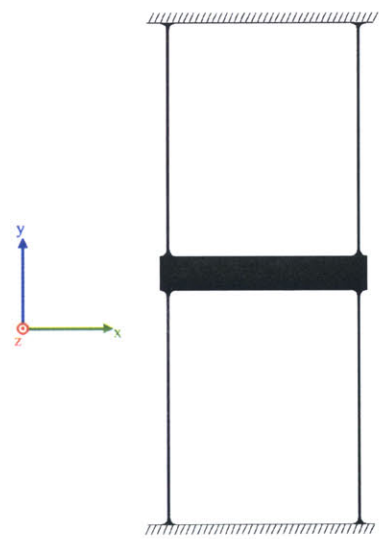

Figure 2-8. *Schematic of a typical hammock flexure.*

In an earlier design, the flexure for the nanotweezer arm was also made of a single half hammock flexure equivalent to the lower half of the one shown in Figure 2-8. The

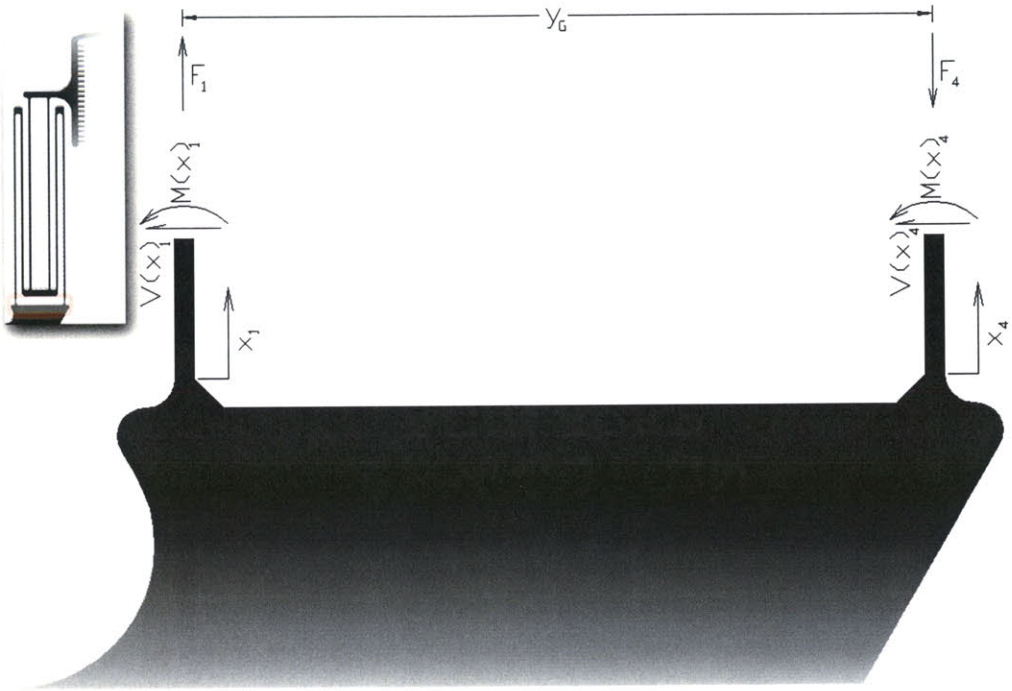

Figure 2-14. *Force and moment diagram for beam set A. Insert on the top left corner indicates the section of the flexure mechanism that is depicted in the diagram. This is the anchor section of flexure mechanism that connects beam set A to the substrate. The x coordinate system originates from the anchor points. The positive direction for deflections of the beam is horizontal and to the left.*

The force and moment diagram for the smaller junction that connects beam #1 with beam #2 is shown in Figure 2-15. For this junction,

$$\sum F_{Horizontal} = V_1(L_a) - V_2(0) = 0$$

$$V_1(L_a) = A_1 = V_2(0) = A_2$$

$$A_1 = A_2$$

$$\sum F_{Vertical} = -F_1 + F_2 = 0$$

Beam #1 and beam #4 form the first, grounded symmetric set, set A. Beam #2 and beam #5 form the second, floating symmetric set, set B. Beam #3 and beam #6 form the final, symmetric set C that connects to the actuator. Beam #2 is mounted in series to beam #1 and similarly beam #5 is mounted in series to beam #4. Beam set C is a half hammock flexure that is mounted in series to the rest of the mechanism at the junction where beam #2 and beam #5 come together. This junction from here on is referred to as the **larger** junction. Under the approximation of axially rigid beams, hammock type flexures such as the one in Figure 2-8 and beam set C, do not allow relative rotation between their two ends and incorporate a zero rotation boundary condition for both. It is important to note that the beam sets A and B, however, are not half hammock flexures. The reason is that the junctions (circled in red in Figure 2-10) that connect beam set A with B, from here on referred to as the **smaller** junctions, are free to rotate and hence do not satisfy the necessary zero rotation boundary condition. Therefore, this flexure mechanism is not a true hammock type flexure and is not as stiff against rotation. While it is possible to add geometry to connect these smaller junctions and prevent their rotation, this would increase the size of the arms and introduce additional inertia within the flexure mechanism. Fabrication experience has also shown that adding large area connecting pieces inside of a compliant mechanism increases the risk that it will break. As a result the smaller junctions between sets A and B were left free to rotate. However, as the following analysis will show, under certain conditions that are satisfied by this design, the mechanism approximates the desired pure translation performance of the hammock type flexures quite well.

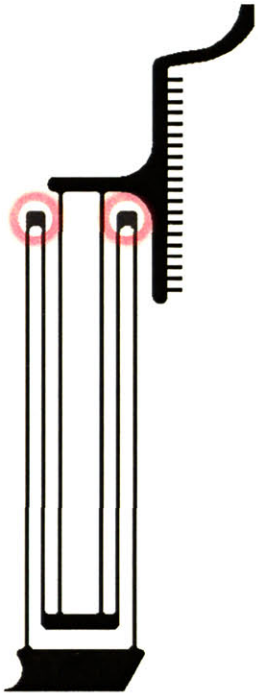

Figure 2-10. *Diagram highlighting the smaller junctions that connect beam set A with B*

For the analysis of the proposed flexure mechanism the following governing equations for beam bending are used. Please refer to the notation of an incremental beam section shown in Figure 2-11. Since the two arms are symmetric, the analysis is carried out for the left arm only.

$$q(x) = 0 \tag{2-14}$$

$$V(x) = A \tag{2-15}$$

$$M(x) = Ax + B \tag{2-16}$$

$$\theta(x) = \frac{1}{EI}\left[\frac{Ax^2}{2} + Bx + C\right] \tag{2-17}$$

$$v(x) = \frac{1}{EI}\left[\frac{Ax^3}{6} + \frac{Bx^2}{2} + Cx + D\right] \tag{2-18}$$

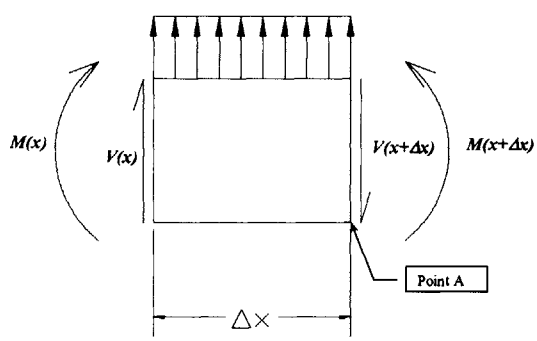

Figure 2-11. *Schematic showing positive force and moment notation for an elemental beam section*

The displacement *v(x)* of each beam is along the same direction as the distributed load *q(x)*. To prevent cluttering of diagrams the positive notation for *v(x)* and *θ(x)* are not indicated in the figures. Instead, for easy orientation, all coordinate systems are chosen so

beams for this design were 1 μm thick to achieve the desired stiffness. However, this proved to be too thin to survive the fabrication process and yield was too low. Instead, a new design incorporating flexures made of 2 μm beams was implemented. To compensate for the increased stiffness of each beam, the second design used multiple flexures mounted in series to reduce overall stiffness. This design is shown in Figure 2-9. It is loosely similar to mounting three half hammock flexures in series and folding them inside each other to save space. Each flexure arm has three symmetric equivalent beam sets mounted in series to each other to produce a more compliant spring.

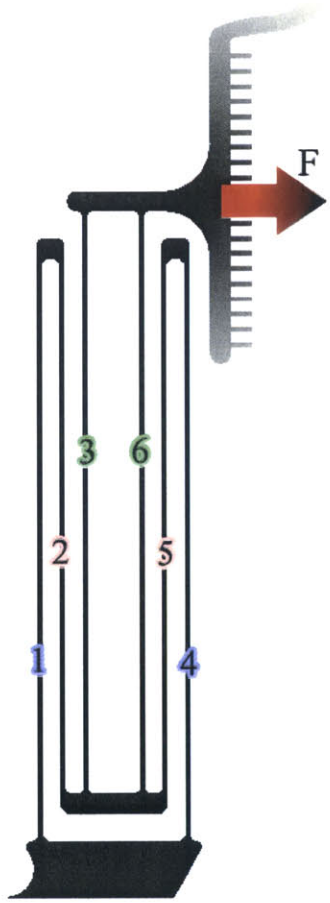

Figure 2-9. *Diagram indicating annotation for each beam comprising the nanotweezers arm flexure mechanism. Color coordination of the annotation indicates a symmetric set: blue for set A, red for set B, and green for set C*

Figure 2-13 indicates the positive notation for the forces and moments in beams #3 and #6 making up set C. The insert in the top left corner of the figure indicates the location of the larger junction relative to the rest of the mechanism. x coordinates originate at the larger junction.

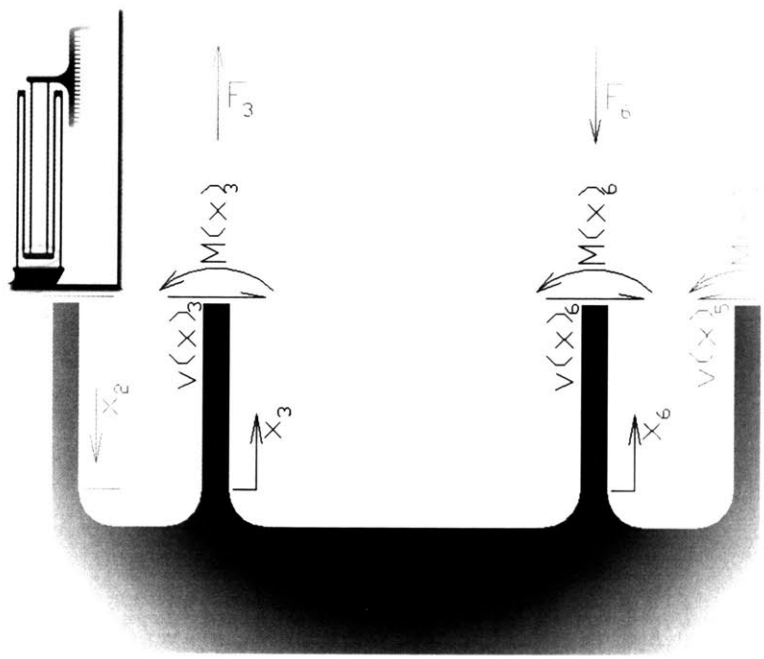

Figure 2-13. *Force and moment diagram for beam set C. Insert on the top left corner indicates the section of the flexure mechanism that is depicted in the diagram. This section is the larger junction that connects beam set B with C. The x coordinate system originates from the larger junction. The positive direction for deflections of the beam is horizontal and to the left.*

L_c is the length of both beams. A zero deflection and zero rotation boundary condition is used at each $x_i=0$ for both beams.

$$V_3(0)=D_3= V_6(0)=D_6=0$$

$$D_3= D_6=0$$

$$\theta_3(0)=C_3=\theta_6(0)=C_6=0$$

$$C_3= C_6=0$$

From force balance in the horizontal direction,

$$V_3(L_c)+ V_6(L_c)=A_3+ A_6=F_A$$

where F_A is the actuator force.

Using symmetry,

$$V_3(L_c)=V_6(L_c)$$

$$A_3= A_6=F_A/2$$

$$\theta_3(L_c)=\frac{1}{EI}\left[\frac{A_3L_c^{\ 2}}{2}+B_3L_c\right]=\frac{1}{EI}\left[\frac{F_AL_c^{\ 2}}{2}+B_3L_c\right]=0$$

$$B_3=-\frac{F_AL_c}{2}$$

again by symmetry,

$$B_6=-\frac{F_AL_c}{2}$$

$$v_3(L_c)=v_6(L_c)=\frac{1}{EI}\left[\frac{F_AL_c^{\ 3}}{12}-\frac{F_AL_c^{\ 3}}{8}\right]=-\frac{F_AL_c^{\ 3}}{24EI}$$

Thus for a given force F_A this half hammock flexure allows a deflection of $\frac{F_A L_c^3}{24EI}$ between its two ends with an effective spring constant of $k = \frac{24EI}{L_c^3}$. Note that the axial forces F_3 and F_6 do not affect the horizontal deflection. They are equal opposing forces. There are no vertical forces generated on the flexure by the actuator. They only impose a moment on the larger junction. For the interface between the half hammock flexure and the rest of the mechanism a simple horizontal force and moment pair of F_A and $F_A L_c$ will be used to represent the transfer of load from the actuator (please see Figure 2-17). This accounts for the moment exerted by the axial forces as well.

Unlike beam set C, beam sets A and B can not be analyzed independently of each other. What is to follow is beam bending analysis applied to beam sets B and C with careful matching of the boundary conditions at the junctions between the beams. Starting with the anchor points of the flexure mechanism to ground, Figure 2-14 indicates the coordinate, force, and moment notations. L_a is the length of beams #1 and #4 making up set A. A zero deflection and zero rotation boundary condition is used at each $x_i=0$ for both beams.

$$\theta_1(0) = \theta_4(0) = \frac{1}{EI}[C_1] = \frac{1}{EI}[C_4] = 0$$

$$C_1 = C_4 = 0$$

$$v_1(0) = v_4(0) = \frac{1}{EI}[D_1] = \frac{1}{EI}[D_4] = 0$$

$$D_1 = D_4 = 0$$

that the positive direction for $v(x)$ is always pointing to the left and in the opposite direction from the actuator. Any deflection denoted with small cap v is in this direction. The positive notation for the rotation θ is defined by $\hat{\theta} = \hat{x} \times \hat{v}$. A right handed system is used. Positive notation for moment summation is always pointing out of the page. Since all beams are made of the same material and have the same cross section both the young's modulus E and the moment of Inertia I are the same for all beams in the system.

In the analysis, beam set C (Figure 2-12), which is a hammock type flexure, is treated as an independent flexure mechanism mounted in series with the rest of the system at the larger junction. The motion and force transfer between the two ends of this half hammock flexure is independent of its interaction with the other beams.

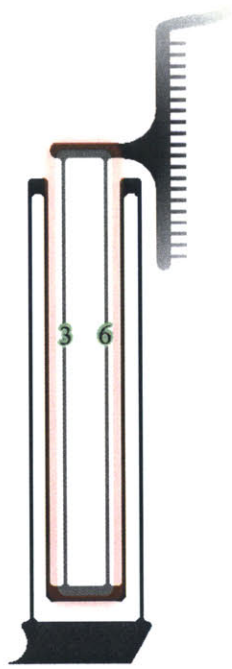

Figure 2-12. *Diagram highlighting the half hammock beam set C. This part of the flexure mechanism forms a hammock type flexure and can be analyzed independent of the other beams.*

$$F_1 = F_2 = F_{12}$$

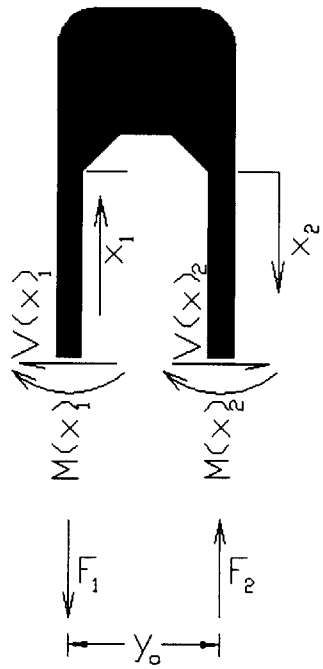

Figure 2-15. *Force and moment diagram for the junction of beam 1 and 2. This is one of the smaller junctions that connects beam set A with B. This junction is the one on the left indicated in Figure 2-10. Diagram highlighting the smaller junctions The x coordinates point in opposite directions. The positive direction for deflections of the beam is horizontal and to the left.*

where F_{12} is the axial force in beams #1 and #2. Note that given this notation the force is tensile for beam #1 and compressive for beam #2. Because F_1, F_2 and V_1, V_2 are equal and opposite force pairs, the moment can be taken with respect to any point in the diagram.

$$\sum M = -M_1(L_a) - M_2(0) + F_{12}y_o = 0$$

$$M_1(L_a) = A_1L_a + B_1 = -M_2(0) + F_{12}y_o$$

$$A_1L_a + B_1 = -B_2 + F_{12}y_o$$

$$\theta_1(L_a) = \frac{1}{EI}\left[\frac{A_1 L_a^{\ 2}}{2} + B_1 L_a + C_1\right] = -\theta_2(0) = -\frac{1}{EI}[C_2]$$

$$\frac{A_1 L_a^{\ 2}}{2} + B_1 L_a = -C_2$$

$$v_1(L_a) = \frac{1}{EI}\left[\frac{A_1 L_a^{\ 3}}{6} + \frac{B_1 L_a^{\ 2}}{2} + C_1 L_a + D_a\right] = v_2(0) = \frac{1}{EI}[D_2]$$

$$\frac{A_1 L_a^{\ 3}}{6} + \frac{B_1 L_a^{\ 2}}{2} = D_2$$

Similarly for the smaller junction that connects beam #4 with beam #5 (Figure 2-16):

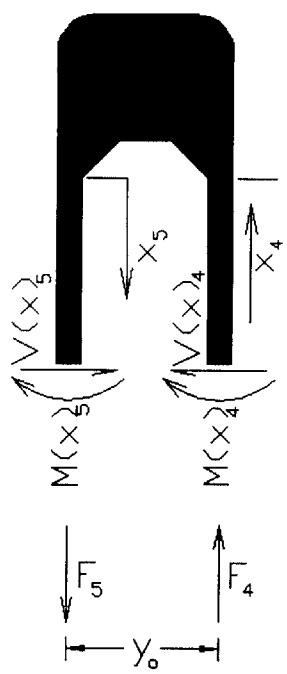

Figure 2-16. *Force and moment diagram for the junction of beam 4 and 5. This is one of the smaller junctions that connects beam set A with B. This junction is the one on the right indicated in Figure 2-10. The x coordinates point in opposite directions. The positive direction for deflections of the beam is horizontal and to the left.*

$$\sum F_{Horizontal} = V_4(L_a) - V_5(0) = 0$$

$$V_4(L_a) = A_4 = V_5(0) = A_5$$

$$A_4 = A_5$$

where F_{45} is the axial force in beams #4 and #5. In this case, however, the force is compressive for beam #4 and tensile for beam #5. It is important to note that while the entire flexure mechanism is symmetric, the axial loading of the beams can be asymmetric.

$$\sum F_{Vertical} = -F_4 + F_5 = 0$$

$$F_4 = F_5 = F_{45}$$

$$\sum M = -M_4(L_a) - M_5(0) + F_{45}y_o = 0$$

$$M_1(L_a) = A_4L_a + B_4 = -M_5(0) + F_{45}y_o$$

$$A_4L_a + B_4 = -B_5 + F_{45}y_o$$

$$\theta_4(L_a) = \frac{1}{EI}\left[\frac{A_4L_a^{\ 2}}{2} + B_4L_a + C_4\right] = -\theta_5(0) = -\frac{1}{EI}[C_5]$$

$$\frac{A_4L_a^{\ 2}}{2} + B_4L_a = -C_5$$

$$v_4(L_a) = \frac{1}{EI}\left[\frac{A_4L_a^{\ 3}}{6} + \frac{B_4L_a^{\ 2}}{2} + C_4L_a + D_4\right] = v_5(0) = \frac{1}{EI}[D_5]$$

$$\frac{A_4L_a^{\ 3}}{6} + \frac{B_4L_a^{\ 2}}{2} = D_5$$

As mentioned before, for the larger junction that connects beam set B with C, the loading from beam set C is represented as a force moment pair as shown in Figure 2-17.

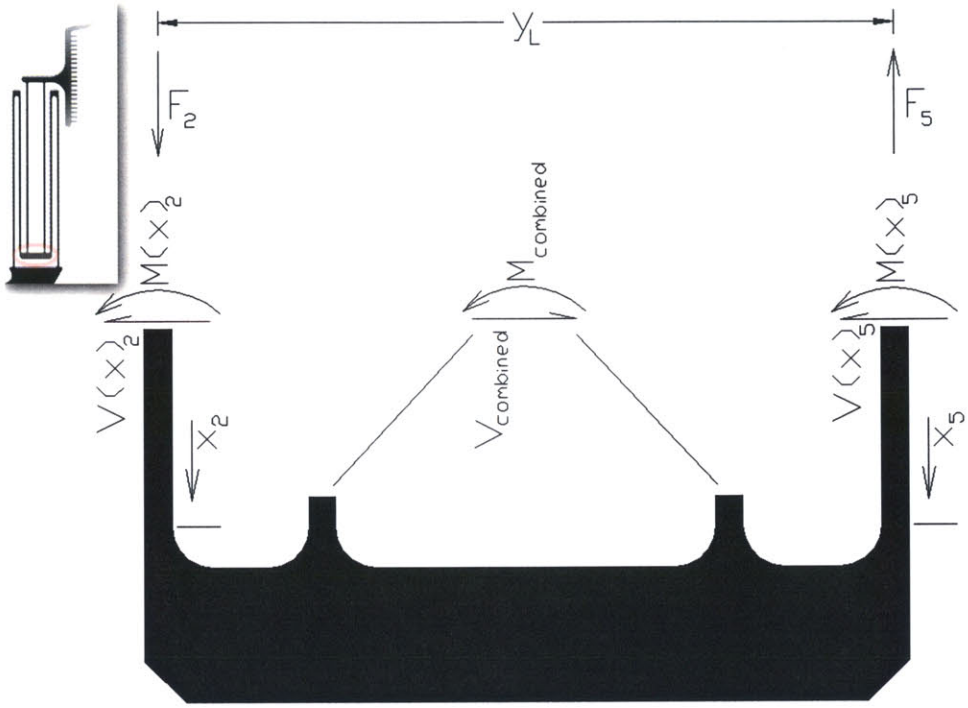

Figure 2-17. *Force and moment diagram for the larger junction connecting beam set B with C. Insert on the top left corner indicates the section of the flexure mechanism that is depicted in the diagram. The loading from beam set C on the junction is represented as a force moment pair. The positive direction for deflections of the beam is horizontal and to the left.*

$$V_{combined}=F_A$$

$$M_{combined}=-F_A L_c$$

L_b is the length of beams #2 and #5 making up set B.

$$\sum F_{Horizontal} = -V_2(L_b) - V_5(L_b) + F_A = 0$$

$$V_2(L_b) + V_5(L_b) = A_2 + A_5 = F_A$$

An overall vertical force balance on the entire flexure mechanism including all three beam sets results in the following expression.

$$\sum F_{Vertical} = -F_1 + F_4 = -F_{12} + F_{45} = -F_2 + F_5 = 0$$

$$F_2 = F_5 = F_{12} = F_{45} = F_{axial}$$

From moment balance of the larger junction:

$$\sum M = M_2(L_b) + M_5(L_b) - F_A L_c + F_{axial} y_L = 0$$

$$M_2(L_b) + M_5(L_b) = A_2 L_b + B_2 + A_5 L_b + B_5 = F_A L_c - F_{axial} y_L$$

$$A_2 L_b + B_2 + A_5 L_b + B_5 = F_A L_c - F_{axial} y_L$$

Since both beam #2 and #5 connect to the same junction:

$$\theta_2(L_b) = \theta_5(L_b)$$

$$\frac{A_2 L_b^{\ 2}}{2} + B_2 L_b + C_2 = \frac{A_5 L_b^{\ 2}}{2} + B_5 L_b + C_5$$

$$v_2(L_b) = v_5(L_b)$$

$$\frac{A_2 L_b^{\ 3}}{6} + \frac{B_2 L_b^{\ 2}}{2} + C_2 L_b + D_2 = \frac{A_5 L_b^{\ 3}}{6} + \frac{B_5 L_b^{\ 2}}{2} + C_5 L_b + D_5$$

An additional kinematic constraint is required to fully define this system and solve for the individual coefficients. For this, it is assumed the beams do not buckle and that any axial displacement due to the axial stress and strain of the beams is negligible compared to displacement caused by bending. This is the previously mentioned axially rigid assumption. Under this assumption, any rotation of the larger junction between the beam sets B and C will cause vertical motion of the ends of beam #2 and #5. Please see Figure 2-18). This motion is in turn accommodated by a rotation of the smaller junctions that connect beam #2 to #1 and beam #5 to #4. Please see Figure 2-18.

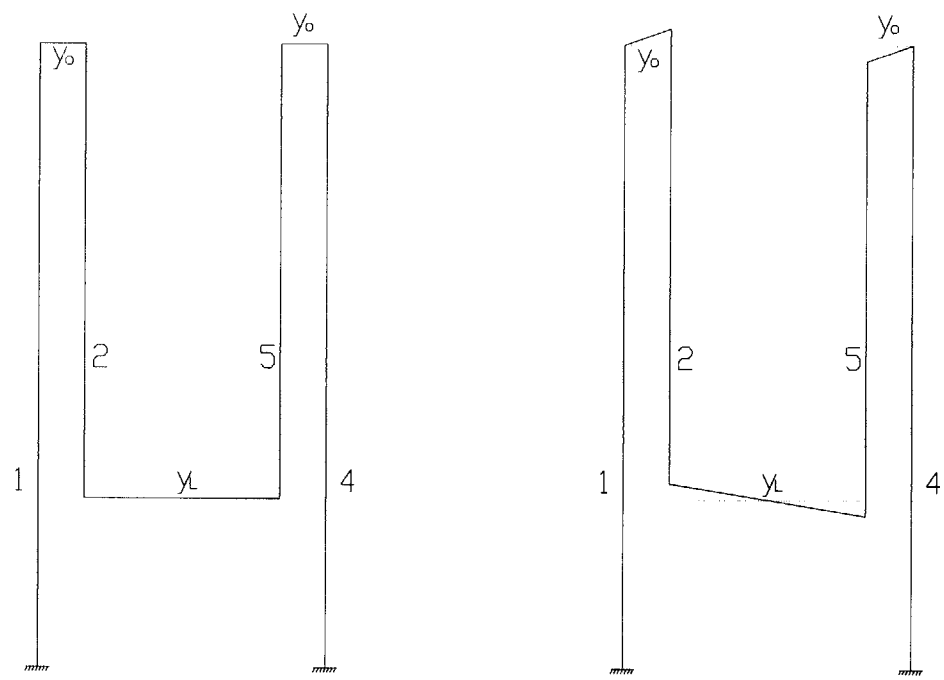

Figure 2-18. *Schematic of kinematic constraints for the beam set junctions. Using the axially rigid beam assumption, any rotation of the larger junction (of length y_L) must be completely accommodated for by consequent rotations of the small junctions (of length y_o).*

Therefore a kinematic constraint of the following form can be applied.

$$\theta_2(0)y_o + \theta_5(0)y_o = -\theta_2(L_b)y_L = -\theta_5(L_b)y_L \tag{2-19}$$

$$(C_2 + C_5)y_o = -\left(\frac{A_2 L_b^{\ 2}}{2} + B_2 L_b + C_2\right)y_L = -\left(\frac{A_5 L_b^{\ 2}}{2} + B_5 L_b + C_5\right)y_L$$

The latter equations fully define the deflection of the flexure mechanism under static load from the actuator. MathCAD, a symbolic manipulation software, was used to solve all of the derived simultaneous governing equations. Results from MathCAD:

$$A_1 = A_4 = \frac{1}{2}\cdot F_A$$

$$B_1 = B_4 = \frac{-1}{4}\cdot F_A \cdot \frac{\left(-L_b^{\ 2} + 2\cdot L_a\cdot L_b + L_a^{\ 2}\right)\cdot y_L^{\ 2} + \left(4\cdot L_a^{\ 2} + 2\cdot L_b^{\ 2} - 4\cdot L_b\cdot L_c\right)\cdot y_o\cdot y_L + 4\cdot L_a^{\ 2}\cdot y_o^{\ 2}}{(L_b + L_a)\cdot y_L^{\ 2} + 4\cdot y_o\cdot L_a\cdot y_L + 4\cdot L_a\cdot y_o^{\ 2}}$$

$$A_2 = A_5 = \frac{1}{2}\cdot F_A$$

$$B_2 = B_5 = \left[\left(\frac{-1}{2}\cdot y_L\cdot y_o - \frac{1}{4}\cdot y_L^{\ 2}\right)\cdot L_a^{\ 2} + \left[(2\cdot L_c - 2\cdot L_b)\cdot y_o^{\ 2} + (-L_b + L_c)\cdot y_L\cdot y_o\right]\cdot L_a - \frac{1}{4}\cdot y_L^{\ 2}\cdot L_b^{\ 2}\right]\cdot \frac{F_A}{\left(y_L^{\ 2} + 4\cdot y_L\cdot y_o + 4\cdot y_o^{\ 2}\right)\cdot L_a + y_L^{\ 2}\cdot L_b}$$

$$C_2 = C_5 = \frac{1}{4}\cdot y_L\cdot L_a\cdot L_b\cdot F_A \cdot \frac{L_a\cdot y_L - y_L\cdot L_b + (2\cdot L_b - 4\cdot L_c)\cdot y_o}{\left(y_L^{\ 2} + 4\cdot y_o\cdot y_L + 4\cdot y_o^{\ 2}\right)\cdot L_a + y_L^{\ 2}\cdot L_b}$$

$$D_2 = D_5 = \frac{-1}{24}\cdot L_a^{\ 2}\cdot F_A \cdot \frac{\left(L_a^{\ 2} + 4\cdot L_a\cdot L_b - 3\cdot L_b^{\ 2}\right)\cdot y_L^{\ 2} + \left(4\cdot L_a^{\ 2} - 12\cdot L_b\cdot L_c + 6\cdot L_b^{\ 2}\right)\cdot y_o\cdot y_L + 4\cdot L_a^{\ 2}\cdot y_o^{\ 2}}{(L_b + L_a)\cdot y_L^{\ 2} + 4\cdot y_o\cdot L_a\cdot y_L + 4\cdot L_a\cdot y_o^{\ 2}}$$

$$F_{axial} = \frac{-1}{2}\cdot F_A \cdot \frac{\left[L_b^{\ 2} + (2\cdot L_a - 2\cdot L_c)\cdot L_b - L_a^{\ 2} - 2\cdot L_c\cdot L_a\right]\cdot y_L + 4\cdot L_b\cdot L_a\cdot y_o - 2\cdot L_a^{\ 2}\cdot y_o - 4\cdot y_o\cdot L_a\cdot L_c}{(L_a + L_b)\cdot y_L^{\ 2} + 4\cdot y_o\cdot L_a\cdot y_L + 4\cdot L_a\cdot y_o^{\ 2}}$$

As can be seen, the coefficients for each beam in a set are the same. This is due in part to the symmetry of the flexures. But it is also necessary to choose the positive direction for the axial forces, internal shear forces, and internal moments as done in this document.

The following results from MathCAD, express the rotation and deflection of key points in symbolic form.

$$\theta_2(0)=\frac{\frac{1}{4}\cdot y_L\cdot L_a\cdot L_b\cdot F_A\cdot\frac{(2\cdot L_b-4\cdot L_c)\cdot y_o+L_a\cdot y_L-y_L\cdot L_b}{\left(4\cdot L_a\cdot y_o^{\,2}+4\cdot y_o\cdot L_a\cdot y_L+y_L^{\,2}\cdot L_b+L_a\cdot y_L^{\,2}\right)\cdot E\cdot I}}{}$$

$$\theta_2(L_b)=\frac{\frac{-1}{2}\cdot F_A\cdot y_o\cdot L_a\cdot L_b\cdot\frac{2\cdot L_b\cdot y_o-y_L\cdot L_b+L_a\cdot y_L-4\cdot y_o\cdot L_c}{\left(4\cdot L_a\cdot y_o^{\,2}+4\cdot y_o\cdot L_a\cdot y_L+y_L^{\,2}\cdot L_b+L_a\cdot y_L^{\,2}\right)\cdot E\cdot I}}{}$$

$$v_2(L_b)=\frac{\frac{-1}{24}\cdot F_A\cdot\left(4\cdot L_b\cdot L_a^{\,3}+L_a^{\,4}+L_b^{\,4}-6\cdot L_b^{\,2}\cdot L_a^{\,2}+4\cdot L_b^{\,3}\cdot L_a\right)\cdot y_L^{\,2}+\left(12\cdot L_b^{\,2}\cdot L_a^{\,2}-12\cdot L_b\cdot L_a^{\,2}\cdot L_c-8\cdot L_b^{\,3}\cdot L_a+4\cdot L_a^{\,4}+12\cdot L_b^{\,2}\cdot L_a\cdot L_c\right)\cdot y_o\cdot y_L+\left(-24\cdot L_b^{\,2}\cdot L_a\cdot L_c+16\cdot L_b^{\,3}\cdot L_a+4\cdot L_a^{\,4}\right)\cdot y_o^{\,2}}{\left[\left(L_b+L_a\right)\cdot y_L^{\,2}+4\cdot y_o\cdot L_a\cdot y_L+4\cdot L_a\cdot y_o^{\,2}\right]\cdot E\cdot I}$$

$\theta_2(0)$ is the rotation of the smaller junctions between beam sets A and B, highlighted in Figure 2-10. $\theta_2(L_b)$ and $v_2(L_b)$ are the rotation and deflection of the larger junction between beam sets B and C shown in Figure 2-13 and Figure 2-17.

Note that the ratio of the rotation of the larger junction to that of the smaller junctions simplifies to $\frac{\theta_2(L_b)}{\theta_2(0)}=\frac{y_o}{y_L}$. As this ratio gets very small, this flexure better approximates the pure translation behavior of hammock type flexure. In fact, for y_o equal to zero, there is no rotation of the larger junction. In this optimal case, the nanotweezers arms are in pure translation just like a hammock type flexure. In reality, it is not practical to make $y_o=0$ due to limitations in lithography and stress concentration caused by sharp curvatures. Accommodating the latter practical considerations, for this particular proposed flexure mechanism $\frac{\theta_2(L_b)}{\theta_2(0)}=\frac{y_o}{y_L}=\frac{12\mu m}{54\mu m}=0.22$. With this geometrical ratio, there is only a 2×10^{-4} radians rotation of the arms when they fully extended inwards to completely close the tips. Therefore, given the loading conditions, the designed flexure mechanism approximates the desired guided behavior of a hammock flexure quite well using a more compact design. The omission of a piece connecting the smaller junctions to

each other is justified and does not compromise the desired performance of the mechanism.

The over all value for the deflection δ_A, measured at the combdrive, is given by the following equation. This includes all three beam sets and takes into account the rotation of set C with respect to ground. δ_A is measured along the axis of actuation and is positive for the actuator pulling the arms inward. In other words, δ_A is aligned to the long axis of the combteeth.

$$\delta_A = -v_2(L_b) + \theta_2(L_b)L_c + \frac{F_A L_c^3}{24EI} \tag{2-20}$$

According to this equation it is expected to move each arm of the tweezers 2 μm and close the gap using a force F_A of 0.67 μN. A voltage of 27.5 V is required to achieve this. The starting target point for the required drive voltage to fully close the nanotweezer gap was 25V as discussed at the end of section 2.2.4. The actual measured voltage required to fully close the nanotweezer gap is less than this as will be discussed in section 4.2. The deflection vs. voltage performance of the flexure actuator pair is independent of its out of plane thickness. By collecting terms the equation for δ_A can be re-expressed as,

$$\delta_A = const.\left(\frac{F_A}{EI}\right) = const.\left(\frac{\frac{nk\varepsilon_o tV^2}{g}}{E\frac{th^3}{12}}\right) = const\left(\frac{nk\varepsilon_o V^2}{Eh^3 g}\right)$$

where t is the out of plane thickness of the nanotweezers. As can be seen t cancels out of the equation. The thickness of the device can therefore be independently adjusted to achieve desired in-plane and out of plane spring constants without affecting the deflection vs. voltage characteristic of the devices.

For a flexure mechanism that has an out of plane thickness of 10 μm, the in-plane spring constant measured at the center of the combdrive is 0.335 N/m based on this analytical model. The spring constant at the same location based on finite element analysis (FEA) is 0.328 N/m. This flexure is matched with an actuator with the characteristics shown in Table 2-1. With this flexure actuator pair a ~2 nm resolution in motion is possible with a 0.01V resolution in drive voltage. The latter is a predicted value and does not take into account noise and variation of device performance due to fatigue and environmental parameters.

Parameter	Value
Number of comb teeth	20
Gap between comb teeth	2 μm
Thickness of comb teeth	2 μm
Target range	2 μm
Required drive voltage to extend full range and close tips	27.5 V
Force at full range drive voltage	.670 μN

Table 2-1. *Table showing characteristics of the combdrive actuator. A range of 2 μm is required of each arm to close the 4 μm gap of the nanotweezers.*

At the tip, the out of plane spring constant is 0.3 N/m based on FEA model, which is well within the range of 0.05-1N/m for contact mode AFM probes. Figure 2-19 shows an FEA model of the deflection of the tip due to an out of plane force. This deflection is

due to a combination of shear, bending, and torsional strain of the structure and is too complex to quantify analytically.

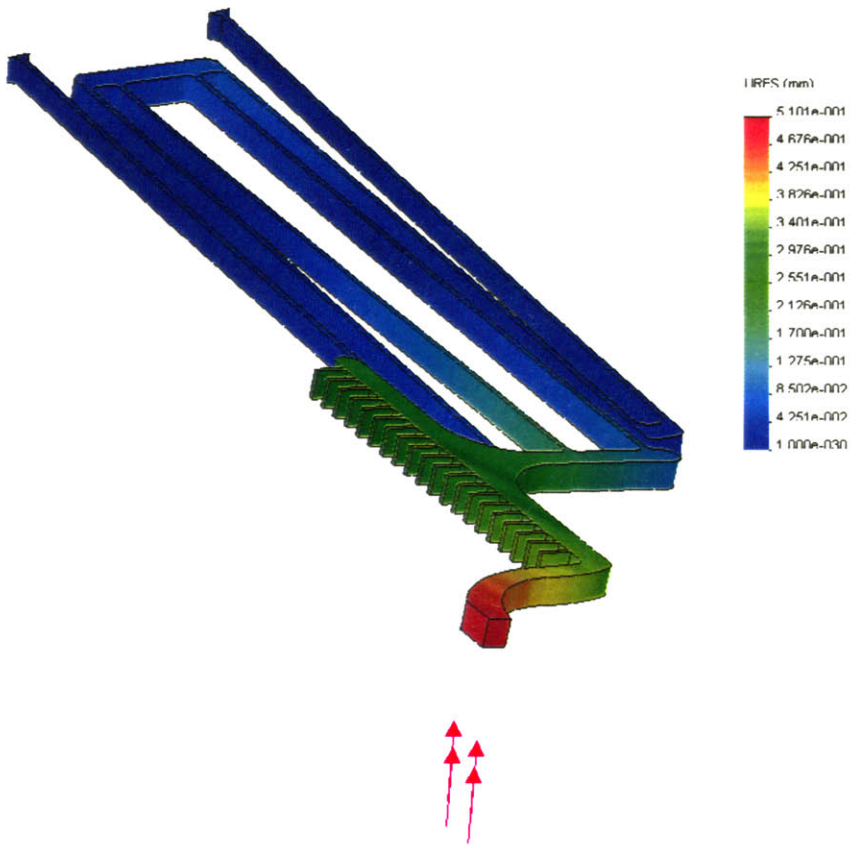

Figure 2-19. *FEA model of the left nanotweezer arm subjected to an out of plane force at the tip. The model shows exaggerated deflection. This is a 1000x model where the color bar shows displacement in units of mm corresponding to units of μm in real life. A model force of 0.15 N is applied corresponding to real life force of* 1.5×10^{-7}*N.*

Using FEA, in-plane spring constant along the direction of δ_A but measured at the tip is 0.28 N/m. This is slightly more compliant than the center of the combdrive. The structure could have been made stiffer in this direction and then paired to a stronger actuator with more comb teeth. However, a more a compliant structure is less likely to over squeeze and the damage objects in an open loop scheme where there is no feedback on whether the tips have closed on an object. As a starting point this spring constant was

matched to that of the AFM probe as well. In not so rigorous terms, it is less likely for an object that does not get damaged by the AFM probe to be damaged by manipulation with a flexure of the same spring constant and an actuator that has been matched for it. In-plane spring constant in the direction perpendicular to δ_A is 3.0 N/m. Motion in this direction is not desired. To obtain the spring constants at the tip, three different force and deflection values were obtained from the FEA models for each direction. The results are summarized in Table 2-2.

Along δ_A		
Force	**Deflection**	**Spring constant**
0.15 μN	0.54 μm	0.28 N/m
0.30 μN	1.07 μm	0.28 N/m
0.05 μN	0.18 μm	0.28 N/m
Perpendicular to δ_A		
Force	**Deflection**	**Spring constant**
0.15 μN	0.05 μm	3.0 N/m
0.30 μN	0.10 μm	3.0 N/m
0.05 μN	0.017 μm	2.9 N/m
Out of plane		
Force	**Deflection**	**Spring constant**
0.15 μN	0.5 μm	0.3 N/m
0.30 μN	1.0 μm	0.3 N/m
0.05 μN	0.17 μm	0.3 N/m

Table 2-2. *Table showing various displacement results and subsequent spring constants derived from FEA model. All spring constants are measured at the tip.*

The AFM can also scan in tapping mode, where a piezo actuator vibrates the AFM probe at its resonance frequency. Force interaction between the tip and sample affects the amplitude of the oscillation, which can be measured. Typical resonance frequency for tapping mode AFM probes is in the range of 50-500kHz. For this flexure based nanotweezer arm, the 6th and 7th modes of vibration generate out of plane motion at

frequencies of 59.314 kHz and 56.113 kHz respectively, which is suitable for tapping mode sensing. These shapes of these modes are shown in Figure 2-20 and Figure 2-21 respectively.

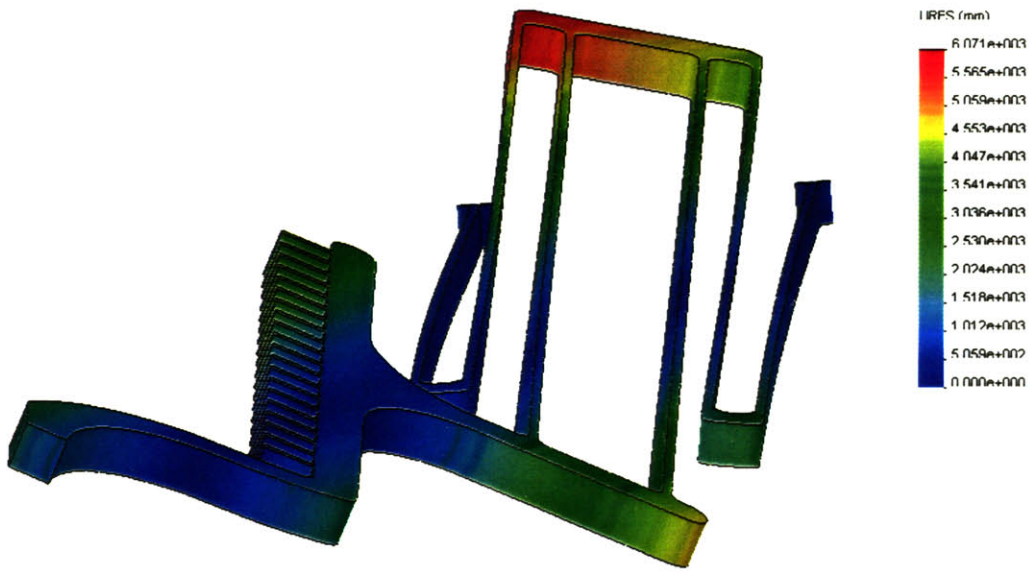

Figure 2-20. *FEA diagram showing the 6th resonance mode of vibration of the nanotweezer arm. Deformation has been exaggerated for visualization.*

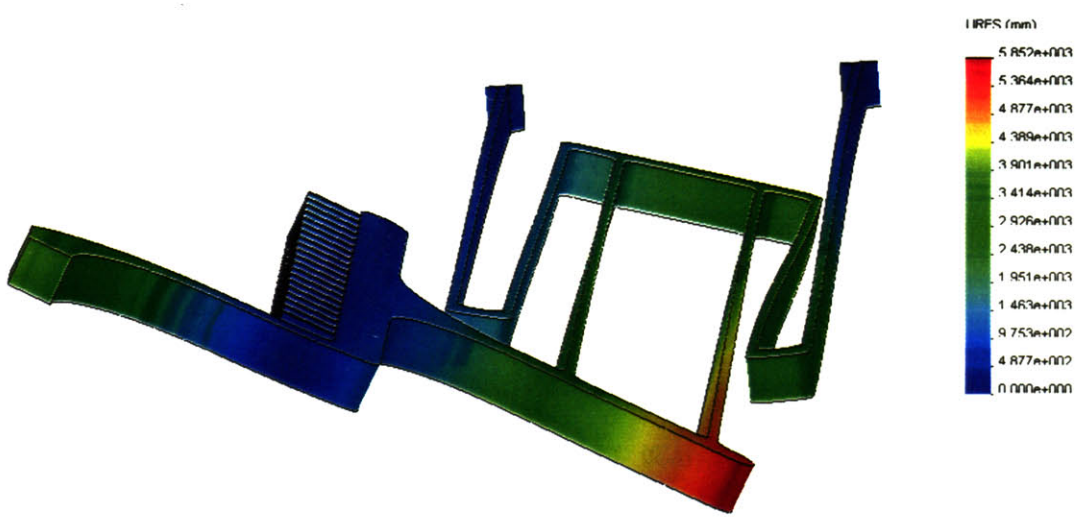

Figure 2-21. *FEA diagram showing the 7th resonance mode of vibration of the nanotweezer arm. Deformation has been exaggerated for visualization.*

The 7th mode of vibration is better suited for tapping mode operation as it generates larger out of plane motion near the tip region. In addition, in the 6th mode of vibration the larger junction that connects beam set B with C has larger amplitude of oscillation than the tip section. It is not clear whether in practice the two modes can be excited independently. However, an approach angle between the nanotweezers and the sample can prevent the rest of the structure from slamming into the sample in either the 6th or 7th modes. The 8th mode of vibration has a frequency of 89.396 kHz and consists purely of in-plane motion. Therefore, tapping mode operation with this design is feasible.

The purpose of all the nanotweezer designs that were fabricated was to map out possible ranges for various parameters of interest using this approach. None of the designs are optimized for one specific parameter or task. As a proof of concept, this nanotweezer arm was designed to achieve both an out of plane spring constant in the range of contact mode AFM probes and also resonance frequency in the range of tapping mode AFM probes. The latter two are not complementary requirements. Therefore, the design is not optimized it for either case. However, given the number of parameters that can be adjusted, there is enough degree of freedom to optimize the design for various applications while still maintaining the same overall size, constrained compliance, and required actuation voltage. Future generations can be optimized to be more compliant in the out of plane direction for contact mode operation, or stiffer with higher resonance frequencies for tapping mode operation. More than anything else, this nanotweezer is an investigative tool to shown that various desired characteristics of nanotweezers are feasible using this design and fabrication approach.

Chapter 3 Fabrication

One of the requirements for the nanotweezers was that they be completely batch fabricated using standard microfabrication methods. The processes for fabricating the nanotweezers structures, consisting of the flexure mechanism and combdrive actuators were developed for use with an SOI wafer. The processes were developed for MIT's Microsystems Technology Laboratory clean room and adhere to its contamination protocols but do not use any equipment that is unique to this facility. The need for 1 μm lithography resolution requires the use of a Nikon stepper tool since it is the only tool capable of this resolution at this facility. The process, however, is compatible with non-stepper type lithography tools should one be available with the desired resolution.

3.1 Pattern Combination/Multiplication Lithography

In this project a Nikon NSR stepper lithography tool was used because of its ability to achieve 1μm resolution and alignment. Instead of using one large mask to expose the entire wafer, a stepper exposes a very small area of the wafer called a die. It then translates the wafer and exposes multiple such dies across the wafer surfaces. Each die is one instance of a device pattern or chip on the wafer. Steppers can also align to previous dies for subsequent layer patterning. With all their virtues, steppers, are expensive tools to work with. Masks for the Nikon stepper have to be 6in. quartz glass and are very expensive. Electronic devices, which interact in a network of other electronic devices and

are often patterned in dense multimillion arrays, are a good application for high resolution lithography tools as they effectively utilize the afforded resolution. MEMS devices however, are often stand alone and interact directly to the outside macro world. Often, as with the nanotweezers, MEMS applications consist of very small feature size devices connected to very large contact pads. This mismatched combination of very small (1μm) and very large (1mm) patterns both requires and also wastes a lot of expensive high resolution reticle space. For the proposed nanotweezers, large contact pads are used for ease of access on the bench and only four nanotweezers and respective contact pad patterns can be placed on a 6in. x 6in. reticle for the Nikon stepper.

Fortunately, in the case of the nanotweezers, the contact pads pattern repeats identically for all of the tweezer designs. It is therefore possible to have only one instance of the large pad patterns and to repeatedly expose and combine it for the various tweezers designs. There are two properties unique to steppers, which make them particularly suited for such a task. First, steppers can shutter down to any given area on a mask and expose only that area while blocking the rest of the reticle. This is shown in the Figure 3-1.

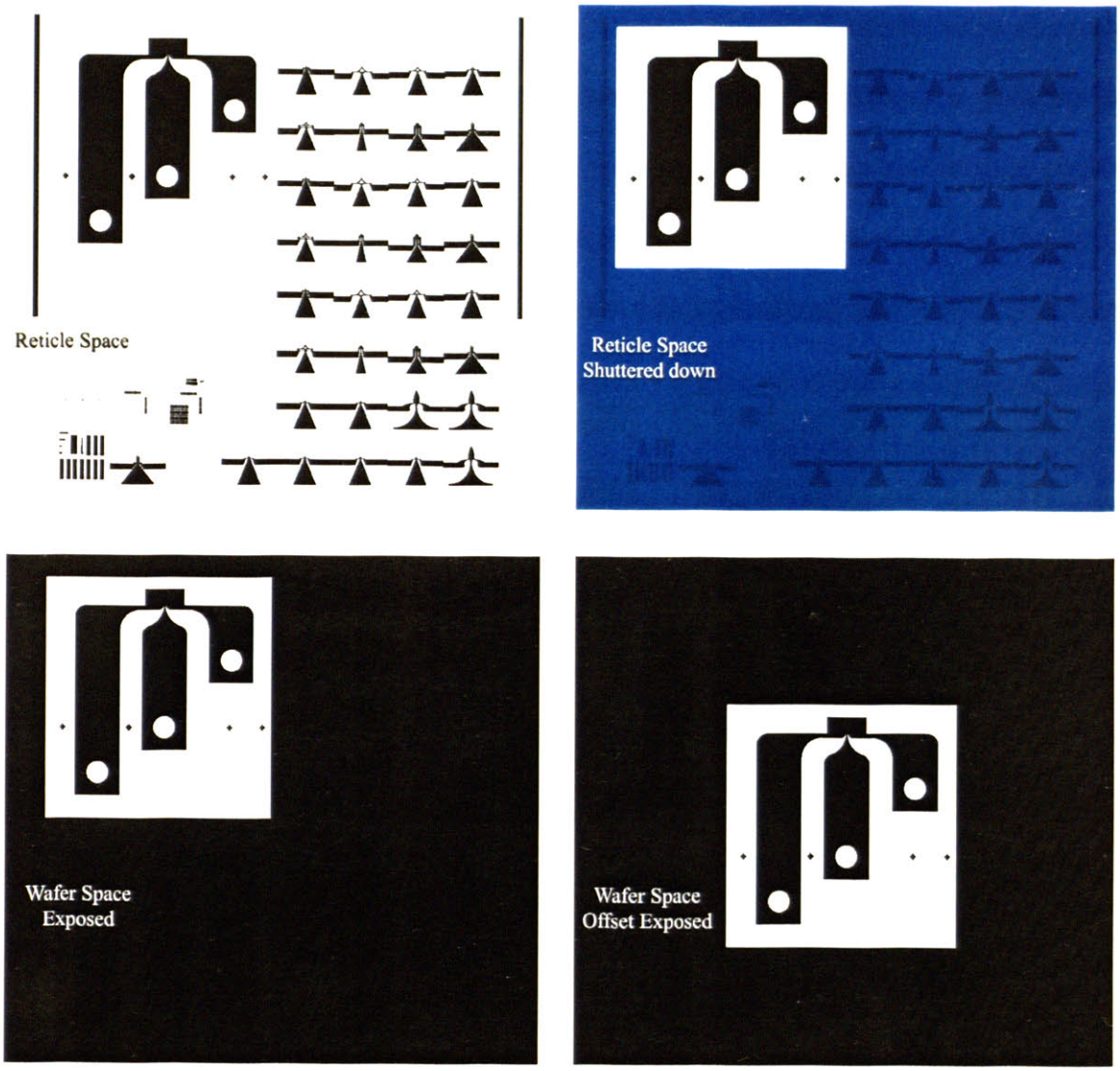

Figure 3-1. *Diagram showing the effect of shuttering and offset with a stepper lithography tool on the wafer pattern. The top two diagrams show the area of the reticle that is shuttered down. The lower left diagram shows the resulting exposed pattern on the wafer. The lower right diagram shows the same pattern offset to the center of the die. Offset is achieved by moving the wafer underneath the reticle.*

Steppers can also offset that area with respect to the wafer. For example, the previous pattern can be printed on the top left corner of a die, or it can be offset to the center position with respect to the die. The reticle always remains stationary. The wafer is moved underneath the reticle to achieve offset. In order to achieve good alignment to previous layers on the wafer, wafer stages must achieve accurate position control within

their alignment accuracy. Since the same stage is used to achieve offset, offset can also be done with the same alignment accuracy. Using these capabilities, it is possible to shutter down and expose two disjoint areas of the reticle in two separate exposure events using offset to make them overlap on the wafer. As shown in Figure 3-2, a single set of contact pad pattern can be shuttered off centered and exposed, and then any of a number of smaller tweezers patterns can be shuttered off, offset, and exposed so that they are connected to each other on the wafer.

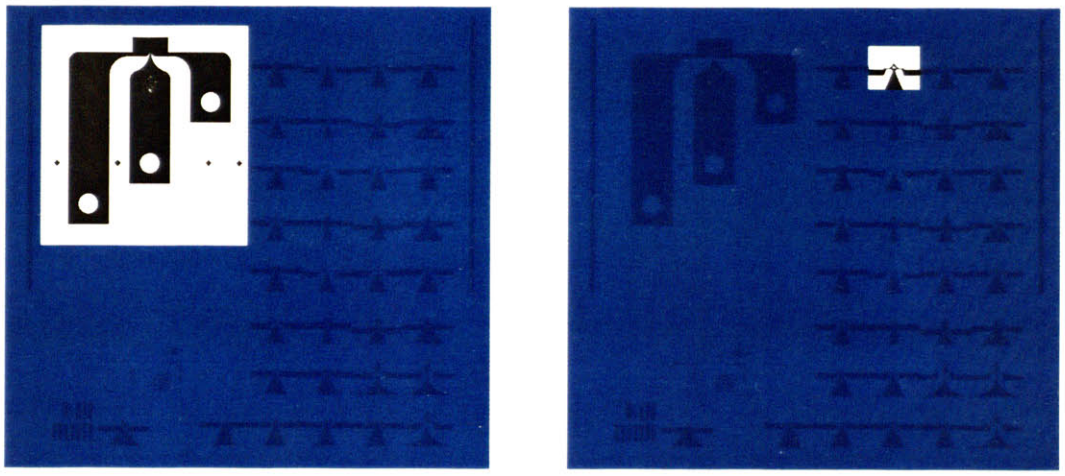

Figure 3-2. *Diagram showing the shuttering of two regions of the reticle to be combined for exposure on the wafer. The two patterns, which are disjoint on the reticle, will be offset during exposure to form a connected pattern on the wafer space.*

In this case each of the large contact pads converges down to a contact line to contact the nanotweezers. Given the alignment accuracy of the offset, it is possible to have each of the three contact lines, align and touch its respective contact point on the nanotweezer pattern. As was previously mentioned, this pattern combination is achieved in two separate exposure events prior to developing the photoresist. The caveat is that any area of the wafer that sees light from either pattern is exposed and will develop away.

Therefore in the connection region of the two patterns, the resulting pattern will not look like either of the two component patterns but is instead a combination of the two. Figure 3-3 shows an abstract example of this concept, where two disks are to be superimposed to form a bean shaped pattern. If just the two disks are used, the pattern will not look like the desired bean shape pattern. Instead, it will look like the pattern shown in Figure 3-3 b.

a) Patterns from two separate exposure events do not sum.

b) The two exposed patterns multiply (dark-field=1 light-field=0). dark-field×light-field=light-field

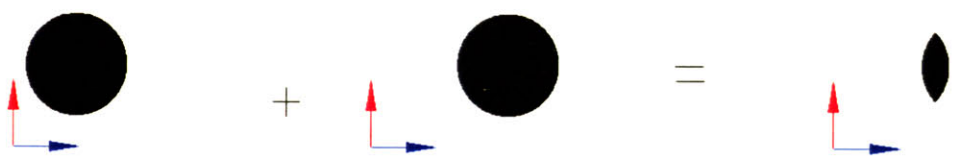

c) Shielding squares are necessary to achieve double circle pattern

Figure 3-3. *Diagram showing pattern combination of two disk patterns, a) shows the commonly expected resulting pattern that is incorrect, b)shows the actual pattern resulting from the combination of the two disks, c)shows what patterns need to be combined to form the desired pattern of a).*

Any area that sees light in either of the exposure events will dissolve away during development. Only areas that are blocked from the light by both patterns remain. **The patterns don't sum; they multiply.** To get the desired bean pattern, each disk pattern must also include an opaque square to block out the light from exposing the area that is to be patterned by the other disk. These opaque squares will be referred to as shield areas as they shield and prevent exposure of the unexposed area that is to be exposed by the latter pattern. In this case the shield areas are squares. In general the shield area has to be as large as the latter pattern that is shielding for. The shutters on the stepper are also in effect shield areas. In similar fashion, the pads shown in Figure 3-1 and Figure 3-2, also have a large shielding area at the top where they converge. This prevents the exposure of the photoresist in that region so that the tweezers pattern can expose it instead. A magnified view of this converging region is shown in Figure 3-4 with the opaque areas in black cross hatch. Similarly, the tweezer patterns also have large shielding areas so that they do not expose out the pattern that has been defined by the previous pattern pad exposure. These shielding areas, shown in red cross-hatch, reach out the edges of the steppers' shutters that shield out the rest of the beam column. When the two patterns combine, only areas that are shielded from the light by both patterns, shown in combined black and red cross-hatch, will remain. The final resulting pattern in the overlap/convergence looks like the pattern outlined in the lower right corner of Figure 3-4, where three distinct contact lines connected to the pads seamlessly converges to their contact points on the nanotweezer.

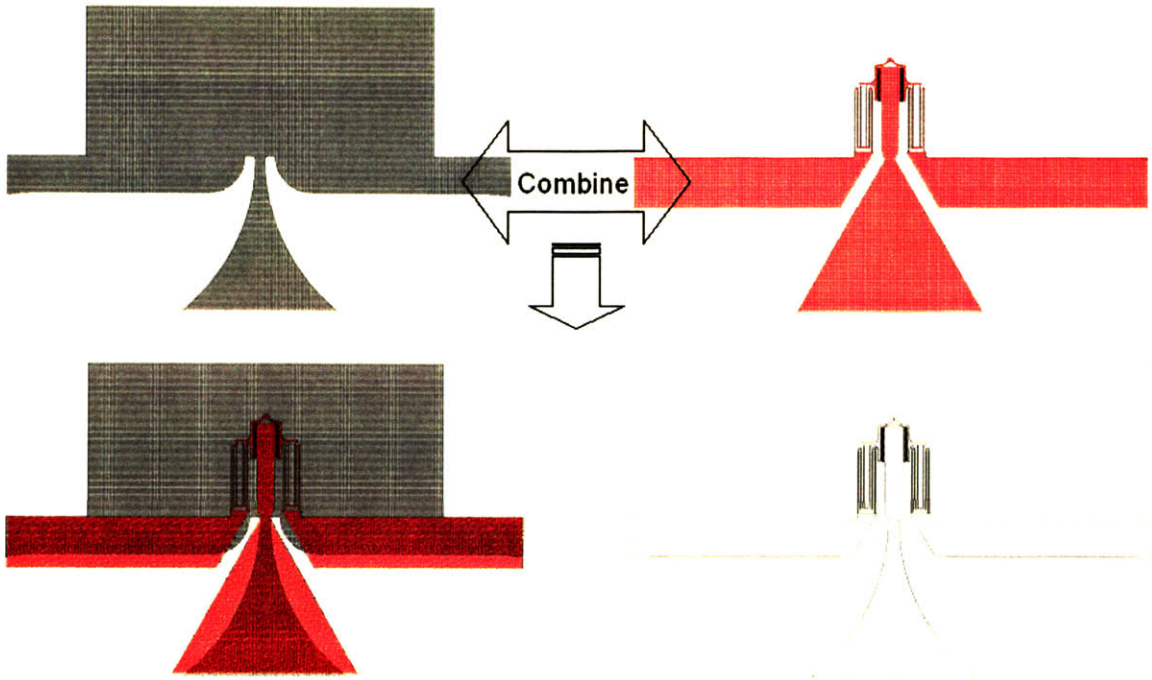

Figure 3-4. *Diagram showing how the pattern in the converging zone of the contact pads (shown in black cross-hatch) combines with the nanotweezer pattern (shown in red cross-hatch).*

If there is any position misalignment in the offset and the two patterns overlap too much, unpredicted geometry can result. Referring back to the two disk example, a spike phenomenon will result from a misalignment of the two patterns where the shield squares overlap. This is shown in Figure 3-5. In addition the circle patterns are compromised on either side. The size of the spikes can be as big as the side length of the shielding areas. In practice these shield areas are very large as they need to shield for large syndicate patterns. In the case of the contact pads, such spikes can be so large that they can connect and short all the contact lines together. Depending on the requirements of the pattern combination, different design rules can be followed to account for alignment errors between the two patterns. A bridge segment can be implemented to prevent spikes and still achieve electrical connectivity between the disks as shown in Figure 3-5 b).

a) Spike features caused by horizontal misalignment of the patterns

b) Use of bridge segment between patterns and shield squares to avoid spikes

c) Effect of horizontal misalignment on bridge segment

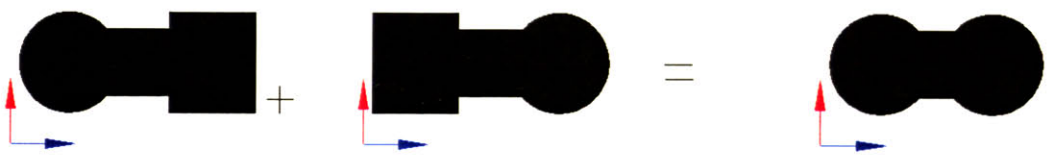

d) Effect of vertical misalignment on bridge segment

Bridge width is compromised

Figure 3-5. *Diagram showing potential pattern errors that can be caused by misalignments and ways to avoid them. a)shows the spikes caused by horizontal misalignment, b) shows how to avoid the spikes by use of a bridge segment, c) shows effect of horizontal misalignment on the bridge segment, and d) shows effect of vertical misalignment on the bridge segment.*

If there is any horizontal misalignment the bridge section will simply become shortened. If there is any vertical misalignment however, the bridge section becomes narrower. This may be an issue if the value for the resistance of the bridge is critical. If bridge width is of importance, one of the bridges can be made wider to encompass the other bridge as shown in Figure 3-6. Vertical offset errors will simply shift the narrower bridge inside the wider one. As long as the wider bridge is wider than the narrower one by twice the amount of expected offset error, the width of the narrower bridge will always be preserved.

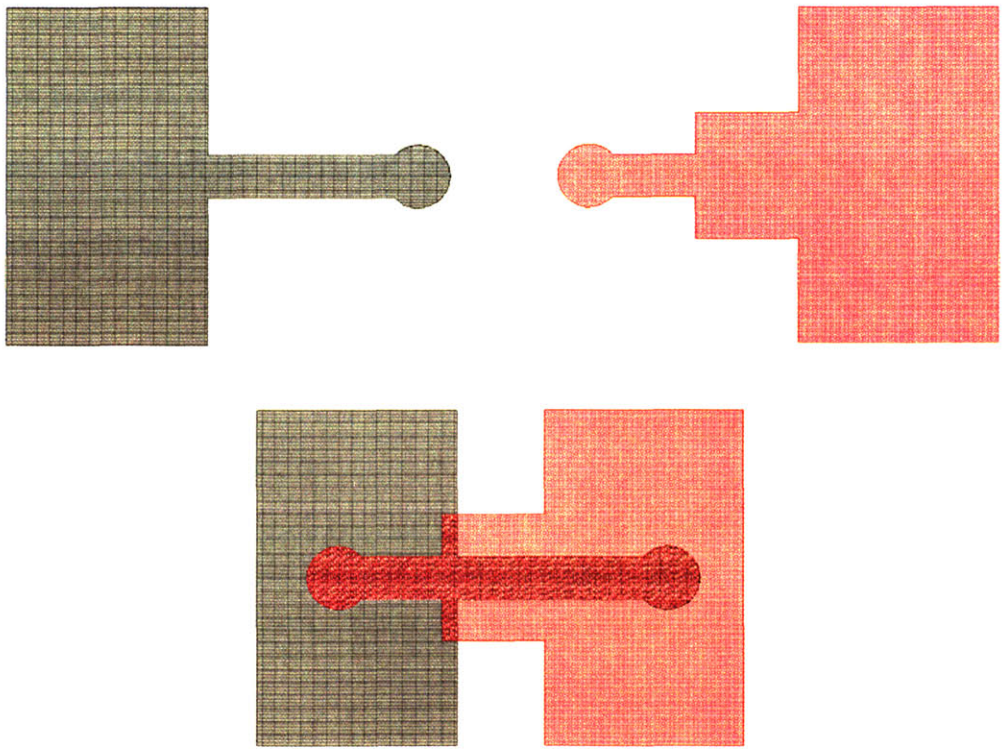

Figure 3-6. *Diagram showing how encompassing bridge segments can be used to avoid narrowing of bridge segments due to misalignment of the patterns.*

This technique also produces spikes as in Figure 3-5, however, the upper limit for the size of the spikes is limited to the width of the wider bridge and not the side length of

the shield squares. The location of the spikes can also be controlled to be in the middle of the bridge and away from any electrical or mechanical components.

Another issue that needs to be considered is the presence of sharp convex corners, which can cause high electric field concentrations; and sharp concave corners, which can cause high stress concentrations. If bridge thickness is not critical then tangential circular bridge sections are best used as they prevent sharp convex or concave corners due to misalignment. Please see Figure 3-7. Using this approach, sharp convex or concave corners do not form either horizontal or vertical misalignments.

A combination of the two approaches can be used to preserve both minimum bridge thickness and also prevent sharp corners. As shown in Figure 3-8, this approach also uses tangential circles to prevent cracks and spikes. However, the point of tangency is placed away from the minimum width location of the bridge thus preserving the minimum width of the bridge.

Use of tangential circular bridge segments to avoid sharp concave and convex corners

Effect of horizontal misalignment on bridge segments

Effect of vertical misalignment on bridge segments

Figure 3-7. *Diagram demonstrating the use of tangential circular bridge segments to prevent sharp concave and convex corners caused by misalignment of the patterns, a) perfectly aligned, b) horizontally misaligned, c) vertically misaligned*

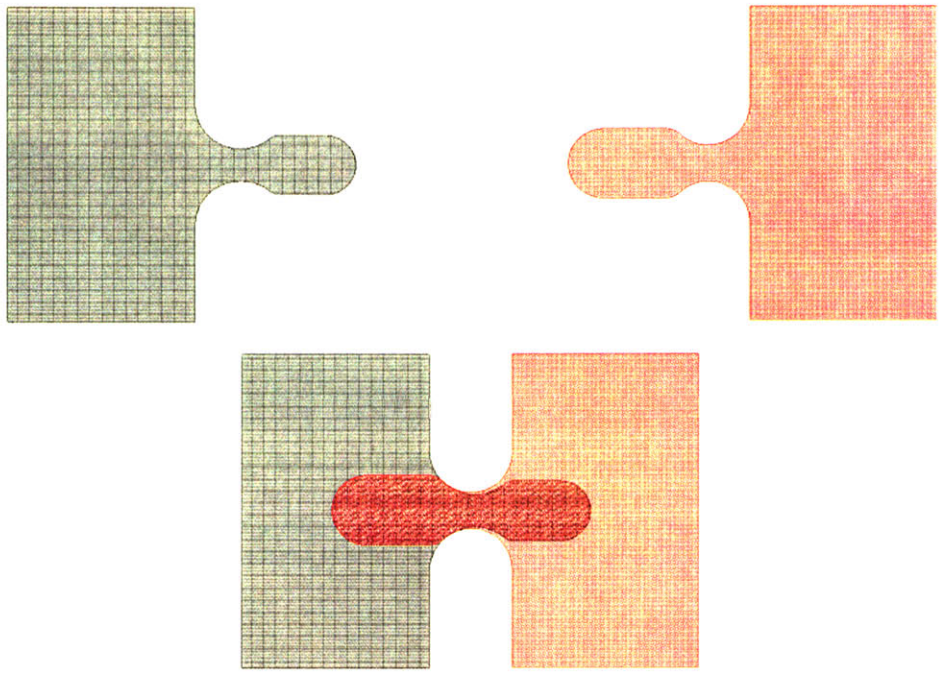

Figure 3-8. *Diagram showing the use tangential encompassing circular bridge segments. This combined approach both preserves minimum bridge width and avoids sharp concave and convex corners despite misalignment of the patterns*

The length of the bridge sections, size of the tangential circles, and overshoot of the wider bridge depend on the upper bound of the expected alignment error between the two exposures. This error is generally small for stepper tools. As previously mentioned, wafer stage motion, which is responsible for offset, is very accurate. Offset alignment errors are often less than 5μm. Pattern combination/multiplication was effectively used for the patterning of all nanotweezer design using the same contact pad pattern. Figure 3-9 shows the resulting structure for one of the nanotweezer designs. Notice the seamless union of the two patterns into one nearly indistinguishable combined pattern.

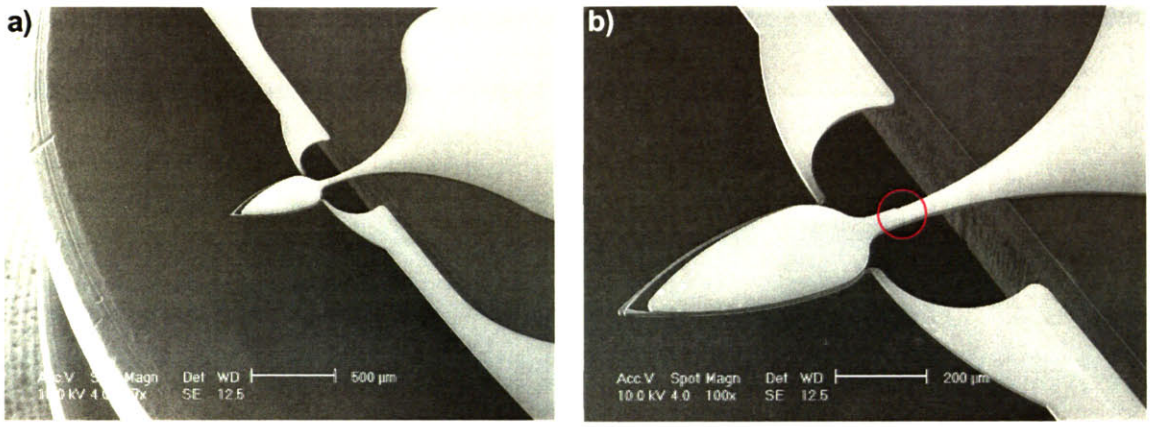

Figure 3-9. *SEM photos showing the result of pattern combination/multiplication lithography in practice, a) shows how the pattern from the large contact pads seamlessly converges down to the contact lines leading to the nanotweezer, b) is a magnified view of the intersection region showing a small step caused by the misalignment of the two patterns circled in red.*

3.2 DRIE Process

Once the photoresist has been patterned, the pattern is etched into the wafer to create the contact pad and device structures. For this step deep reactive ion etching (DRIE), a process for etching high aspect ratio features in Si, is used. DRIE is an anisotropic dry etch that uses inductively coupled plasma reactive ion etching. The process, which was developed by Bosch corporation[17], uses alternating etch and passivation steps to increase the directionality of the etch. A 20:1 aspect ratio etch is easily attainable. However, the process leaves rough sidewall with scalloping resulting from the alternating steps. In order to successfully produce 2 μm features, the passivation and etch times for the process were dramatically reduced to reduce sidewall roughness. Using this method smooth sidewall with less than 300nm roughness was achieved. Actual side wall roughness varies with the size of the channel cut and is often less than 100nm.

Figure 3-10 shows an example of nanotweezer arms etched using this process. The side walls appear smooth relative to the scale of the structure.

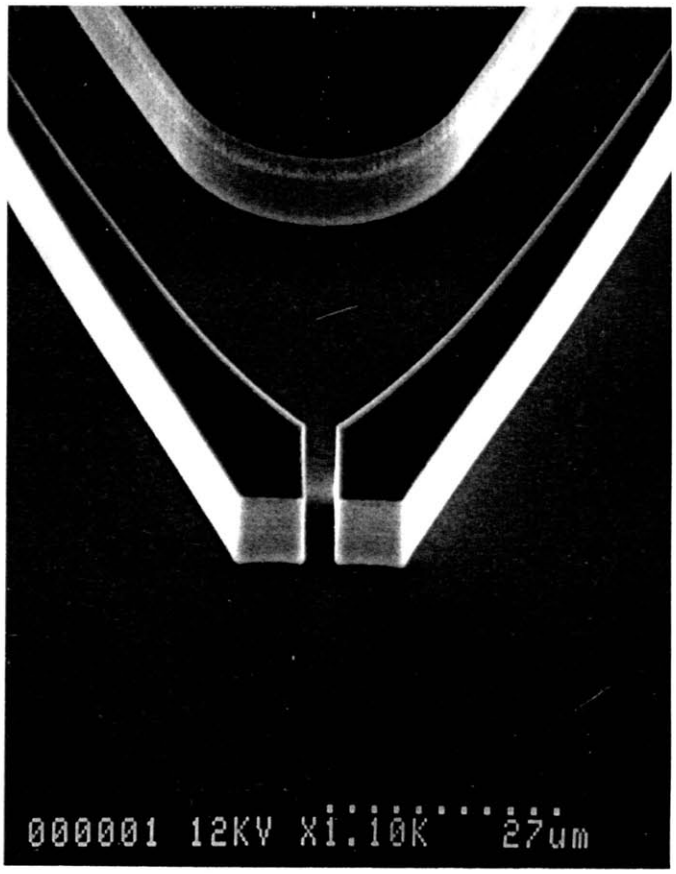

Figure 3-10. *SEM photo of structure formed by the FARDAD DRIE process showing the smooth side walls created by the process.*

Other parameters were adjusted to maintain good selectivity to photoresist and straight sidewall profile. The etch rate for this modified process is 1μm/min, which is slightly slower than other DRIE recipes. Table 3-1 summarizes the parameters used. This recipe was developed for a Surface Technology Systems machine. In MTL it is has the name "FARDAD" and is available on the machine "STS2".

Parameter	Value			
Etch step time	7 seconds			
Passivation step time	5.5 seconds			
Etch overrun	0.5 seconds			
Pass over	0 seconds			
Pressure APC settings	75% Manual			
Base Pressure	0 mTorr			
Pressure Trip	94 mTorr			
Gas	**Etch**		**Pass.**	
	Flow (sccm)	Toler.	Flow(sccm)	Toler.
SF_6	105	25	0	5
C_4F_8	0	5	25	0
O_2	0	5	0	5
Ar	0	5	0	5
RF Power	**Etch**	**Pass.**	**Toler.**	
Platen	120 W	60 W	99	
Coil	800 W	600 W	99	

Table 3-1. *Table of parameters for "FARDAD" DRIE etch recipe.*

3.3 Surface Tension

Once the DRIE etch is complete and the photoresist is removed the final device structure is exposed. However, the devices cannot function since they are still attached to the substrate via the underlying buried oxide layer (also referred to as BOX layer). Please refer to Figure 2-1. Hydrofluoric acid can be used to remove the BOX layer undercutting the device and thus releasing them. However, when this is done, the surface tension force of the solid, liquid, air interface is rather large compared to the stiffness of the device. As the liquid dries and the various droplets shrink over the devices, the surface tension force is large enough to deform the slender beam structures causing them to permanently stick to each other as shown in Figure 3-11. The exact value of the loading to due surface tension depends on the contact angle of the liquid air surface with the structures. The value for contact angle depends on many factors such as temperature, humidity, and any polymer coating left on the structures by the DRIE process. Using surface tension coefficient of 72.8 mN/m for water, the surface tension force distributed on each beam is

estimated to be on the order of 5×10^{-5} N. This is based on semi-infinite droplet assumption given the approximately 20:1 aspect ratio of the long beams. The force of the actuator, which the flexure mechanism was designed for, is two orders of magnitude less than the surface tension force on any one beam. As is expected, the structures become permanently deformed as shown in Figure 3-11. Problems caused by surface tension are common for MEMS devices and organisms at this scale[18]. The surface tension force scales linearly with length scale whereas stiffness and inertial forces scale with the square and cube of length scale respectively. As such at very small scales the surface tension force dominates.

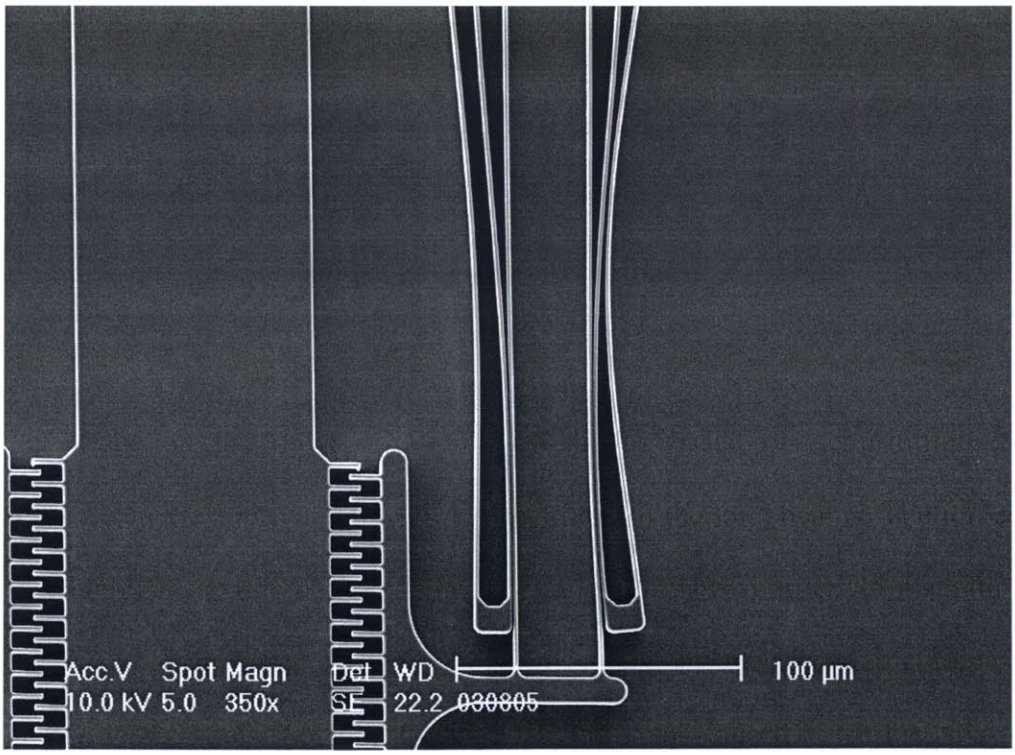

Figure 3-11. *Close-up SEM photo of structures showing effect of surface tension on the structures. The slender beams have permanently adhered to each other and the device is destroyed.*

3.4 Solution to Circumvent Wet Release

To alleviate the problem associated with surface tension, a dry process for releasing the devices is necessary. A common solution to this problem is to use critical drying processes. Another alternative for dry release is to use a hand off scheme, where the device is held onto by a secondary deposited material prior to wet release of the BOX layer. The deposited material braces the device structure to prevent it from deforming due to surface tension. This secondary material has to then be removable via a dry process in order to not re-encounter the surface tension issue. In such a scheme, before the BOX layer is removed via a wet process, another material can be deposited to braces and protect the structures from the top. A suitable material that can be readily removed via a dry process is photoresist. Photoresist can be removed using oxygen plasma and hence can used to brace the device during the BOX layer removal. Once the structures have been coated with a thick layer of photoresist on the top there are two ways to achieve fluid access to remove the BOX layer. The first is to pattern and develop the thick bracing photoresist to create access holes/ports for the HF to get through the photoresist, remove the BOX layer, and undercut the devices. Another method is to create port holes in the substrate layer of the SOI to allow HF to access and remove the BOX layer through the backside of the wafer while the photoresist braces and protects devices from the front side. The latter option is used in this case since removal of the substrate layer from underneath the device is already necessary to achieve overhanging structures.

3.5 Struct-v3 Process

The Struct-v3 process flow is based on the use of photoresist as a brace material to protect against surface tension during wet processing. The photoresist also protects the devices during the bulk etch of the substrate from the back that cuts out the individual dies. This process is based on the DRIE process that is detailed in 3.2. The process results in overhanging structures necessary for use with an AFM.

As mentioned before for this process a SOI wafer is used. The process is compatible with varying device and substrate thicknesses. However, a minimum thickness of 2 μm is required for the BOX layer due to the selectivity of the etch processes used. For this process the crystal orientation of the device layer is not critical. However, for the process that creates the tips, described in Chapter 5, crystal orientation does matter. Figure 3-12 shows a 2-D process flow diagram for the entire process.

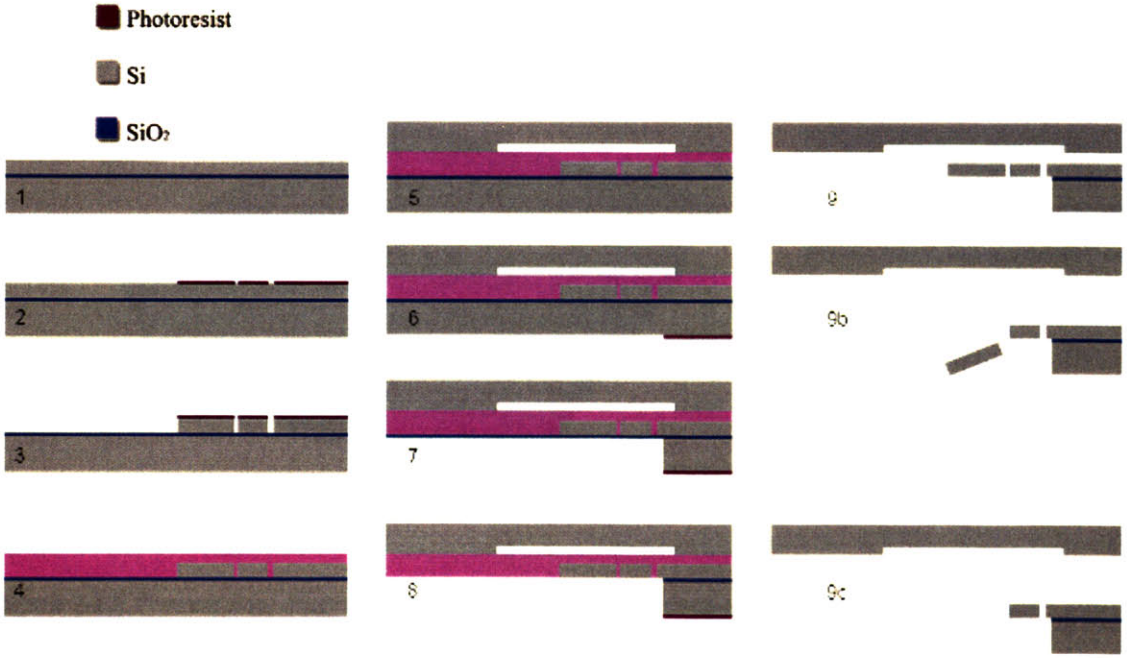

Figure 3-12. *2-D Diagram of the entire process flow. The left column (steps 1-4) shows the patterning and bracing of the device layer. The middle column (steps 5-8) shows the mounting of the SOI water and subsequent BOX layer removal and die separation. The right column (step 9) shows the final ashing step.*

The following is a step by step explanation of the process. For some steps, the intricacies of the process are best conveyed using a three dimensional representation. For some key steps a three dimensional diagram representing a 3 × 3 die section of the wafer is shown.

1. The wafer is quoted with 1 μm photoresist and the resist is patterned with a Nikon stepper to pattern many dies, each consisting of the nanotweezer structure and contact pads.
2. This pattern is next transferred onto the device layer via a DRIE etch that stops on the BOX layer (Figure 3-13). This DRIE etch is the modified version detailed in section 3.2.

Figure 3-13. *Process flow diagram for nanotweezers structures at the completion of step 2 (post DRIE). Insert on the right shows a perspective view of a representative 3 × 3 die section of the wafer.*

3. The photoresist is ashed using oxygen plasma and removed.

4. The wafer is then coated with another thick (10 μm) layer of photoresist that serves as a brace to protect the devices (Figure 3-14). Prior to the brace photoresist application the wafer is re-exposed to HMDS vapor to insure that the photoresist is attracted to the Si and fills all crevasses of the device structure. This photoresist is then soft-baked.

Figure 3-14. *Process flow diagram for nanotweezers structures at the completion of step 4 (post PR brace). Insert on the right shows a perspective view of a representative 3 × 3 die section of the wafer.*

5. Using a second thin layer of thin photoresist the SOI wafer is mounted to another wafer, referred to as the mount wafer.

The mount wafer has special pillars surface micromachined at its interface with the SOI wafer. These pillars are 30 μm tall and are prefabricated in the mount wafer prior to the mounting. The Figure 3-15 b) shows the bulk of the mount wafer as transparent to demonstrate the location of the pillars relative to underlying SOI wafer.

a)

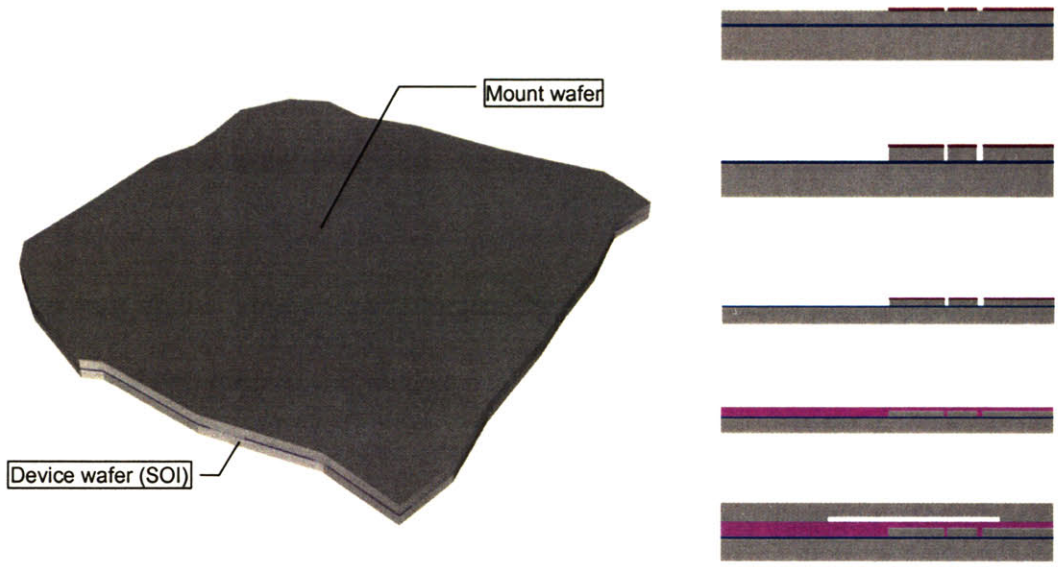

b)

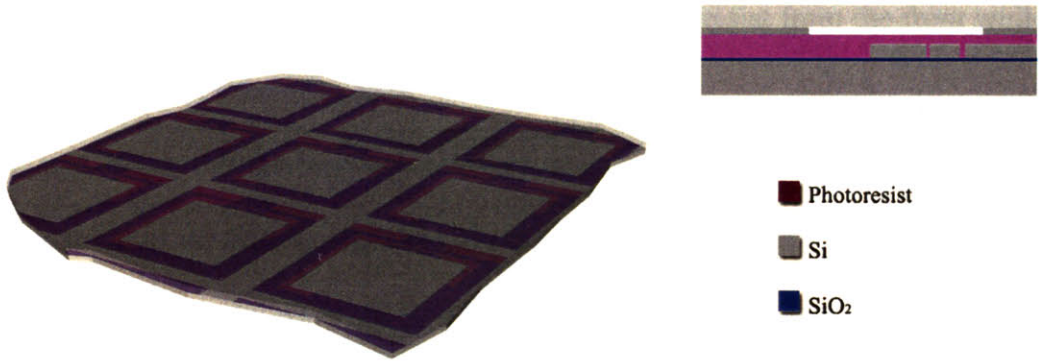

Figure 3-15. *Process flow diagram showing the device wafer mounted to a mount wafer a). The mount wafer has special pillars and channels surface micromachined into its interface surface with the device wafer. The locations of these pillars and channels relative to the device wafers are shown in a see through diagram b).*

Note, the pillars contact the SOI wafer within the contact pad regions only. No part of the mount wafer actually touches the SOI wafer in the nanotweezer regions. In

effect the nanotweezers, encased in photoresist, hover in channels in the mount wafer. A soft bake is carried out at 90 °C for 120 minutes to secure the mount.

6. Once properly mounted from the front, the backside of the SOI wafer is patterned with thick photoresist.
7. A long DRIE etched is then used to bulk micromachine the handle of the SOI all the way up to the BOX from the backside. Since side wall roughness is not important, this is done using a regular DRIE etch with faster etching rates. This step serves two purposes. It cuts around and separates each of the individual dies from the device wafer. It also removes a large area of the substrate from the region underneath the nanotweezers thus producing the required overhanging structures.
8. Next the BOX layer is removed using a wet BOE or HF dip (Figure 3-16). The devices are encased and protected by the bracing photoresist from the front while the wet etch works from the back.

At this point the devices are released and the individual dies have been completely cut out of the SOI wafer. The only thing keeping the dies from falling out is their attachment to the mount wafer via the photoresist.

9. Next the two wafer combo is placed in an asher where oxygen plasma slowly eats at the organic photoresist. The exposed photoresist inside the etched channels wafer channels erodes away first as shown in Figure 3-17.

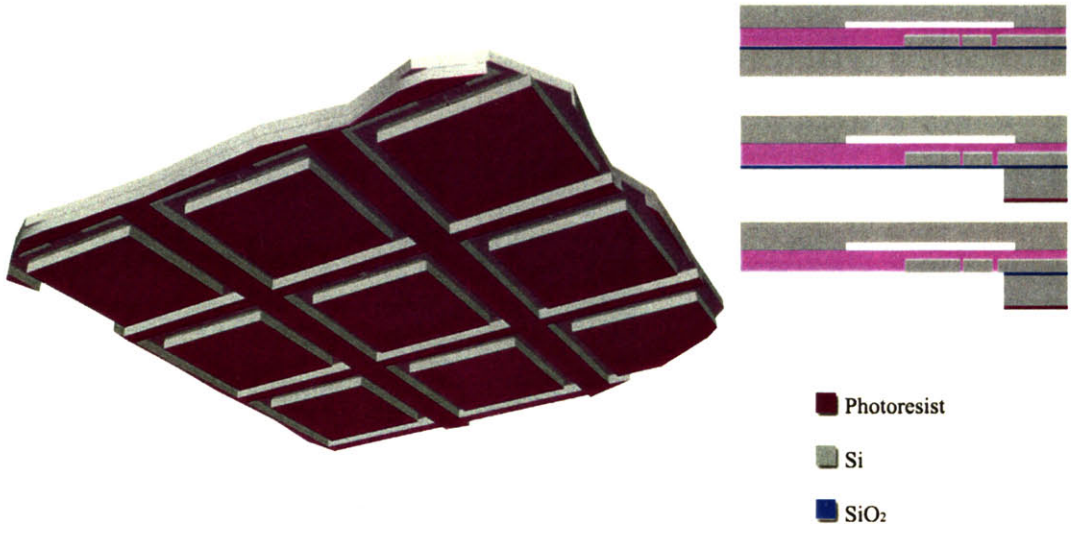

Figure 3-16. *Process flow diagram for nanotweezers structures after step 8 (post backside die release). Insert on the right shows a perspective view of a representative 3 × 3 die section of the wafer.*

As the wafer is ashed even further, the oxygen plasma starts to attack the photoresist sandwiched in the region between the contact pads and the mount wafer pillars. Once this step is complete the individual dies become dismounted from the mount wafer and can be extracted for use (Figure 3-17). This step is carried out with the two wafer combo upside down so that the mount wafer is on the bottom. This way after dismounting is compete, gravity keeps the dies in place on the mount wafer until they are picked off.

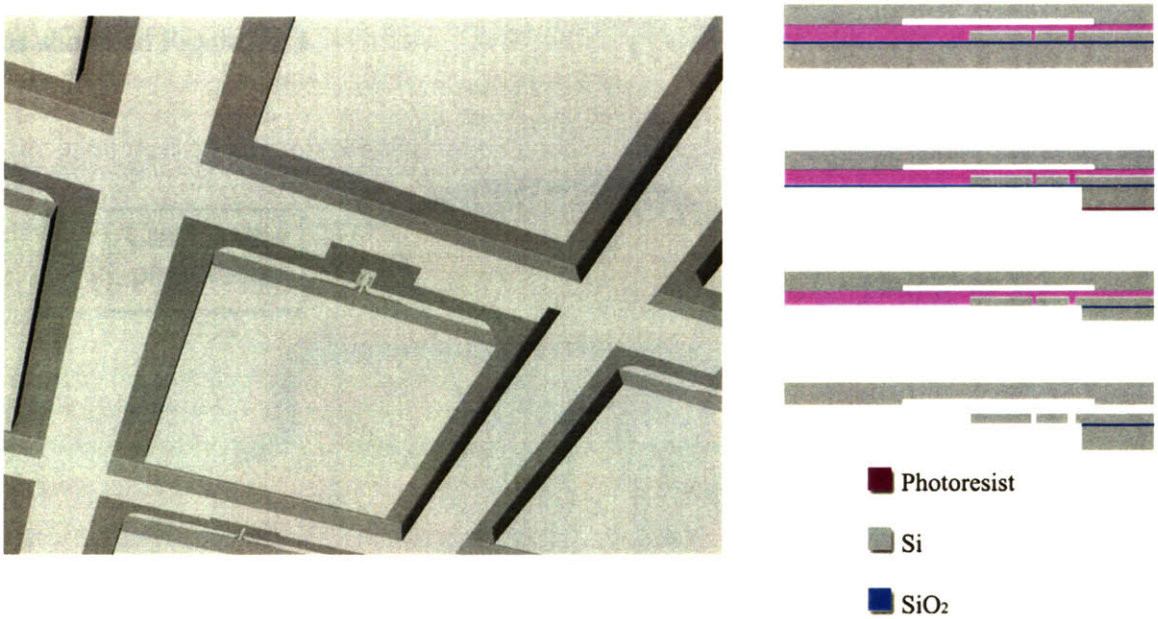

Figure 3-17. *Process flow diagram for nanotweezers structures at the completion of step 9 (post dry dismount). Insert on the right shows a perspective view of a representative3 × 3 die section of the wafer. At this point the individual dies are no longer stuck to the mount wafer and can be extracted for use.*

3.5.1 Bumpers

The photoresist that is spun on in step 4 has two purposes: to brace the structures to prevent deformation due to surface tension during the BOX layer removal; and to brace the structures to protect them during the back side DRIE etch. The wet process for removing the BOX layer is gentle enough that photoresist alone will suffice. However, the DRIE process used in step 7 is very hard on the photoresist. This is a 4-5 hour etch and because of the increase thermal resistance of the mount wafer, the device wafer heats up during this process. Even by separating the etch into smaller 1 hour cycles followed by cooling periods the combination of high temperature conditions and the momentum of the plasma cracks the photoresist towards the end of this step. When such cracks happen in the vicinity of a nanotweezer, the crack often propagates through the entire device shifting the cracked sections over. To prevent these cracks from damaging the devices the

photoresist brace is strengthened by the use of bumper structures around the nanotweezer as shown in Figure 3-18.

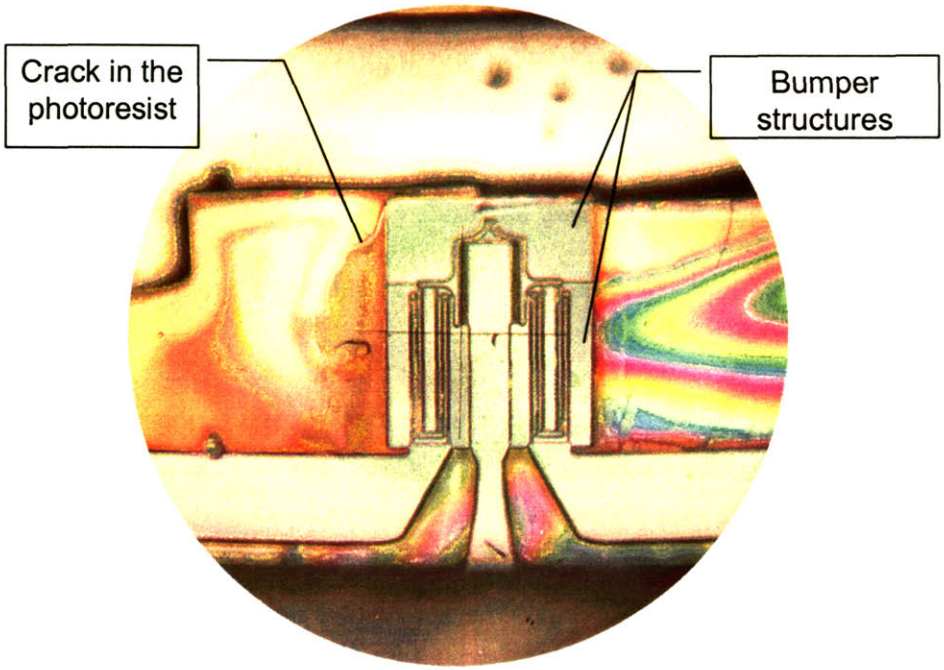

Figure 3-18. *Optical microscope photo of the wafer after the back side DRIE etch (step 7). The photo shows the nanotweezer section and the contact lines that are converging in. Bumper structure that surround the nanotweezer are surface micromachined in the device layer to prevent cracks from propagating through the device.*

These bumper structures only outline the nanotweezer and are not connect to them through the device layer. The bumpers are only attached to the nanotweezer via the BOX layer underneath and the bracing photoresist on top. When the BOX layer and the photoresist are removed in steps 8 and 9, the bumper structures simply fall away from the nanotweezers. Since the ashing process is done with the two wafer combo upside down, the bumpers structures fall into the channels of the mount wafer.

3.6 Outcome of Fabrication

With the addition of the bumper structures, a reasonable number of devices survive the entire process all the way through die separation and removal from the wafer. Overall yield for this design is 30-36%, which is low by industry standards and can be improved with incremental modifications to process parameters and use of more uniform SOI wafers. The SEM images in Figure 3-19 show the devices to be in good condition without any noticeable out of plane deformation due to residual stresses.

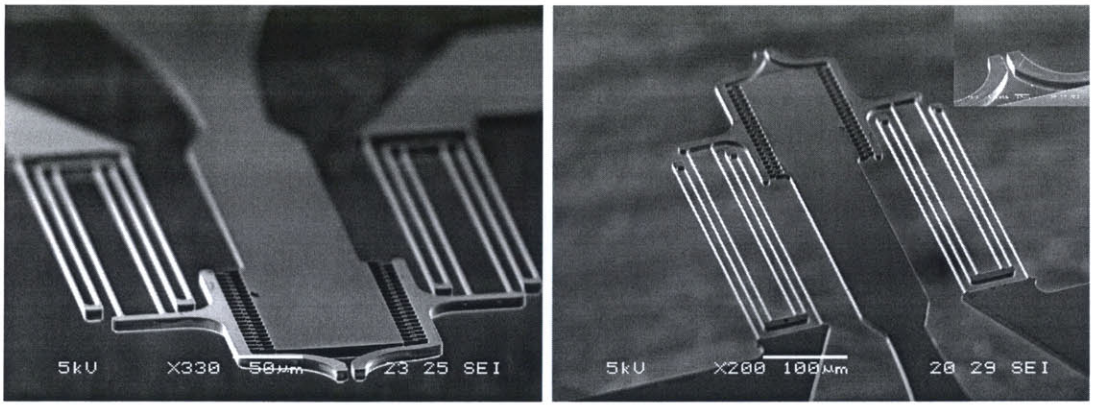

Figure 3-19. *SEM photos of the nanotweezers structures after extraction from the process. Insert on top corner of the picture on the right shows a magnified view of the tips region.*

As seen in Figure 3-20, in-plane geometry also looks as expected with good tapering for the anchor points of the beams. There is however, some unexpected geometrical variations in the cross-section of the beams caused by the DRIE etch. This will be discussed in further detail in section 4.2.

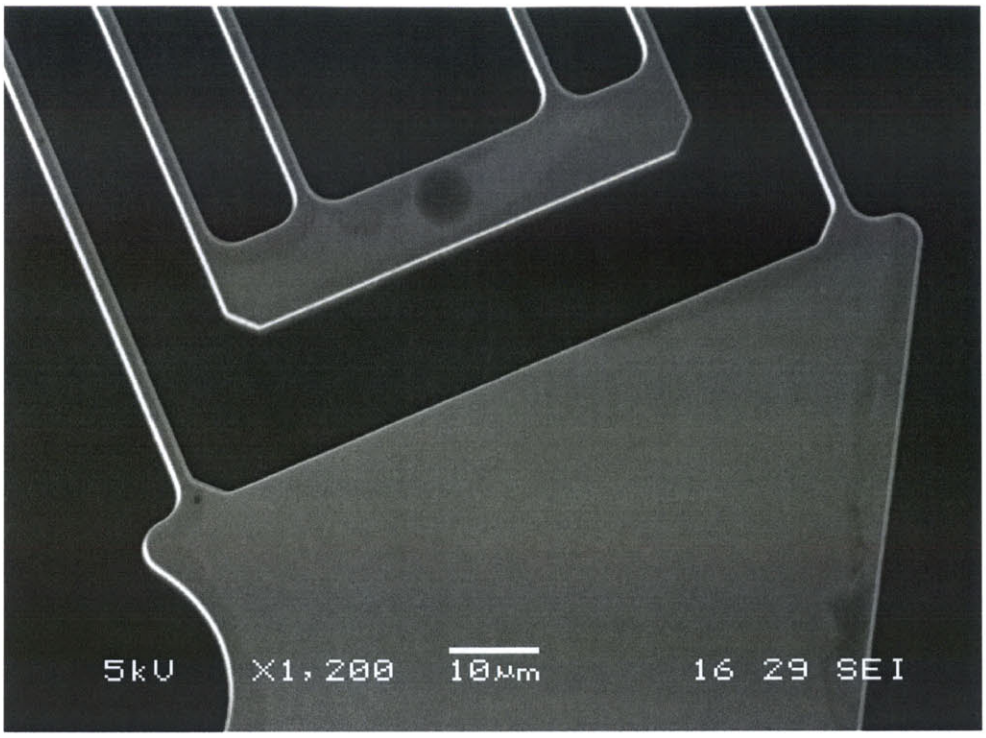

Figure 3-20. *Close-up top view SEM photo of the nanotweezer flexure mechanism showing beam anchor points.*

Chapter 4 Device Testing

Several nanotweezers were fabricated using the Struct-v3 process. These devices were tested to verify actuated response and compare it with designed values. The main priority was to verify alignment of the two arms and whether nanoscale actuation of the tweezing gap was possible. The in-plane frequency response of the devices was also tested to provide additional data that could be used deduce the cause of deviation between measured and predicted values.

4.1 Experimental Setup

Once on the bench top it was necessary to make good electrical contact to the doped Si contact pads of the nanotweezer. For this, the surfaces of the Si pads were scratched using a diamond scribe in order to scratch away any native oxide and create a rough surface. Next, 500 μm indium spheres were squished down and over the rough scratches. The scratches helped grab on to the malleable indium sphere as they were pressed down and sheared at the same time. Next, a conducting metal pin was pressed on top of the indium sphere squishing it down even more. Indium was used as an intermediate material to achieve better ohmic contact to the Si. The amount of contact resistance varies greatly, from 30 kΩ to just under 1 kΩ with increasing mechanical pressure on indium spheres. To increase the mechanical pressure and decrease the contact resistance, micromanipulator stages were used to keep the indium balls under pressure underneath the conductive pins while the setup was secured using epoxy. Figure 4-1

shows the setup prior to the application of epoxy. The device was monitored under a microscope and actuated several times to test contacts before the application of epoxy. Once the epoxy was fully cured the micromanipulator stages were detached and the nanotweezer was ready for testing.

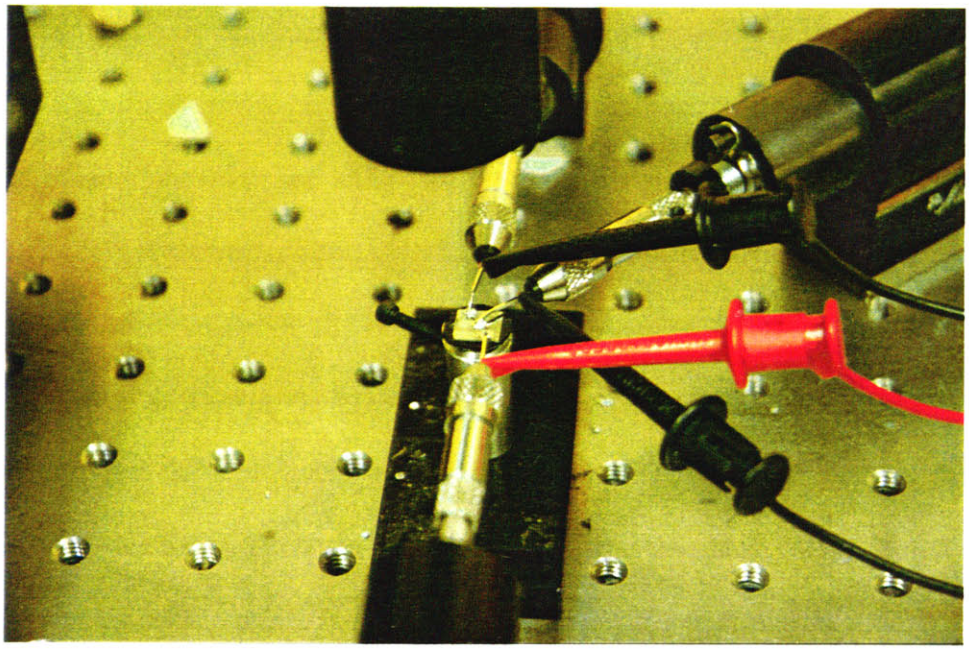

Figure 4-1. *Photograph of experimental setup*

On a separate sacrificial device made of the same wafer, two such contacts were made to the doped Si material at distance of 3 mm. The total resistance for the pin-indium contacts and the wafer resistance between them was measured to be between 600-800 Ω after the epoxy had fully cured. Therefore, the contact resistance of the pin-indium contacts to the Si pads can be safely considered to be less than 400 Ω. In comparison, the electrical resistance of the flexure mechanism is 45 kΩ based on the resistivity of the device layer. The contact resistance that is achieved using this method is small in comparison. In addition, since the capacitance of the combdrive is predicted to be

approximately 10fF, the time constant for the 45 kΩ-10fF resistor capacitor pair is only 4.7×10^{-10} seconds. The electrical response of the actuator is very fast and does need to be considered.

To characterize deflection vs. voltage behavior the devices were observed using an ESEM. This ESEM has a port for electrical connections for use with a paltrier thermometer. This port was modified to allow electrical connection to the nanotweezers across the vacuum chamber. The resistance of this connection was less than what can be measured by an ohmmeter. The ESEM also has a tool for measuring distances off of the display. The measurement tool already accounts for magnification. Figure 4-2 shows the device actuated fully closed in the ESEM. A close up of the tip region in both open and closed positions is shown in Figure 4-3. The measurements were made at higher magnification than the figures above. While the picture becomes less sharp at the higher magnification, relative position can be measured more accurately. With this setup it was possible to measure and control the gap of the nanotweezers to within 30 nm.

The resonance frequency of the device was measured using the MEMS Motion Analyzer G2 from Umech Technologies Corporation. This equipment is based on technology developed at MIT by Davis and Freeman[19]. It uses an optical microscope to take images of MEMS devices as they are excited by the equipments voltage source. Several images are taken in phase with the source excitation and are analyzed to correlate the amplitude of oscillation with the frequency of excitation.

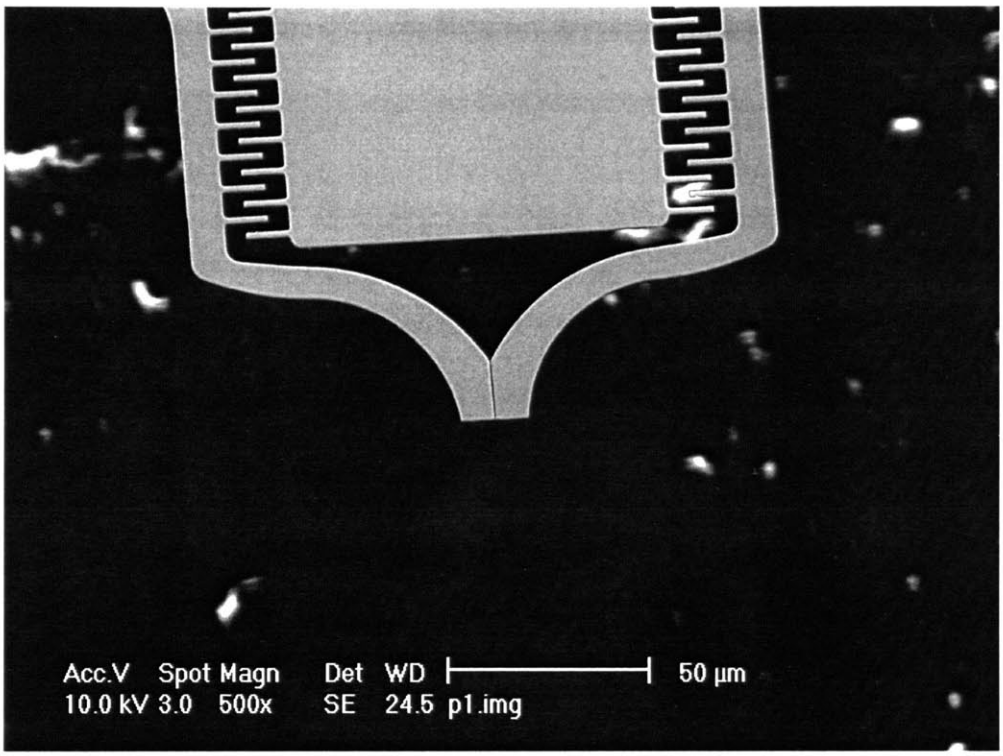

Figure 4-2. *SEM photo of the nanotweezers in the closed position*

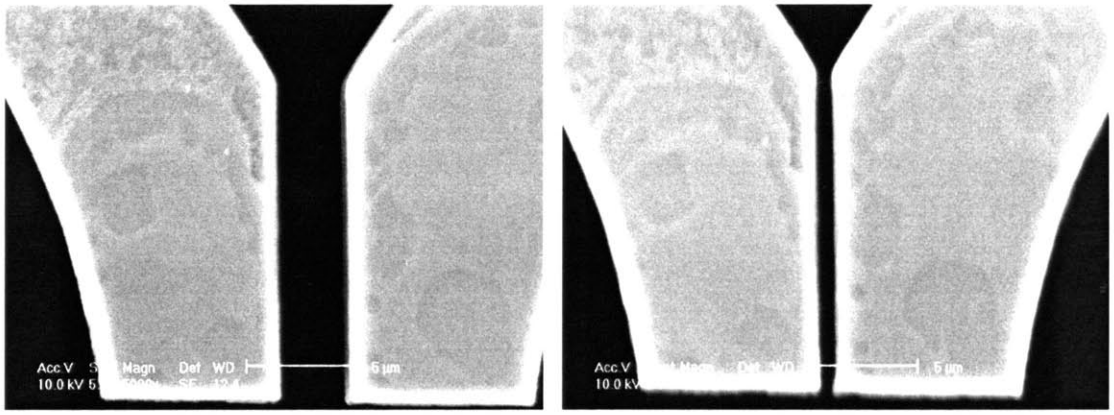

Figure 4-3. *Close-up SEM photo of the nanotweezers' tips in the open and closed positions*

While diffraction limits the resolution of an image taken from an optical microscope, it does not limit resolution in measuring the spatial shift of the image. Therefore, by using a high enough resolution CCD sensor it is possible to see measure the amplitude of oscillation of a feature to within nanometers. This method was used to

obtain the frequency response of the system for in-plane motion. The system is also able to measure out of plane modes though this data was not obtained for the nanotweezers.

4.2 Analysis and Explanation of Results

Figure 4-4 shows the nanotweezers gap as a function of voltage applied across the combdrive actuators. The same voltage is applied across both combdrives and the arms close symmetrically. The nanotweezers close completely at 12.92V. This result is off from the calculated intended value of 27.5V to fully close the gap by about 50%.

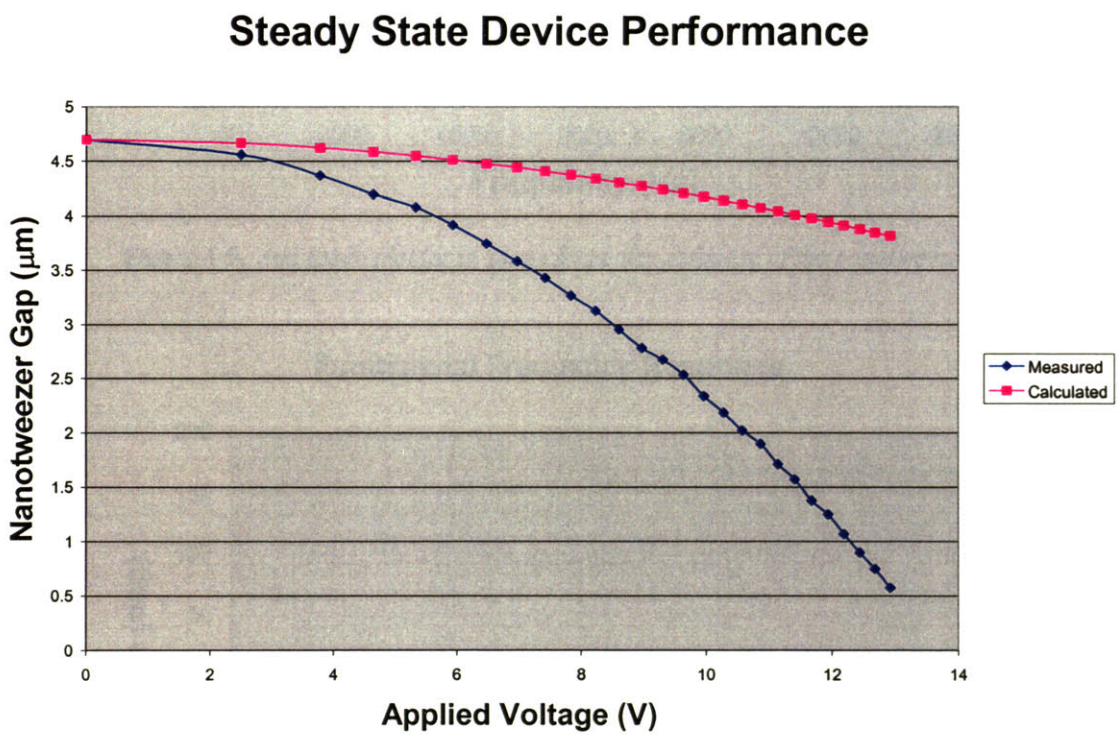

Figure 4-4. *Graph showing measured vs. calculated actuation data*

Figure 4-5 and Figure 4-6 show in-plane frequency response of the nanotweezers obtained using MEMS Motion Analyzer. This data corresponds to in-plane vibrations of the nanotweezer arms excited using its own combdrive actuator.

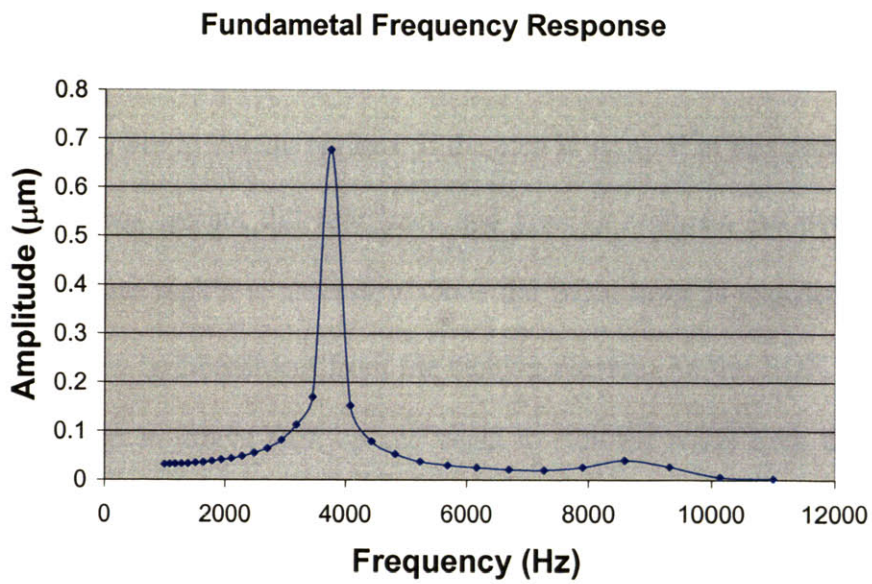

Figure 4-5. *Amplitude plot for in-plane frequency response of the nanotweezers*

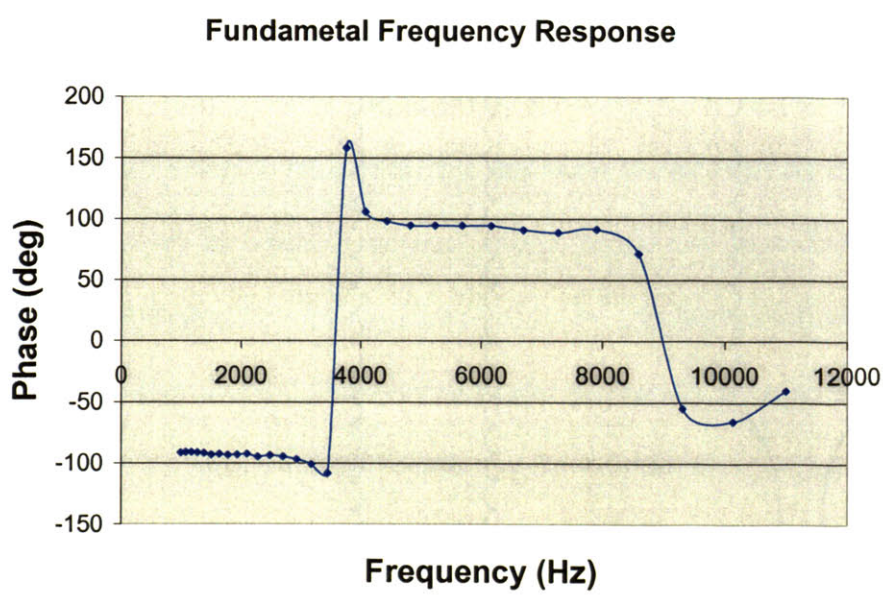

Figure 4-6. *Phase plot for in-plane frequency response of the nanotweezers*

The measured first fundamental frequency is 3.775 kHz. The calculated value based on FEA for the first fundamental frequency is 8.128 kHz which is off by 54%.

The differences between measured and calculated values are due to deviations of the structure geometry caused during the DRIE etch. When the device layer of the SOI wafer has non-uniform thickness, the devices in the thinner region are etched down to BOX layer before those in thicker regions. If the etch is stopped at this point, the devices in the thicker regions are not full fabricated and yield is reduced. An over etch of the devices in the thinner region is necessary. Once the BOX layer is exposed, it begins to charge up due to ion bombardment from the etching plasma. As the BOX layer charges up it causes the ions to reflect back up and begin to etch the walls from the bottom up. This effect is called footing. As a result a beam cross-section that should look like the one in the middle, in Figure 4-7, will end up looking like the one on the right.

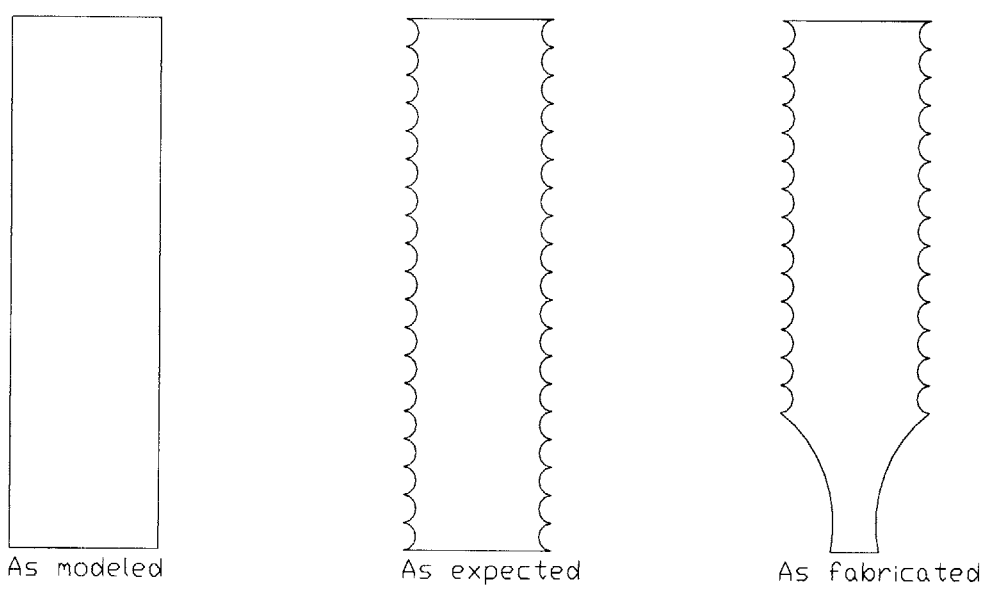

Figure 4-7. *Diagram showing the effect of the footing from the DRIE etch on the beam cross-section*

Figure 4-8 shows a close up SEM photo of the footing effect on the device. The BOX layer, which was subsequently removed, was underneath this structure.

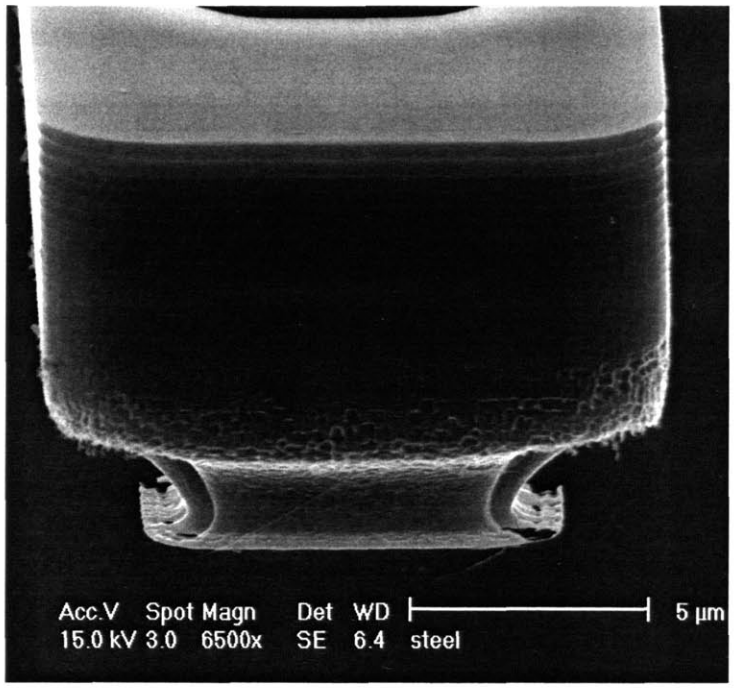

Figure 4-8. *SEM photo showing the effect of the footing from the DRIE etch on the structure. The effect is visible underneath the structure where the BOX layer was, prior to removal.*

To account for this deviation a new effective thickness for the beam, representing the average thickness, is used in the model. It is important to note that any over etching or footing that would cause the beams to become thinner would also cause the gap between the combdrive teeth to become wider. Therefore to be consistent, the effective beam thickness $h_{effective}$ and the effective combdrive gab $gap_{effective}$ must have equal and opposite deviations from their nominal designed values.

$$h_{designed} - h_{effective} = -\left(gap_{dsigned} - gap_{effective}\right) \tag{4-1}$$

.

The nominal value for the beam thickness h and the combdrive teeth gap is 2 μm for both. Using $h_{effective}=1.06\mu m$ and $gap_{effective}=2.94\mu m$ achieves a better match to predicted results for nanotweezer gap vs. drive voltage. The plot of the calculated behavior with the effective parameters is shown in Figure 4-9.

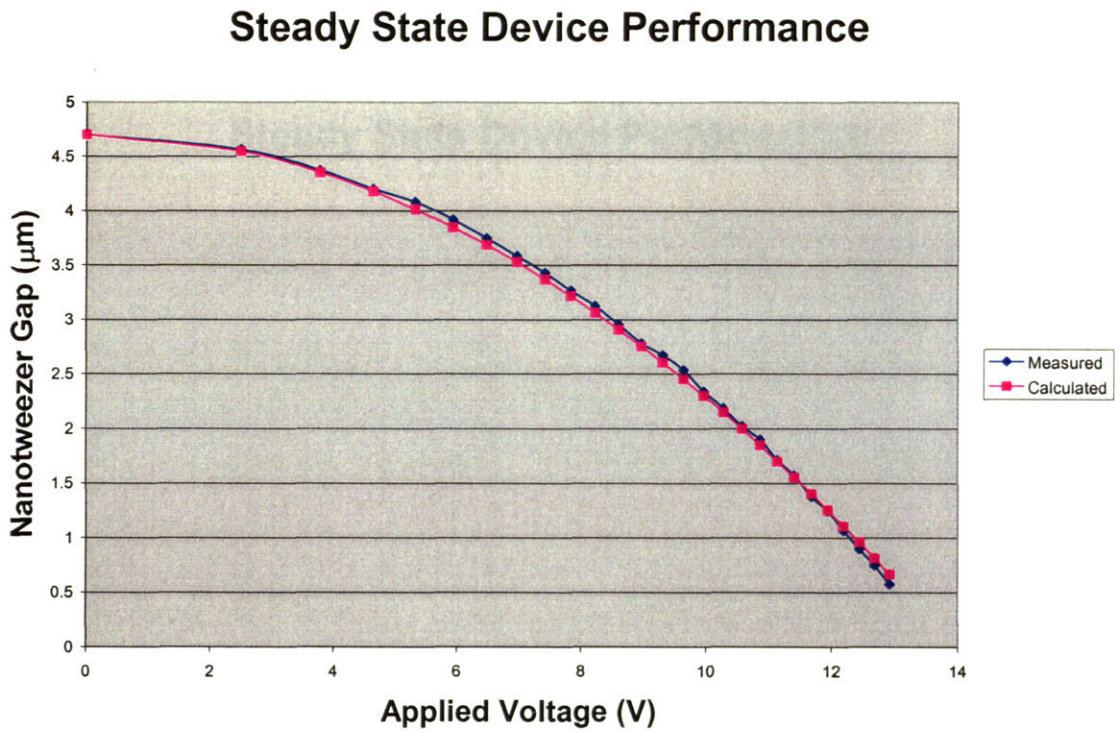

Figure 4-9. *Graph showing measured vs. calculated actuation data. The new calculated data accounts for structural deviations caused by footing by incorporation of an effective beam thickness and combdrive gap. In this case, effective parameters were optimized to match deflection data.*

In this case the calculated values match the measured values to with 2.54% on the average. The same value for $h_{effective}$ used in a FEA model results in a calculated value of 3.359 kHz for fundamental frequency, which is within 11% of the measured value of 3.775 kHz.

Using $h_{effective}=1.15\mu m$ and $gap_{effective}=2.85\mu m$ results in better agreement between calculated and measured values for fundamental frequency. The calculated value of 3.774 kHz from FEA is within 0.03% of the measured value of 3.775 kHz. However, using these parameters the agreement between measured and calculated actuated deflection is not as good but still within 17% on the average. This plot is shown in Figure 4-10.

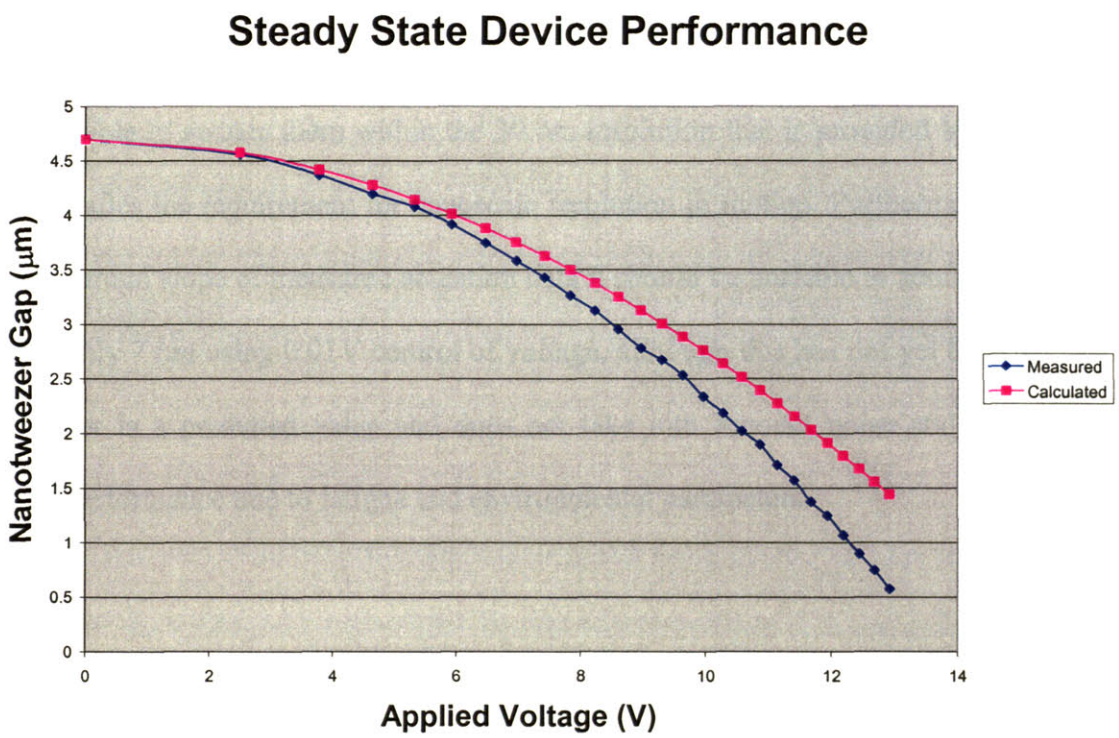

Figure 4-10. *Graph showing measured vs. calculated actuation data. The new calculated data accounts for structural deviations caused by footing by incorporation of an effective beam thickness and combdrive gap. In this case, effective parameters were optimized to match in-plane frequency response.*

The implementation of an effective thickness and gap is believed to best represent the real state of the nanotweezer, since the same correction addresses both deviations in actuation and frequency responses pretty well. It is consistent. Using this justification a value for effective thickness in the range of 1.06 μm to 1.20 μm and corresponding

effective gap reasonably reconciles measured and predicted values for both actuated deflection and fundamental frequency behaviors.

It is important to note that despite the harshness of the DRIE process its effect is uniform over the scale of the device and does not perturb its symmetry. In fact, the two arms of the nanotweezers close with impeccable alignment during the entire range of motion (see Figure 4-2 and Figure 4-3). This is an indication of the symmetry of the nanotweezers' structures and the device level uniformity of the processes used. The nanotweezers are more compliant than predicted due to the effects of DRIE. Despite this, it is possible to actuate them within the 30 nm resolution that is provided by the ESEM. This satisfies the requirement for nanoscale resolution in motion. Furthermore, based on the maximum slope of measured actuation data it should be possible to actuate the gap to within only 7 nm using 0.01V control of voltage, although this has not yet been verified. The latter is a predicted value and does not take into account noise and variation of device performance due to fatigue and environmental parameters.

Chapter 5 Nanocut Process

The Nanocut process is the culmination of various attempts to fabricate aligned nanoscale tips with nanoscale spacing using microscale lithography. The process makes use of oxidation as a method for fine tuning feature size.

5.1 Process Flow

The diagrams in Figure 5-1 show the wafer after key steps during the process. This process makes cut or holes that are self-aligned to the apex of protruding structures. The idea behind process is to use oxidation to as a means to define the size of the cuts and holes. This process as will be shown in section 5.3, can be combined with the Struct-v3 process to make nanotweezer with nanoscale tips with a nanoscale gap. Figure 5-2 shoes SEM photos of pyramidal walls created using this process. Figure 5-3 show a close up view of the top edge of these walls. The top edges are sharp to within ~50nm.

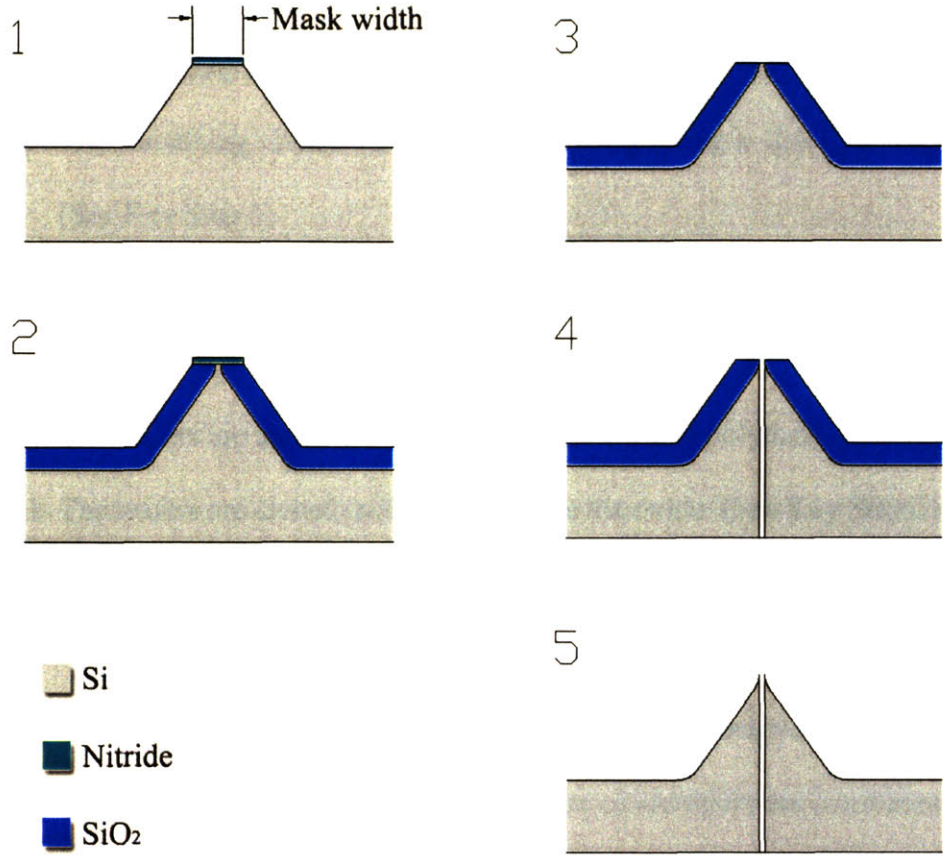

Figure 5-1. *Process flow diagram for the Nanocut process*

A Si wafer with the <100> crystal plane orientation on the top surface is need for the following process.

1. 2000A of LPCVD stoichiometric Si nitride is grown on the wafer at 775°C
2. The wafers are coated with photoresist
3. 1 μm wide lines are patterned using a stepper lithography tool
4. The nitride is etched using a dry CF_4 Nitride RIE etch.
5. The wafers are etched in 80°C KOH using the nitride lines as a mask pattern to etch down 1 μm. (See Key Step 1)
6. The wafers are cleaned using a Piranha etch.

7. The wafers are oxidized using the nitride as a mask against thermal oxidation. (See Key Step 2)
8. The remaining nitride lines are etched away using a dry CF_4 Nitride RIE etch. (See Key Step 3)
9. The wafer are etched using the DRIE etch detailed in section3.2. The oxide on the wafers is used as a mask. (See Key Step 4)
10. The wafers are ashed in oxygen plasma to remove polymers from DRIE.
11. The wafers are etched in BOE to remove the oxide. (See Key Step 5)

In step 7 the nitride acts as a barrier against the diffusion of oxygen to the Si and prevents any oxidation from the top. During thermal oxidation, SiO_2 grows at the SiO_2-Si interface. Roughly 46% of the oxide grows underneath the original exposed surface while the other 54% grows above it. During step 7, the oxide thickness consumes Si from both sides and pinches down underneath the nitride mask. Subsequently, in step 9, this oxide is used as mask for DRIE. The resulting gap between the tips is a function of both the initial width of the nitride mask and the oxidation thickness. Given a selectivity of 100:1 for Si vs. SiO_2, it is reasonable to assume that the DRIE etch will not significantly deteriorate the oxide mask for shallow etches.

Under this assumption:

$$gap_{tips} \approx w_{nitride} - (2 \cdot 0.45 \cdot x_{oxide}) \tag{5-1}$$

where gap_{tips} is the gap between the tips, $w_{nitride}$ is the initial width of the nitride mask, and x_{oxide} is the oxide thickness. This is an approximate function and depends in part to how

well the DRIE process is tuned to match the channel width to what is defined by the oxide. The oxidation time determines the oxide thickness according to the Deal-Grove model.

$$x_{oxide} = 0.5A_{DG}\left[\sqrt{1+\frac{4B_{DG}}{A_{DG}^{2}}\left(t+\tau_{DG}\right)}-1\right] \tag{5-2}$$

where A_{DG} and B_{DG} are temperature dependant constants and τ_{DG} is a function of the initial oxide thickness and is given by the following equation.

$$\tau_{DG} = \frac{x_{initial}^{2}}{B_{DG}} + \frac{x_{initial}A_{DG}}{B_{DG}} \qquad 5\text{-}3)$$

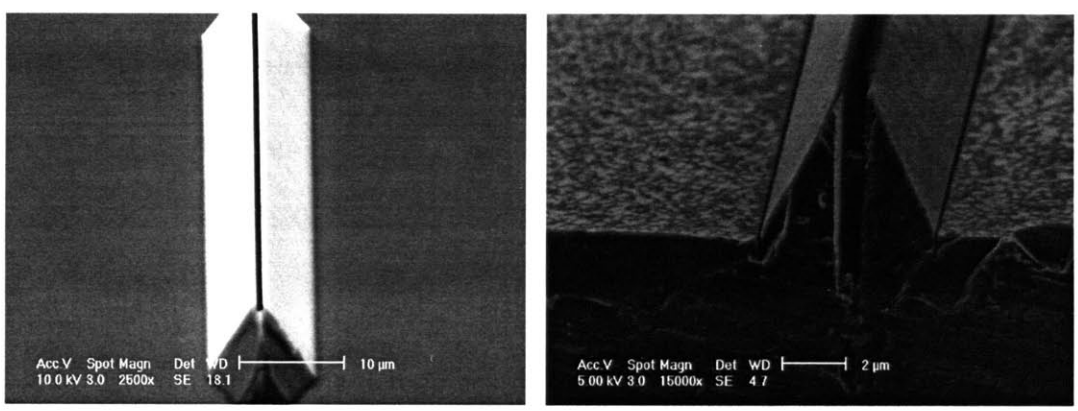

Figure 5-2. *SEM photos of features created using the Nanocut process. On the left is a view of a pyramidal wall created by a nitride line mask. On the right is a cross-section view of a similar pyramidal wall.*

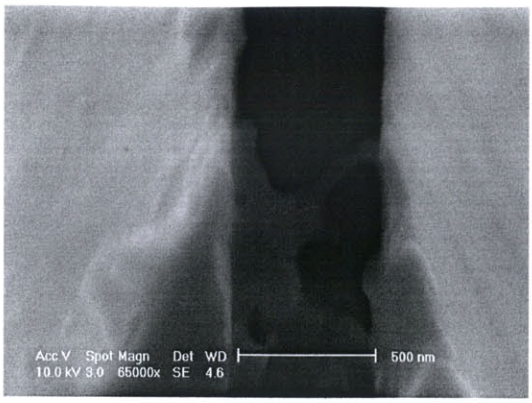

Figure 5-3. *Close-up cross-section SEM photos of a pyramidal wall created using the Nanocut process*

5.2 Process Results

In order to characterize the Nanocut process, 5 wafers with initial nitride mask lines were oxidized with consecutively thicker oxide and carried all the way through the Nanocut process. Each wafer contained nitride mask lines of widths ranging from 1 μm to 10 μm at integer values. Figure 5-4 shows an SEM of one such wafer showing the 10 different cuts resulting from the 10 different starting line widths. All nitride lines had a starting thickness of 0.019 μm.

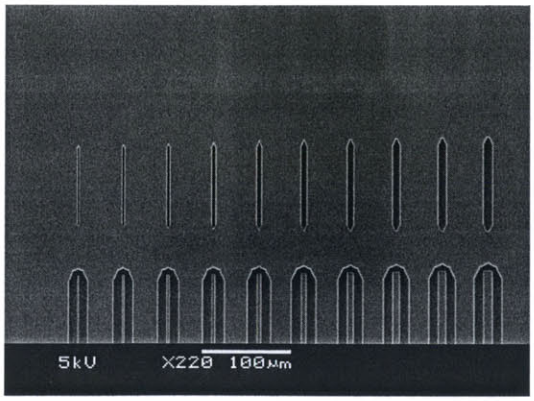

Figure 5-4. *SEM photo of experimental results for the Nanocut process*

The amount of oxide growth was predicted using the Deal-Grove model for the 1000 °C wet oxidation. For the oxidation tube used (MIT MTL Tube5D-thickox) the coefficients are $A_{DG}=0.299\mu m$ and $B_{DG}=0.258\mu m^2/hr$. Using these coefficients the plot in Figure 5-5 shows predicted results versus those measured after oxidation.

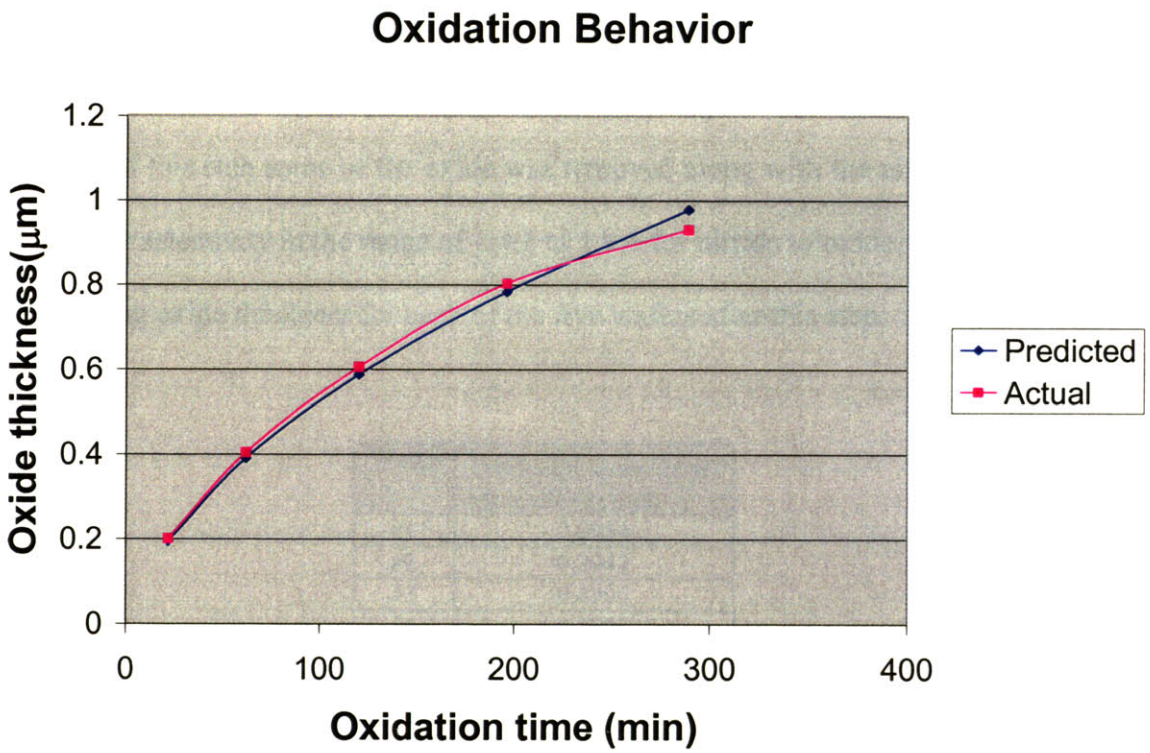

Figure 5-5. *Graph of oxidation thickness vs. time for the thermal oxidation process*

Table 5-1 shows the starting oxide thicknesses used for each wafer.

Wafer	Oxidation time (min)	Oxide thickness (μm)
#1	22	0.1995
#2	62	0.4023
#3	120	0.6028
#4	196	0.8010
#5	289	0.9727

Table 5-1. *Table of starting oxide thickness for each wafer*

After oxidation, a CF_4 nitride etch was used to remove the nitride. Due to poor selectivity of this etch some of the oxide was removed along with the nitride. The nitride CF_4 etch has selectivity in the range of 1.4:1 to 1.9:1 for nitride to oxide. Table 5-2 shows the remaining oxide thickness for each of the five wafers after this step.

Wafer	Oxide thickness (μm) after nitride etch
#1	0.0954
#2	0.2942
#3	0.4905
#4	0.6791
#5	0.8518

Table 5-2. *Table of oxide thickness for each wafer post nitride etch*

Finally, the "FARDAD" DRIE recipe, detailed in section 3.2, was used to etch the cuts using the grown oxide as a mask. The DRIE etch was carried out for 6 minutes for each wafer. Table 5-3 shows the remaining oxide thickness for each of the five wafers after DRIE.

While the DRIE has very good selectivity of ~100:1 Si to oxide, a small amount of oxide was still removed in this step. However, all wafers had some oxide left at the end of the process.

Wafer	Oxide thickness (μm) after DRIE etch
#1	0.0161
#2	0.2096
#3	0.4050
#4	0.5961
#5	0.7690

Table 5-3. *Table of oxide thickness for each wafer post DRIE etch*

Any remaining oxide was removed at the end of the process using BOE. It is important to design the process and mask widths so that some amount of oxide survives the entire process. If the oxide is depleted too early, the width of the cut will widen. Then, the width will no longer be defined by the oxide thickness. In addition, the sharpness of tips will be affected if the oxide is depleted. The following equation can be used to properly design a process that does not deplete the oxide layer.

$$x_{oxide} \geq \left(\frac{thickness_{nitride}}{1.5} + \frac{DRIE_{depth}}{100} \right) \cdot \left(1 + f_{litho}\right) \tag{5-4}$$

$$w_{nitride} \approx gap_{tips} + \left(2 \cdot 0.45 \cdot x_{oxide}\right)$$

In this equation, f_{litho} is roughly a function of the difference between the lithography resolution and the desired resolution for Nanocut. The larger this difference, the higher the uncertainty in $w_{nitride}$ and the need for more room to adjust x_{oxide}. The exact value of

f_{litho} also depends on the repeatability of the entire lithography process including development. A factor 0.2 is good starting place. The Nanocut process has been successfully executed with as little as 0.017 μm of nitride. Using 0.019 μm of nitride is safe thickness to design for.

Figure 5-6 shows the final cut width (gap_{tips}) as function of oxide thickness. The various lines represent the starting nitride mask widths ($w_{nitride}$) defined by lithography. For the smallest width of 1 μm, it was possible to pinch the cut width all the way to zero using oxidation. The nonlinearity in the plot is due to the DRIE etch process. This nonlinearity is hard to define quantitatively as it depends on many factors, including the interplay between the etch and deposition steps and charging of the oxide mask. While Nanocut is a batch process, it requires one control wafer to be sectioned and observed in an SEM after the KOH etch to determine the oxidation time necessary to obtain the desired cut width. However, given the wafer to wafer repeatability of lithography and thermal oxidation, many wafers can be batch fabricated based on the results of one control wafer in the lot. In addition, using profiler metrology tools it is possible to measure each wafer to obtain an average measure of oxidation necessary for the entire wafer lot.

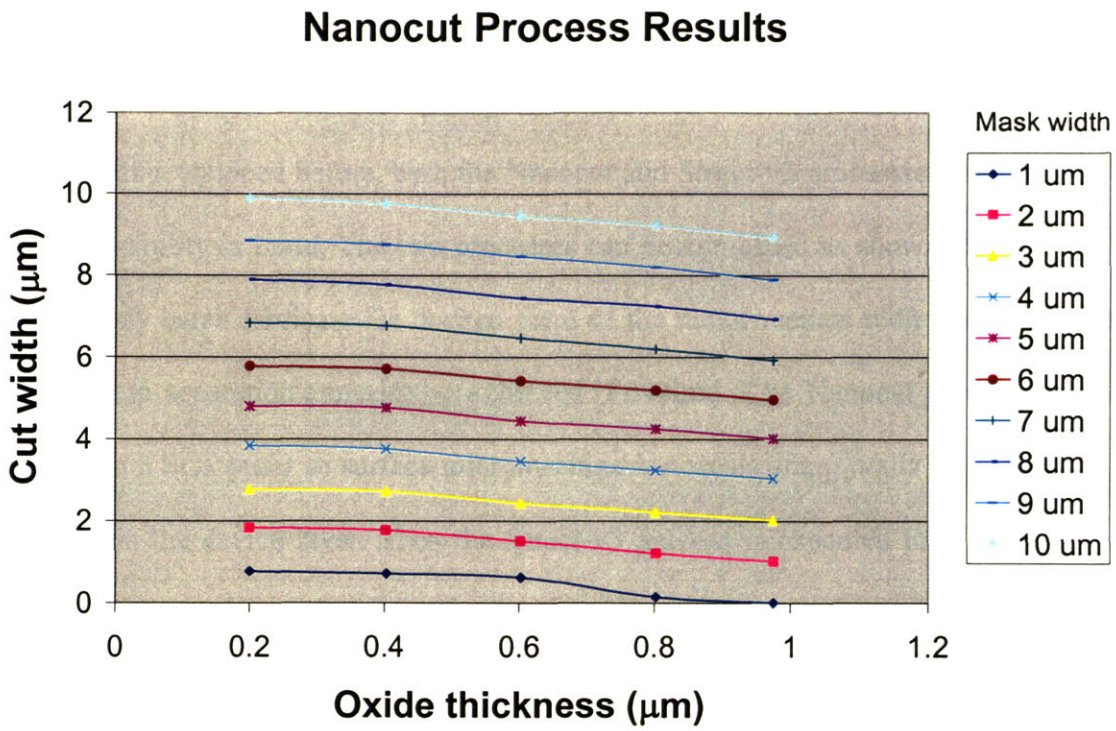

Figure 5-6. *Graph of results for the Nanocut process*

This process was developed in parallel with the structure process. At the time, it was not clear that the structure process could create adequately symmetric nanotweezers arms that close with good alignment. Hence, a parallel target goal of the process, as mentioned in section 1.4.2, was to create smaller gaps on the scale of the objects to be picked up to minimize the required range of motion of the arms and any lateral misalignment. In retrospect, while it is still very necessary to create nanoscale tips with nanoscale alignment, it is not critical that they be separated by nanoscale gap.

5.3 Combination of Nanocut and Struct-v3 processes

As was mentioned before, both the Nanocut and Struct-v3 processes were designed with compatibility in mind. The two processes can be combined as shown in Figure 5-7 to completely batch fabricate the desired form of the nanotweezers with nanoscale tips. Nanoscale tip separation can also be achieved if desired. The Nanocut process is first executed on a SOI wafer to surface micromachine nanoscale sharp walls with nanoscale separation in the device layer. Then the Struct-v3 process is executed to micromachine the flexure mechanism and combdrive structures that in combination with the Nanocut features result in the final form nanotweezer. For the combined process;

1. Photoresist is used to pattern nitride lines using a dry etch.
2. The nitride lines are used for the KOH etch.

   A control wafer is taken out of the process and measured to see how much oxide needs to be grown to achieve the desired gap between the tips.
3. Thermal oxide of appropriate thickness is grown.
4. The oxide is used as a mask to DRIE etch the gap all the way down to the buried oxide.
5. Using a wet BOE the masking oxide is removed leaving inherently sharp tips.
6. The wafer is coated with photoresist and patterned with the nanotweezers structure pattern.

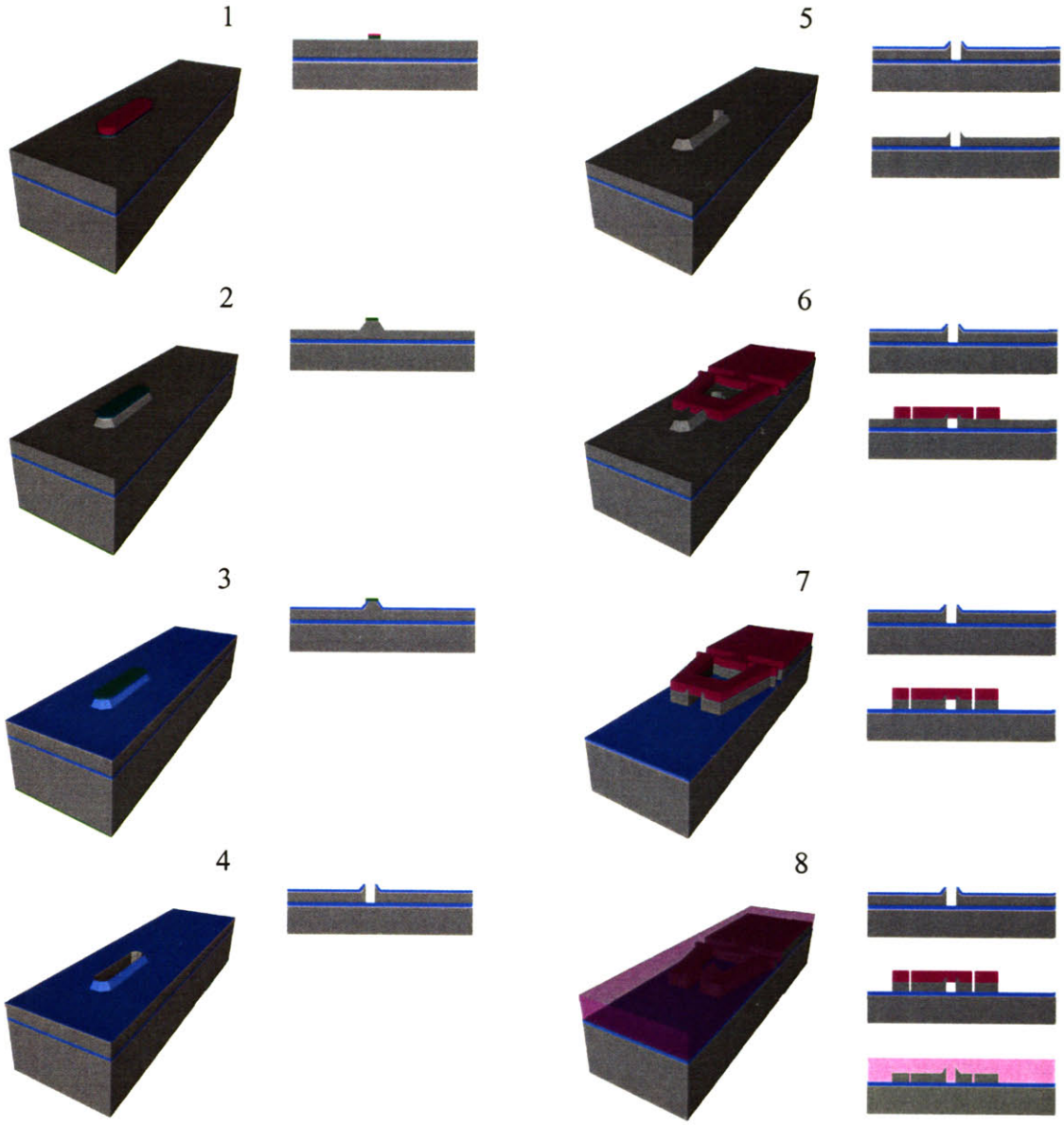

Figure 5-7. *Schematic of the combined Nanocut and Struct-v3 processes*

For simplicity and generic nanotweezers structure is used in Figure 5-7 to represent the arms and the combdrive. In addition, bumper structures, which would have to be used, are omitted in the figure. From here on the Struct-v3 process is executed with one minor yet key difference. As shown in Figure 5-7 step 7, this structure pattern does not include a gap to separate the two arms. Instead, it relies on a pre-existing gap from the Nanocut

process. In fact, if this structure pattern were to be used on an unprocessed SOI wafer it would produced inoperable nanotweezers with the two arms fused together.

In the final form, the contact pads, flexure structure, and combdrives are micromachined using the Struct-v3 process. Prior to that, the tips and tip separation are pre-defined in the wafer using the Nanocut process. From that point on, the structure is coated with the thick bracing photoresist and the rest of the Struct-v3 process is completed as before. The tips consist of the sharp corners of the pyramidal walls. The approach angle between the nanotweezer and the sample prevents the entire top edge of the walls from touching the sample. In addition, gray scale DRIE[20] etch can be used to create gradient height walls that result in protruding tips, which do not require and approach angle between the nanotweezer and the sample.

5.4 Other Applications of Nanocut

In general terms, Nanocut is a process to make cuts or holes that are self-aligned to the apex of protruding structures using oxidation for feature definition. These protruding structures can be defined using KOH etch, or they can be defined using other methods. For example, a purposely poorly executed reactive ion etch process that produces angled side walls was used instead of KOH etch to create the thin Si walls shown in Figure 5-8 shows.

The advantages of Nanocut are its ability to fine tune feature gaps to within tens of nanometers and its self-alignment. In Figure 5-9, Nanocut was used to fine tune the capacitance gap for resonating rings designed by Arvind Narayanaswamy for a metamaterials application. This structure was created as a potential stamp for making the

rings. The top two SEM pictures show the stamp structure as defined by lithography and the bottom two after Nanocut has been used to pinch down the gap. As mentioned before, Nanocut can also be used to create self-aligned holes. Figure 5-10 shows SEM photos of an array of holes created using Nanocut that can be used for application in near field optical data storage.

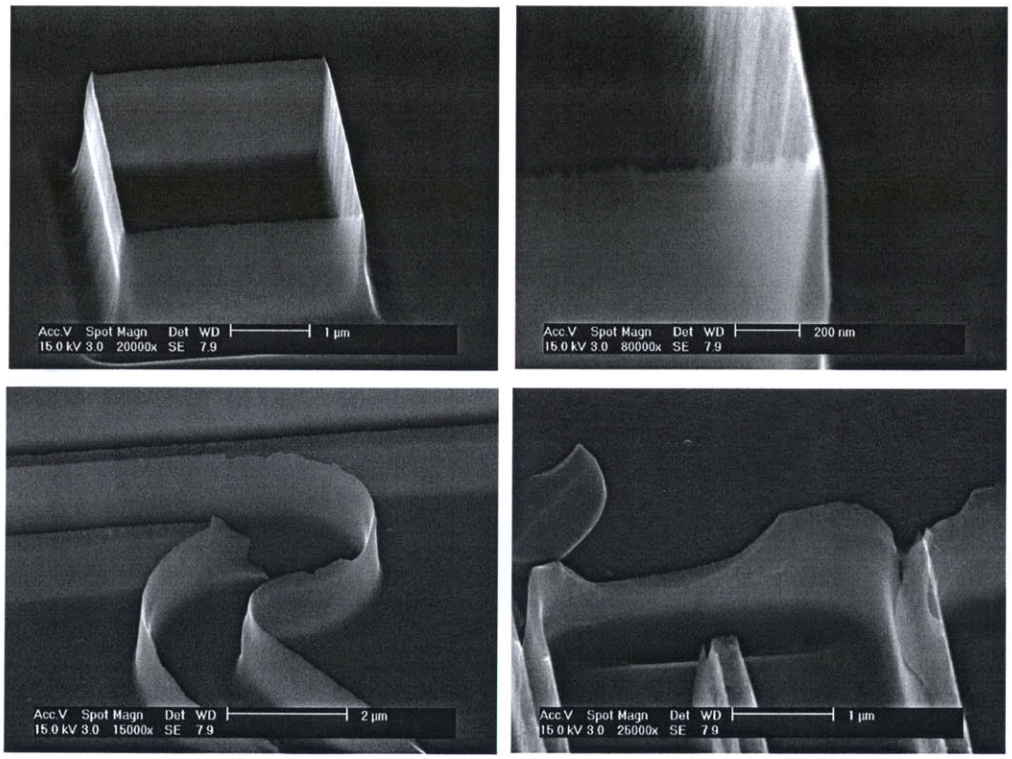

Figure 5-8. *SEM photos of thin walls micromachined into Si using the Nanocut process*

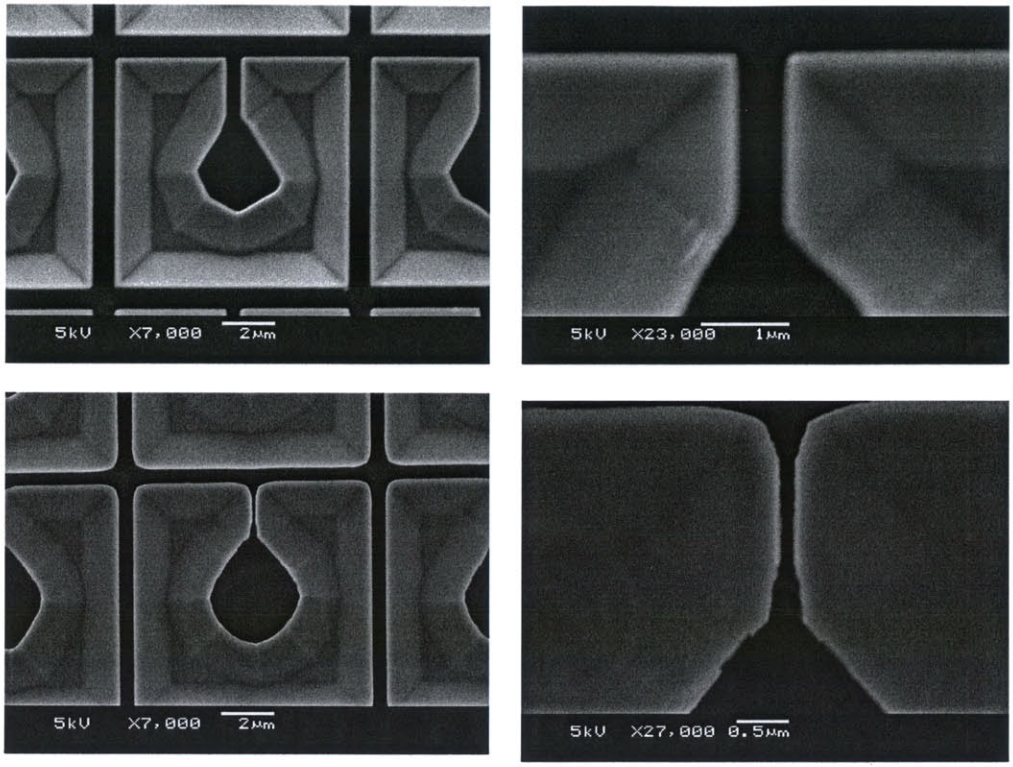

Figure 5-9. *SEM photos showing the application of the Nanocut process to rings fabricated for Metamaterials applications*

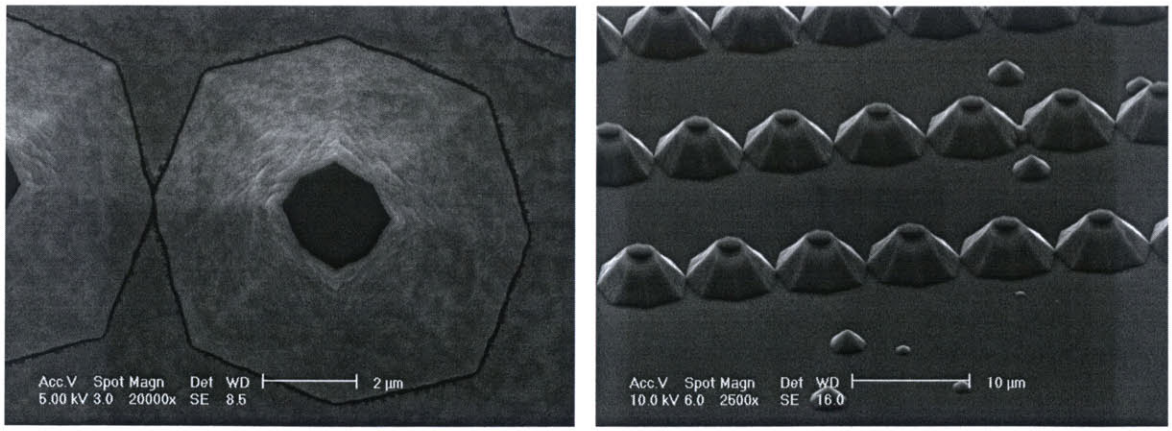

Figure 5-10. *SEM photos showing an array of apertures created using the Nanocut process.*

Chapter 6 Future Work and Conclusion

This project has been a preliminary attempt at generating nanoscale motion from microscale structures and using standard microfabrication techniques for creating nanoscale features. Based on this experience it is apparent what improvements should be made to both the fabrication process and the design to further satisfy the goal of a high utility batch fabricated nanotweezer. In the future, the Struct-v3 and Nanocut processes should be combined to fabricate completed nanotweezers that implement the following improvements

6.1 Future Work and Considerations

6.1.1 Robust design paradigm

In microfabrication, more so than other types of manufacturing methods, process parameters are difficult to control precisely. Variations in process can cause variations in device characteristics and consequent variation in device performance. For example, variations in the isotropy of an DRIE etch, exposure time during lithography, or spin rate during development can all result in dimensional variations of the beam thickness of the flexures. This changes the stiffness of the beams and affects how much the nanotweezers

close as a function of the actuation voltage. Therefore it is desirable to design the nanotweezers whose performance characteristics are impervious to dimensional variations of the beams or the actuators features. In particular it is desirable to have the displacement vs. voltage characteristic of the nanotweezers to be the same despite out of plane thickness or in plane dimensional variations. For both combdrives and parallel plate actuators, force behavior as a function of voltage has a linear dependence on out of plane thickness t. For combdrives

$$F = \frac{nk\varepsilon_o t V^2}{g}$$

For parallel plate

$$F = \frac{wtk\varepsilon_o V^2}{2x^2}$$

In addition, for designs that use only beams in pure bending, the deflection as a function of force always has an inverse dependency on the area moment of Inertia I and hence an inverse dependence on the thickness t. Note that the out of plane thickness of the device is the width of the beams.

$$v(F) = const \cdot \frac{F}{EI} = const \cdot \frac{F}{E\frac{th^3}{12}}$$

The combined equation, describing the deflection of the device as a function of voltage, has not dependence on the out of plane thickness t as the linear and inverse dependencies cancel. For example for the single half hammock flexure driven by a combdrive, the following equation characterizes the deflection behavior as function of voltage.

$$v(F) = -\frac{FL^3}{12EI}$$

$$v(V) = -\frac{nkt\varepsilon_o L^3 V^2}{24E\frac{th^3}{12}g} = -\frac{nk\varepsilon_o L^3 V^2}{2Eh^3 g}$$

Therefore, such devices are not at all sensitive to variations in the out of plane thickness of the device for either combdrive actuated or parallel plate actuated devices.

For devices of this type that are actuated by combdrives only, it is also possible to design them such that they are robust against small in plane dimensional variations as well. For such devices the deflection behavior as a function of voltage has the following general form.

$$v(V) = \frac{AV^2}{h^3 g}$$

The value of the constant A will vary depending on the specific design. For the half hammock flexure driven by a combdrive $A = -\frac{nk\varepsilon_o L^3}{2E}$.

Since the nanotweezers are very small, the distance between the combdrive teeth and the beam members is small compared to the size of the wafer. Therefore, despite lack of wafer uniformity, it is reasonable to assume that for any given nanotweezer both the beams and the combdrives are subject to the same process and consequent dimensional variations. Any process variation that thickens the beams also thickens the combdrive teeth and reduces the combdrive gap. Thus any change that makes the beams stiffer also makes the actuators stronger.

$$dh = 2\delta_{process} = -dg$$

where $\delta_{process}$ is the thickness variation of the beams due to processing and is defined positive in the direction for which the beams become thicker. Potential reasons for a positive $\delta_{process}$ are under etching or underexposure during lithography.

It desirable for R defined as the ratio of the deflection to the square of the voltage to be constant regardless of process and dimensional variations.

$$R = \frac{v(V)}{V^2} = \frac{A}{h^3 g}$$

$$dR = \frac{\partial R}{\partial h} dh + \frac{\partial R}{\partial g} dg = 0$$

$$dh = -dg$$

$$\frac{\partial R}{\partial h} dh - \frac{\partial R}{\partial g} dh = 0$$

$$\frac{\partial R}{\partial h} = \frac{\partial R}{\partial g}$$

$$\frac{-3A}{h^2 g} = \frac{-A}{h^3 g^2}$$

$$h = 3g$$

Hence if the nanotweezers are design such that the thickness of the beams are three times the combdrive gap, then the deflection vs. voltage behavior of the devices will not change for very small dimensional variations due to processing.

6.1.2 Sensing tip sample interactions

In order to increase the utility and versatility of the nanotweezer, it is highly desirable to be able to measure both the position and force of tips. These capabilities would allow even gentler gripping and manipulation of objects than current open loop schemes relying on the compliance of nanotweezers to mitigate errors in position. In addition to more refined manipulation, these capabilities will also allow the nanotweezers to be used to mechanically test micro and nanoscale objects.

6.1.2.1 Measuring force

The ability to measure the capacitance of the device in combination with drive voltage control can be used to control the force of the actuator As already mentioned in section 2.2.3, the force of a combdrive actuator is proportional to the square of the drive voltage per

$$F = -\frac{V^2}{2}\frac{dC}{dx} \qquad \textit{(general force expression)} \quad (2\text{-}4)$$

While the drive voltage is known, geometrical variations in fabrication may cause a change in *dC/dx* adding errors to the force measurement. In order to faithfully measure force from the drive voltage the value of *dC/dx* must also be measured. One way to do this is to superpose a small amplitude high frequency signal on top of the dc voltage used actuate the device. This high frequency signal will in turn generate a current on the capacitor electrodes of the combdrive. In general,

$$I = C(x)\frac{dV}{dt} + V\frac{dC}{dx}\frac{dx}{dt}$$

where *dx/dt* is the velocity of the combdrive. However, the design of the flexure actuator pair can be implemented in such a way to reduce the effect caused by the velocity of the combdrives. Effectively then,

$$I \approx C(x)\frac{dV}{dt}$$

The main problem arises from the small value of the capacitance to be measured. For the particular design detailed in this thesis the capacitance is about 7.1-10.6fF within its range operation, as designed. Another nanotweezer design incorporating smaller 1μm combdrive gaps, has a capacitance of about 44fF. Based on the performance of both these devices, there is enough alignment accuracy to use combdrives with more teeth and larger stroke to achieve capacitance changes as high as 100fF. However, even at 100fF, the

capacitance of the combdrives is still quite small. The parasitic capacitance of the contact leads to the ground can be in the range of 80fF-4000fF depending on whether the substrate is grounded and whether the electronics used to process the signal are on the same chip as the nanotweezers. Therefore this parasitic capacitance also has to be taken into account. Through the use of elaborate charge measuring circuits incorporating switching transistors it is possible to isolate and measure the capacitance of the combdrives. While a detailed discussion of these methods is beyond the scope of this project, as a proof of feasibility, Analogue Devices Corporation uses a similar method along with low pass filtering and demodulation to measure variations of a 100fF capacitor in their ADXL150 capacitive accelerometer.[21] In their device, the change in capacitance is used to measure the position of a proof mass as an indication of acceleration, the latter of which can be measured to within 0.1% of range at 1 kHz. A direct comparison of the ratio of the measurement resolution to range between the ADXL150 output and the nanotweezer combdrive is inaccurate. The ADXL150 uses a differential parallel plate capacitor instead of a combdrive and operates in a different environment with different noise characteristics. However, for force measurement of the nanotweezers a 0.1% of range measurement of capacitance is also not necessary. For the nanotweezers, this measurement is not used to measure the position of the combdrive electrodes. Instead, it is to be used to get a global indication of dC/dx. While the exact value of dC/dx depends on fabrication outcome, given adequate interdigitation of the teeth, dC/dx should remain constant through out the travel range. A relative measure of capacitance at two extremes of its range is feasible and sufficient to determine what this constant is. Using such a capacitance measurement in combination with the position

measurement of the combdrive, two data points to indicate the *dC/dx* can be obtained. The exact accuracy of such a measurement is dependant on too many factors determine without putting to practice but should be quite possible using similar methods as the ADXL150.

6.1.2.2 Measuring position

Measuring the position of the combdrives, which corresponds directly to the position of the tips, can be combined with the capacitance measurements to obtain *dC/dx* and thereof the force of the actuator as a function of voltage. By itself, monitoring the position can be used in conjunction with the image from the AFM to determine the right closing gap of the tips to pick up an object. In addition, sudden changes in the closure rate of the tips while increasing the drive voltage is indicative of an obstruction in the way to the tips.

Given the existence of a laser source and a photodiode in AFM instruments, it is particularly attractive and practical to make use of diffraction to measure position. The idea is to setup of a grating structure made of a flexure whose pitch depends on the position of the arms. Light from the laser is then reflected off of the individual members making up the grating. An advantage of this method is that, while fabrication variations in geometry may affect the thickness of the members making up the grating pattern, they do not affect its pitch. There are two methods of implementing a flexure based grating setup. The first is to add a secondary flexure making up the grating to connect to the nanotweezer arm as shown in Figure 6-1. This approach will add to the stiffness of the arms, however, a large number of grating lines can be used.

A second approach is to use the already existing flexure mechanism of the arms as the grating. This solution is simpler but limits the number of grating lines to three to five. A maximum of five lines can be achieved with other flexure designs incorporating more sub-flexures in series. Beyond five the ability of the flexure to guide motion and constrain compliance will be compromised or alternatively the flexure mechanism will have to become too big to do both. The current design detailed in this thesis is suitable for three grating lines while still maintaining reasonable size and performance.

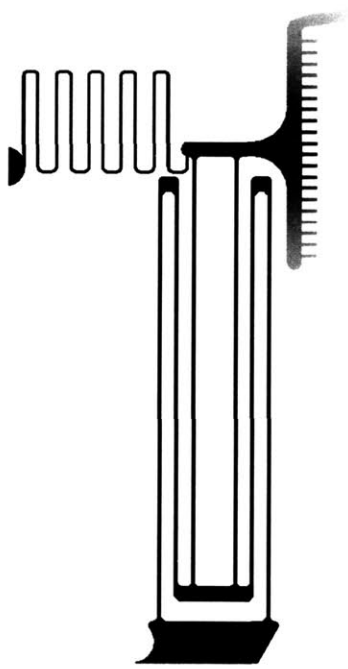

Figure 6-1. *Diagram showing the attachment of an external flexure based grating to the existing nanotweezer arm. The grating flexure would be designed to be much more compliant than the arm flexure.*

Given a grating of N lines at pitch distance d, equation (6-1) describes the intensity of the diffraction pattern as a function of the angle θ.[22] In this method, each line of the grating is treated as a coherent oscillator source in phase with the others. A small

angle of incidence from the source laser to the grating and small angle of reflection from the grating to photodiode is needed if N is small. In the latter case, the laser and photodiode of the AFM can not be used. I_o is the reflected intensity due to any one of the grating lines at the plane of the photodiode. k is the wave vector for the laser source. Figure 6-2 shows the plot of normalized I.

$$I = I_o \frac{\sin^2\left(\frac{Nkd\sin\theta}{2}\right)}{\sin^2\left(\frac{kd\sin\theta}{2}\right)} \tag{6-1}$$

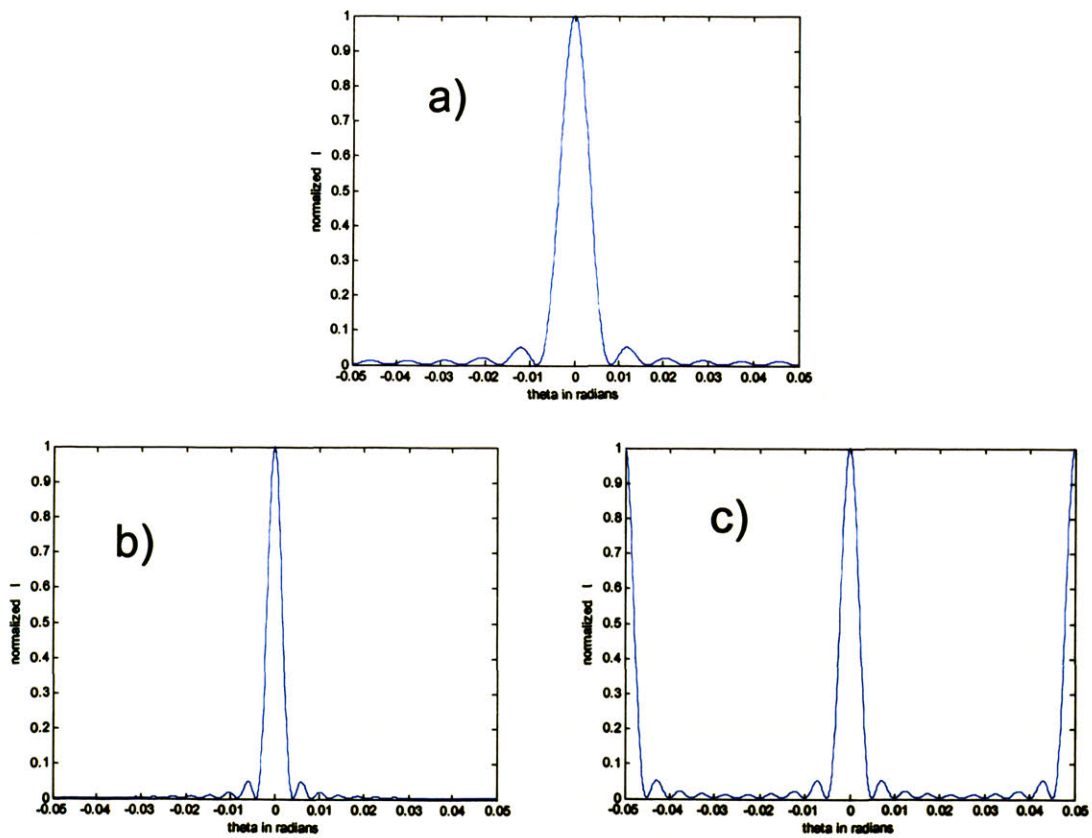

Figure 6-2. *Plots showing normalized intensity of reflection of a grating as a functional of angle a), with increased number of grating lines b), with increased spacing between the grating lines c).*

Increasing the number of grating lines N increases the sharpness of the principle maxima and brings the subsidiary maxima closer to each other. Increasing d brings the principle maxima closer together. Increasing the number of grating lines N is possible if a separate grating flexure is used but it allows for the use of the existing AFM laser and sensor. Given the use of the arm flexure as a grating, N is limited to 5 for practical reasons. d is limited to be 1 to 2 μm. Using $d=1\mu m$ a shift of about 0.04 radians, which is 2.3 degrees, can be obtained in the location of the second subsidiary peek. Figure 6-3 shows the diffraction pattern as a function of θ. A 500nm wavelength source is assumed. The blue pattern is with the device at the relaxed-state and the red pattern is with it extended to fully close the gaps.

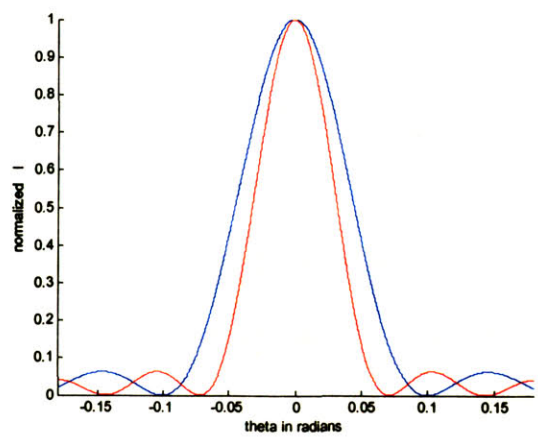

Figure 6-3. *Plots showing normalized intensity of reflection of a flexure arm grating as a functional of angle. Blue plot corresponds to the relaxed state. Red plot corresponds to the fully extended state.*

Even with this limiting case, by placing the sensor at a distance of 2.5 cm, the spatial shift of this peek is about 1 mm. It is quite feasible to use a CCD sensor to image the diffracted image and use it to detect changes in the spacing of the nanotweezer flexure arm. However, this method would be difficult to implement this using the existing laser and photodiode of the AFM. If using the existing laser and photo sensor is a

priority, then probably a separate diffraction grating optimized to perform at the oblique angles is required.

6.2 Lessons Learned

6.2.1 Nanoscale tips

At the beginning of the project, study of prior art indicated that it was necessary for the tips of the nanotweezers to be separated by a nanoscale gap. This seemed like a reasonable requirement as the tips may misalign during a relatively large stroke of motion inward. In particular, since DRIE was used to fabricate the structures, there was a concern the damage caused from the scalloping may be non-uniform and affect the two nanotweezer arms differently. If this were the case then the arms would not be symmetric and would move differently as they close and misalign. Reducing the gap would reduce the range of travel required to close and hence also reduce the degree of misalignment. In addition, if it were possible to reduce the gap to be less than the width of the objects to be picked up, then it would be possible to fabricate the nanotweezers in the closed state and actuate them open.

In retrospect, while the DRIE process is very harsh and damages the device structures, it is adequately uniform in its effect. Specifically, while the effect of DRIE is not uniform across the wafer, it is uniform within the scale of the devices, which is about 500μm. Therefore, the symmetry of the devices is not affected by DRIE. The tips close with alignment that is at least within 30nm for the devices tested. Although the ability to separate tips by a submicron gap is still valuable and has other applications, it is not necessary as long as they can be fabricated with good starting alignment.

6.2.2 Process flow development

The combined Nanocut and Struct-v3 process is a 16 step process, counting photoresist deposition, lithography, and development as one step and not including the intermediate clean steps required for contamination purposes. In addition, the process uses SOI wafers, which are very expensive. Debugging the entire process as a whole can be quite difficult and expensive given the cost of each run. As a result, a better approach is to break the process into smaller sub-processes that are debugged individually using cheaper test or prime wafers. Each time two consecutive sub-processes are debugged they are combined into second level sub-process. Similarly consecutive debugged second level sub-processes are combined into third level and so on until the final working process flow is realized. It is very important to check and make sure overall process compatibility is maintained each time a change is made to debug a sub-process. This approach was successfully used to develop the Nanocut and Struct-v3 processes, which themselves are sub-processes to be combined to become the full process for fabricating nanotweezers.

The advantage of this approach is that it reduces the time and financial cost-risk of each debugging run. It is more efficient as problems are isolated to smaller set of potential contributing factors. It prevents stalling of the progress if any sub-process encounters at temporary impassible obstacle as there are always a number of parallel processes being debugged. This approach also works better for a busy clean room such as MTL, since overall progress is never hinging the use of one particular machine.

There are also disadvantages to this approach. Progress and generation of tangible deliverable results is highly non-linear. Initially, during the first level debugging and combination, there are almost no tangible deliverable results of substantial significance.

Towards the end, during the last level of debugging and combination everything falls into place and working devices are happily extracted for testing by a very relieved graduate student.

This approach is good for low budget ambitious projects. In addition, it also generates sub-processes at various levels that have other applications. It is good for establishing fabrication knowledge base and capability within the group that is not specific to just one project. It is not good for projects that need to deliver results on a periodic schedule to a funding agency or for projects that are competing for time to publication. It requires an understanding of all parties involved that progress is very non-linear and potential exit strategies in the unlikely even that the final debug and combination turns out to be impossible.

6.2.3 Sub-process debugging

It is difficult to debug some sub-processes when there are a large number of parameters that influence the final result. Often contradicting literature can be found that claim opposite affects for the same change in a parameter. In the clean room, the same modification can have opposing effects from one recipe to another and one machine to another. This is particularly true for dry plasma etch processes that are the result of a close race between etching and deposition from species in the plasma.

As an example, when trying to use the HBr based RIE etch on the AME5000 tool instead of DRIE for the Nanocut process, it was found that the side walls close in at the bottom of the channels. In order to alleviate this problem the pressure of the etch was increased to increase the sideways etch rate and open up the walls. Alternatively, the

pressure was left the same and the power to the plasma was increased to do the same and also increase the acceleration of the ions towards the wafer. Contrary to what was expected both changes made the walls close in even further. The reason is that both increased pressure and increased power, increased the rate of deposition more than they increased the etch rate and directionality. Observations of another group on a different tool of the same type do not necessarily apply. Process recipes are very machine and even chamber specific. The best way to analyze and modify a process is to keep good written record of observed effects specific to a machine and to share them with other users. To this end, Table 6-1 summarizes the modifications that were tried in this attempt. In general, opposite results from what is indicated in literature is quite possible, whereas data that is specific to a recipe on a machine is more reliable.

	Original	Trial#1	Trial#2
Etch step	4 steps	4 steps	4 steps
Pressure(mTorr)	200	250	200
Power(W)	350	350	450
Gauss	50	50	50
Time(sec)	4 of 250	2 of 250 + 2 of 0	2 of 250 + 2 of zero
Voltage limits(V)	0 to -1000	0 to -1000	0 to -1000
Cl2 flow rate(scc)	20	20	20
HBr flow rate(scc)	20	20	20
Cool step	3 in between etch steps	3 in between etch steps	3 in between etch steps
Pressure(mTorr)	200	250	200
Power(W)	0	0	0
Gauss	50	50	50
Time(sec)	180	180	60
Voltage limits(V)	0 to -1000	0 to -1000	0 to -1000
Cl2 flow rate(scc)	20	20	20
HBr flow rate(scc)	20	20	20
Stabilization Step	1 initial	1 initial	1 initial
Pressure(mTorr)	200	250	200
Power(W)	0	0	0
Gauss	50	50	50
Time(sec)	20	20	20
Voltage limits(V)	0 to -1000	0 to -1000	0 to -1000
Cl2 flow rate(scc)	20	20	20
HBr flow rate(scc)	20	20	20
Results	Walls close in at bottom of channel	Walls close in even more at bottom of channel	Walls close in even more at bottom of channel
	e-mail fardad@mit.edu for SEM photos and data	e-mail fardad@mit.edu for SEM photos and data	e-mail fardad@mit.edu for SEM photos and data

Table 6-1. *Table of poly-Si RIE etch modifications*

6.2.4 Summary of Contributions

The devices fabricated during this project already have many of the desired performance characteristics necessary to function as nanotweezer. The specific design included in this thesis already achieves nanoscale motion, constrained compliance, and good alignment of the arms. There is still a lot of room to optimize the design for better use as an AFM probe and to customize them for specific applications. There is a lot of work still to be done and the results indicate the approach covered in this thesis can be used to do so. The result of the project is a general frame work that enables the design and batch fabrication of nanotweezers with definable characteristics such as tip separation, desired in plane compliance, force range, guided motion path at nanoscale, and motion range and resolution.

6.2.4.1 Major contributions

This frame work is the result of two combinable processes. The first is a process for creating slender, high aspect ratio, overhanging, and planar structures. It uses a novel combination of photoresist and bumper structures in the device layer to brace the structures and circumvent problems due to surface tension. The process protects the devices all the way through the competition of an inclusive die separation that leaves them ready for use. The second process is a novel process for making very small cuts and holes in Si aligned to the apex of protruding features such as walls and pyramids. This process is a self-aligning process that uses oxidation to define the width of the cuts and holes to a much higher resolution and alignment than what can be achieved with lithography. This latter can be combined with the first to create nanotweezers with

nanoscale size and spaced tips. It also has the potential for other applications beyond the scope of nanotweezers.

6.2.4.2 Minor contributions

Two sub-processes developed for the lithography and DRIE etch of the nanotweezers may also have other useful applications. The lithography method is useful for saving mask space when patterning designs consisting of larger repeating patterns connected to small unique ones. This method, developed for use with stepper tools, allows for one instance of the large pattern to be repeatedly exposed and combined with each of the unique smaller patterns. The DRIE process is specifically adjusted for etching small features on the scale of a 2 μm. The size of the scalloping is observed to be a function of the width of the channels but has never been observed to be larger than 300nm. It is often observed to be less than 100nm. It is a good alternative to RIE for applications that require higher aspect ratios for very small features.

REFERENCES

[1] R. Young, J. Ward, F. Scire; *The Topografiner: An Instrument for Measuring Surface Microtopography*, Rev. Sci. Inst., Vol 43, No 7, p 999

[2] G. Binnig and H. Rohrer; *Scanning Tunneling Microscopy—From Birth to Adolescence*, Rev. of Mod. Phys, Vol 59, No. 3, p 615, Part 1 1987

[3] G. Binnig, C.F. Quate, Ch. Geber; *Atomic Force Microscope*, Phys. Rev. Letters, Vol. 56, No 9, p 930, 1986

[4] S. R. Manalis, S. C. Minne, A. Atalar,a) and C. F. Quate; *Interdigital cantilevers for atomic force microscopy*, Appl. Phys. Lett. 69 (25), p.3944-3946, 1996

[5] S.C.Minne, S.R.Manalis, and C.F.Quate; *Parallel atomic force microscopy using cantilevers with integrated piezoresistive sensors and integrated piezoelectric actuators*, Appl. Phys. Lett., Vol.67, No.26, p. 3918-3920, 1995

[6] Metin Sitti and Hideki Hashimoto; *Controlled Pushing of Nanoparticles: Modeling and Experiments*, IEEE/ASME Transactions on Mechatronics, VOL. 5, NO. 2, p. 199-211, 2000

[7] Guthold, M.; Falvo, M.R.; Matthews, W.G.; Paulson, S.; Washburn, S.; Erie, D.; Superfine, R.; Brooks, F.P., Jr.; Taylor, R.M., II; *Controlled manipulation of molecular samples with the nanoManipulator*, IEEE/ASME International Conference on Advanced Intelligent Mechatronics, AIM, p. 3-8 , 1999

[8] M.R. Falvo, et al; *Manipulation of individual viruses: friction and mechanical properties*, Biophys J., vol 72, pp. 1396-1403, 1997

[9] M. Guthold, et al; *Quantitative Manipulation of DNA and Viruses with the nanoManipulator Scanning Force Microscope*, Surf. Interf. Analys., vol. 27, 1999

[10] M.R. Falvo, et al; *Bending and buckling of carbon nanotubes under large strain*, Nature, vol. 389, p. 582-584, 1997

[11] M.R. Falvo, et al; *Nanometre-scale rolling and sliding of carbon nanotubes*, Nature, vol. 397, p. 236-239, 1999

[12] C.J. Kim and A. Pisano, *Silicon-Processed Overhanging Microgripper*, Journal of Microelectromechanical Systems Vol.1 No.1, p.31-36, 1992

[13] Kim P and Lieber C M; *Nanotube Nanotweezers*, Science 386 p.2148-2150, 1999

[14] Akita, S., et al; *Nanotweezers consisting of carbon nanotubes operating in atomic force microscope*, Appl. Phys. Lett. 79, p. 1691–1693, 2001

[15] P Bøggild, T M Hansen, C Tanasa and F Grey; *Fabrication and actuation of customized nanotweezers with a 25 nm gap*, Nanotechnology 12, p.331-335, 2001

[16] C Tsou, W T Lin, C C Fan, and Bruce C S Chou; A novel self-aligned vertical electrostatic combdrives actuator for scanning micromirrors, Journal of Micromechanics and Microengineering 15, p.855-860, 2005

[17] F. Lärmer and P. Schilp; *"Method of anisotropically etching Si"*, German Patent DE 4241045, 1994

[18] O Raccurt, F Tardif, F Arnaud d'Avitaya and T Vareine; *Influence of liquid surface tension on stiction of SOI MEMS*, J. Micromech. Microeng. 14, p.1083–1090, 2004

[19] C. Quentin Davis and D. M. Freeman; *Using a Light Microscope to Measure Motions with Nanometer Accuracy*, Optical Engineering 37, p.1299-1304, 1998

[20]Christopher M Waits, Alireza Modafe and Reza Ghodssi; *Investigation of gray-scale technology for large area 3D silicon MEMS structures*, Journal of Micromechanics and Microengineering vol.13, p.170-177, 2003

[21] Stephen D. Senturia; *Microsystem Design*, Kluwer Academic Publishers, 2000

[22] Eugene Hecht; *OPTICS fourth edition*, Addison Wesley, p. 449-452, 2002